

Chapter 11

Noninvasive Fluxomics in Mammals by Nuclear Magnetic Resonance Spectroscopy

Justyna Wolak, Kayvan Rahimi-Keshari, Rex E. Jeffries, Maliackal Poulo Joy, Abigail Todd, Peter Pediatitakis, Brian J. Dewar, Jason H. Winnike, Oleg Favorov, Timothy C. Elston, Lee M. Graves, John Kurhanewicz, Daniel Vigneron, Ekhson Holmuhamedov, and Jeffrey M. Macdonald

Abstract

Metabolism is an interconnecting network of metabolite consumption and creation. Metabolomics has focused on metabolite concentrations in metabolic networks. Fluxomics is also required in the study of metabolism and quantifies the flux of substrate through each reaction step or a series of reaction steps (i.e., metabolic pathway or cycle), and ultimately is required for energy balance equations of the system. The primary noninvasive method of quantifying fluxes in living systems is by in vivo ^{13}C nuclear magnetic resonance (NMR) spectroscopy. The present state of noninvasive in vivo NMR technology allows for just four simultaneous flux measurements of metabolic pathways: gluconeogenesis, glycogen synthesis, glycolysis, and citric acid cycle. Since the liver is the gatekeeper and metabolic center for the animal, in vivo fluxomics of liver is extensively reviewed. Additionally, other organ systems studies are discussed demonstrating interorgan cycles, such as the Cori and Randall cycles. This review discusses the basics of in vivo fluxomics focusing on the general details of the NMR experimental protocol and required hardware/software needed to analyze the data.

Currently, there are two general methods for determining multiple flux rates. The *dynamic* method entails acquiring serial time points, whereas the *static* method is a single measurement in which flux through metabolic pathways is quantified by isotopomer (i.e., isotope isomers) analysis. The flux data are analyzed by mathematical models to calculate the global flux measurement (in silico fluxomics), and create a mass balance of the biosystem. Models are especially useful for inferring various metabolic states of the system, which are affected by drugs, toxicants, or pathology. As with all in silico models, increasing the number of empirically derived concentrations and fluxes into the model greatly increases the accuracy and utility of the model. NMR spectroscopy (NMRS) is inherently insensitive compared to other analytical modalities, limiting the temporal resolution of the dynamic in vivo measurements. To address the NMR sensitivity, several technological advances have been made. First, magnets are now at higher magnetic field strengths. Second, the technique of dynamic nuclear polarization (DNP) of substrates increases the signal for ^{13}C up to five orders of magnitude.

In vivo fluxomics requires a broad knowledge of biochemistry, in vivo NMRS, and metabolic modeling. Therefore, this chapter is intended as a handbook for upper division undergraduate students and graduate students in biochemistry or engineering and relates the basics of electrical and biochemical engineering and animal handling. The chapter is intended for use in an introductory graduate course on NMR-based fluxomics for physical scientist.

Key words: Fluxomics, hyperpolarization, in vivo NMR, modeling

1. Introduction

Decoding of the human genome has brought about the need to phenotype a multitude of genotypes. Current methods for gene sequencing (genomics), quantification of mRNA (transcriptomics), and analysis of proteins (proteomics) require the destruction of the biological sample. On the other hand, metabolite analysis (metabolomics) can be done nondestructively using nuclear magnetic resonance (NMR)-based methods. Metabolomics focuses on the identification and quantification of small molecules (<2 kDa), typically at a single time point. However, missing from “-omics”-based analysis is the flux of substrate through a given pathway (fluxomics). Figure 1 shows how flux links all the “-omics.” For example, the environment can quickly change a biological system when stress is applied (Fig. 1). For example, newly exercised muscle tissue in the order of 1 min speeds up the rate of glycolysis 100-fold to maintain ATP for the actin-myosin complex (1, 2). The net effect of this action is that the ATP concentration does not drop by more than 40% (3). Genomic differences can also lead to altered phenotypes because mutations may exist that affect the flow of nutrients into and out of the cell. A cell switching from G_0 to G_1 and entering the cell cycle will exhibit a profound change in metabolism in order to make proteins, lipids, and nucleotides required for mitosis (4).

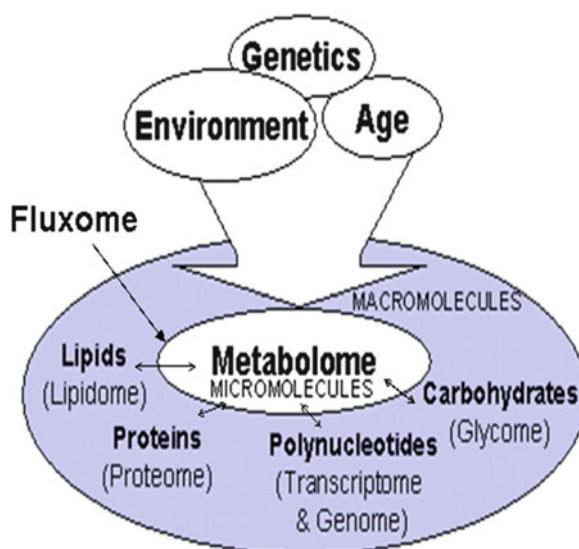


Fig. 1. Metabolomics connects to all the other “-omics” via metabolic turnover with macromolecules.

This is accomplished primarily from the consumption of carbohydrates. During an infection, lymphocytes significantly increase their pyrimidine pool, an order of magnitude, while purines are increased just fourfold (5). During DNA replication, it is essential that the four deoxynucleotides are of roughly equal concentration and not rate-limiting, otherwise a nucleotide substitution can occur causing a mutation. Therefore, cell cycle regulation of nucleotide metabolism is extremely robust (6). Metabolic regulation controls pyrimidine flux and will be discussed in Sect. 2.2.

Fluxomics is the quantification of biochemical reaction rates, or fluxes, in a biological system, while the fluxome is the summation of all fluxes within a biosystem. With current technology, it is not possible to measure all metabolites *in vivo*, so mathematical models are required to predict the entire fluxome. The commonly used mathematical methods for fluxomics include metabolic flux analysis (MFA) and metabolic control analysis (MCA) discussed in Chaps. 8 and 9, respectively. As an example of MFA, experimentally derived fluxes are used as input for the *in silico* MFA model, which then generates the fluxome (7, 8). Since technologically it is not yet possible to quantify the fluxome, the flux of measurable metabolites at key pathway junctions or branch points act as surrogate measures of flux through an entire metabolic pathway (9) and the rest is derived *in silico* (see Chaps. 8 and 9) (10).

The goal of fluxomics is to determine the mass balance within a given biosystem (11, 12). Mass balance is based on the first law of thermodynamics, conservation of mass and energy. Since virtually all reactions for energy generation are known and most experiments are performed in a closed system, a quantitative description of metabolite production and consumption rates can be balanced between the tissue and the environment. When the energy currencies of high-energy phosphagens such as nucleotide triphosphate (NTP) (13) and phosphocreatine (PCr) and redox factors, nicotinamide adenine dinucleotide (NADH), are incorporated, an energy balance is generated that can act as a metabolomic phenotype. For example, at the simplest level of complexity, cells in culture, the metabolites inside the cell (termed the “fingerprint”) can be balanced with the media (termed the “footprint”) by mass balancing the multitude of coupled reactions thereby generating an energy balance for the system. Dynamic energy and mass budget (DEB) theory and methods were developed in the early 1990s to determine mass balances at multiple levels of complexity: organisms (i.e., a network of organs and tissues), eco-systems (i.e., a network of organisms) (14), and even to assess global warming of the planet (15, 16). *In vivo* fluxomics can determine the mass balance in a biosystem making it a powerful phenotyping tool. For example, if a malignant tumor is cultured in a dish, the fingerprint will show increased consumption of glucose and glutamine while the footprint will show increased lactate production

(glycolytic end product) even under aerobic conditions. This metabolomic phenotype is called the “Warburg effect” (17) and could be given as a mass balance, or less detailed, an energy balance of phosphagens and redox cofactors, in the various compartments (i.e., intra- or intercellular) of the biosystem.

Production and consumption rates of metabolites can be determined by measuring the change in concentrations, or mass, over time using various techniques, including gravimetric, spectroscopic, or chromatographic in the biosystem where the boundary conditions are defined. For example, if the boundary conditions are the borders of a perfused liver, one can calculate the changes in concentration of nutrients or waste products in the perfusate entering and leaving the isolated liver (18, 19). However, in order to determine the contribution from the various metabolic pathways contributing to the nitrogen or carbon “mass balance” in a biosystem, one must use isotope tracers (^{15}N , ^{13}C , ^{14}C , ^{11}C) (20, 21), especially at steady state when concentrations do not change. For example, in the perfused liver example given above, if one were to quantify production and consumption rates inside the perfused liver at steady state, one would use isotopes to obtain rate constants. In vivo NMR spectroscopy (NMRS) has been used to measure flux rates noninvasively in intact animals as well as by high-resolution NMRS of tissue or cell extracts. This review covers all of the types of biochemical fluxes that have been quantified by NMRS with a *focus on perfused and intact liver and translation to humans*. Although some very elegant in vivo ^{15}N NMR studies were performed to quantify the hepatic urea cycle (22) and transamination (23) reactions using ^{15}N -labeled ammonia, as well as ^2H to define hepatic one-carbon metabolism (24), this review will focus on ^{13}C NMR studies.

Flux measurements by ^{13}C NMRS are done by *dynamic* or *static* methods. Examples of these methods at steady state and nonsteady state conditions will be discussed. The concept of time scales is very important in the accurate determination of flux. For a given compound within a biosystem, the time scale of reactions can change due to different compartmentation or *pools* (see Glossary for defining the subtle difference of these two terms). For example, pathways such as glycolysis, the citric acid cycle, and serine formation require temporal resolution on the order of minutes even seconds during a *dynamic* flux measurement in order to obtain accurate flux calculations. In contrast, the primary antioxidant of the body, glutathione, has a turnover of about 10 h and requires a temporal resolution on the order of hours. Total body protein turnover occurs in 3 days (25–27), yet insulin is synthesized in 20 min (28, 29), and some plasma proteins in several hours (30, 31). There are several pools of lipids in a cell with different turnover rates. For example, in brain the turnover of the glycerophospholipids, phosphatidylinositol, phosphatidylcholine and phosphatidylethanolamine depends on the attached fatty acids,

and for the fatty acid docosohexanoic acid, the half-life 3.9, 22.4, and 57.8 h, respectively (32, 33). This relatively short turnover of phosphatidylinositol reflects its utility in cell signaling. Also, there are different pools within the cell: those undergoing endocytosis forming lysosomes, those being synthesis in the endoplasmic reticulum, and those forming the nuclear and plasma membranes, as well as different pools in the different cell types within the brain (32, 33). These turnover rates depend on the environment (28), genetic disposition and cell cycle (34), and maturational age (21, 35, 36) of a cell. RNA turnover rates have been determined (37) and decrease with age that affects downstream protein translation (36), ultimately affecting mitochondrial function (38). The turnover of RNA (t-RNA, r-RNA, and m-RNA) is also tightly controlled by cell cycle machinery (39). The concept of the various time scales for turnover rates will be demonstrated using a specific example of glycine metabolism in Sect. 3.

Finally, a new technology, dynamic nuclear polarization (DNP), will be reviewed, which increases ^{13}C NMR sensitivity nearly 5 orders of magnitude, making 1 mM metabolites as sensitive as 55.5 M water (111 M protons). DNP ^{13}C spectroscopic imaging is being rapidly translated to the clinic (40). This new technology will be explained in Sect. 6.

2. Background: Fluxomics

2.1. Fluxomics and the Methods Used for Quantification of Flux

The essence of metabolism is captured by the quantification of organic and inorganic substrates defining a mass balance, which is based on the first law of thermodynamics, conservation of energy (see Chap. 3). A comprehensive measurement of mass balance of the biosystem would require measurement of all the concentrations and fluxes depicted in the generalized biochemical scheme shown in Fig. 1 and has never been done for any multicellular species. The primary available chemical potential energy of a biosystem is in the form of ATP and the capacitance stored across mitochondrial membrane (2). Biochemistry texts can be misleading by stating that the driving force of ATP hydrolysis is the high-energy phosphoanhydride bond. The critical thing is that ATP readily couples to other reactions via enzymes, both increasing the speed as well as being able to drive them against their own ΔG . ATP levels can be noninvasively quantified by in vivo ^{31}P NMRS (41). Fluorescence spectroscopy is the most common method used to measure mitochondrial membrane hyperpolarization using fluorescent dyes (42) or the endogenous redox couple NADH/NAD $^{+}$ (43). It is a relatively unknown fact that NMRS can measure endogenous redox couples, which correlate to the redox potential in the same manner as fluorescent tracers quantify the NADH/NAD $^{+}$ ratio.

In vivo NMRS is the only method permitting in situ measurements of multiple metabolites simultaneously. Therefore, in vivo NMRS is a powerful noninvasive method for fluxomics. In addition, these methods are easily translated to humans because they employ stable isotopes rather than (unstable) radioactive nuclides, which release ionizing radiation from nuclear decay. Even though doses are within safe ranges of exposure, radioactivity has become stigmatized within the patient population. In fact, the stigma associated with radioactivity prompted dropping the word “nuclear” from NMRS and clinically NMRS is known as magnetic resonance spectroscopy (MRS). By quantifying concentrations by ^1H spectroscopic imaging (44) and reaction rates by ^{13}C NMRS (45), production or consumption rates, or net flux rates, can be quantified, permitting determination of the mass balance of a biosystem.

In nuclear imaging, positron-emitters such as the radioactive nuclides, ^{11}C and ^{18}F , are incorporated into nutrients and are extremely useful in the detection and diagnosis of cancer. In particular, the success of positron emission tomography (PET) is due to its ability to detect increased uptake of glucose commonly observed in cancerous tissue. Since children have faster growing tissue than adults, and thereby more susceptible to permanent DNA mutations, it is advised they not be exposed to the positron-emitters used in PET due to radiation exposure. Rather, it is recommended that MRI or ultrasound be used instead (46). The positron-emitting ^{18}F -fluoro-2-deoxy-D-glucose (FDG) is more rapidly taken up in cancer cells, but is not metabolized beyond the hexokinase step due to the absence of the 2-OH group. Furthermore, there is usually a down-regulation of the phosphatase, resulting in a net accumulation of FDG compared with normal tissue. Thus, at most it provides an estimate of glucose transport and not intracellular metabolism. The emitted positrons annihilate electrons in nearby atoms, releasing two gamma rays, in opposite directions. The simultaneously detected gamma ray paths are reconstructed into a three-dimensional image.

PET-CT combination scanners enable a high-resolution X-ray image to register the metabolic PET image to colocalize the signal by dual image modalities for a validated cancer diagnosis (47). In clinical PET systems, the pixel resolution is between 4 and 6.5 mm, while whole body CT can reach a pixel resolution of 0.5 mm with 64 slices. ^1H MRI and hyperpolarized ^{13}C MRSI achieve a resolution of less than 0.2 mm with asymmetric voxels in 3 T whole body imagers (48). The advantage of both ^1H and hyperpolarized ^{13}C MRSI is the detection of multiple biomarkers enhancing its diagnostic potential (40, 44). However, unlike radioactive tracers in PET scans, which are used at levels of 0.01% thereby creating a true “massless” tracer, in some in vivo ^{13}C NMR experiments the plasma substrate concentrations are an order of magnitude higher during the infusion (45) and therefore cannot be

considered a tracer in the true sense of the word (20). Higher field magnets used in animal studies and attention to these steady state issues insure accurate interpretation of the in vivo ^{13}C NMR experimental results.

Dynamic PET imaging in humans is used to obtain rates of glucose uptake in the brain (49). A three-compartment model, which includes the blood–brain barrier, is used for the analysis and is applied to each voxel using a bolus of ^{18}F -FDG (49). However, only a single flux is measured, so fluxomics is not possible with PET. Fluorescence spectroscopy has long been used to obtain rates in isolated cells, but typically pure enzymes or cell preparations are used for enzyme kinetics. Optical imaging is increasingly being used in whole animals and should become useful for determining some rates, but is limited by the ability to detect light due to quenching, especially in deep tissue. Therefore, optical imaging is not as useful in determining kinetics of enzymes, especially in internal organs from intact organisms, as compared to NMR. Also optical methods as well as ultrasound are not amenable to the determination of multiple rates, which is easily accomplished with ^{13}C NMR (50) and will be reviewed in depth in Sect. 6.

2.1.1. Stable Isotopic Labels and ^{13}C NMR Spectroscopy

NMRS generates positional information using stable nonradioactive isotopes such as ^{13}C , ^{15}N , and ^2H . Metabolic flux information is encoded in the isotopomers (i.e., isotope isomers or isomers of a chemical composed of varying isotopes $^{13}\text{C}/^{12}\text{C}$, $^{15}\text{N}/^{14}\text{N}$, $^{17}\text{O}/^{16}\text{O}$, etc.) that are generated during metabolism and permits the quantification of “relative” fluxes via isotopomer ratios. Absolute flux is obtained by measuring isotope incorporation rates dynamically (i.e., over time) resulting in a rate constant which when multiplied by concentration results in the absolute flux (see Sect. 2.2). A powerful NMR-observable nuclei in determining metabolic flux is ^{13}C because: (1) it is a naturally abundant tracer (1.1% of all carbons), (2) positional information is generated with superior resolution along the α -axis (chemical shift), which is at least fourfold greater than ^1H and is far less complex due to inherently fewer coupling partners with superior line widths (see Chap. 3), (3) it has greater sensitivity compared to other common NMR-observable nuclei common in biochemistry, such as ^{15}N , ^{17}O , and (4) compared to in vivo ^1H NMRS, it does not require solvent suppression.

What the ^{13}C isotopes provide in metabolic experiments is positional information on isotopomer enrichments. Both the ^{13}C and ^1H NMR spectra can aid in determining ^{13}C isotope enrichments, which can vary from 1.1 to 100% (51). Fractional enrichment is defined as the number of molecules with a ^{13}C spin in a given position (label coming from introduced precursor as well as natural abundance), divided by the total number of molecules in the pool. Absolute fractional enrichment is the enrichment above the background natural abundance, which is subtracted from the

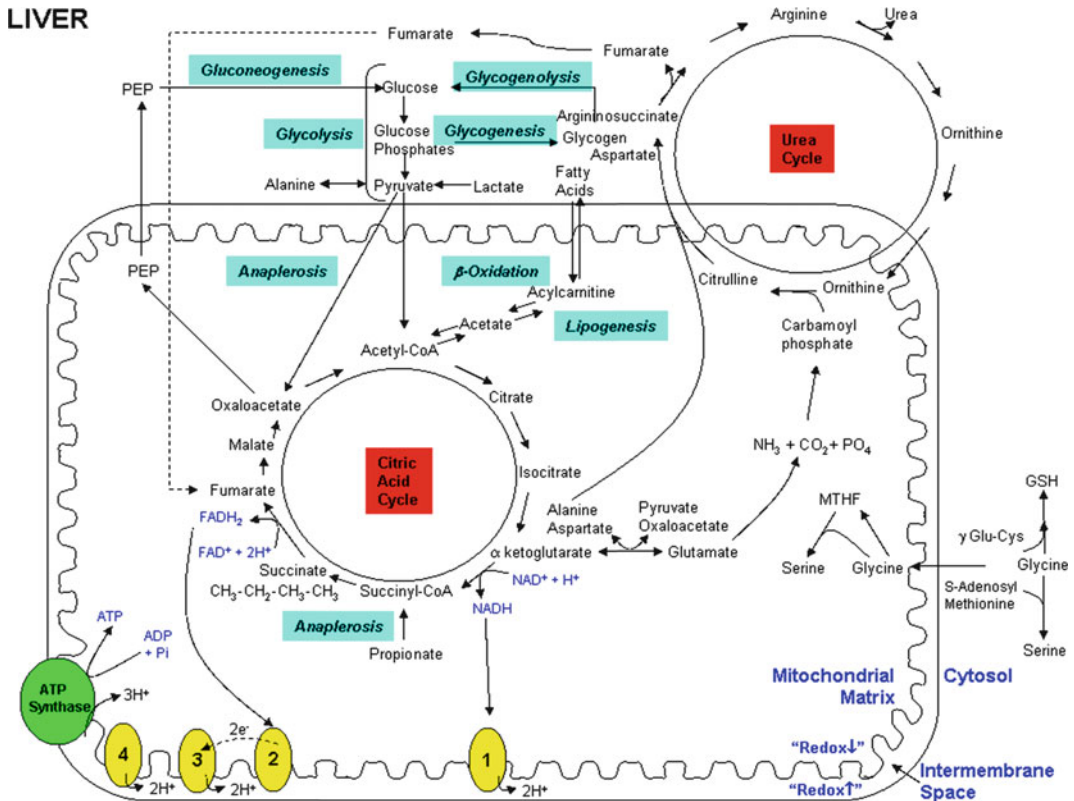


Fig. 2. Biochemical scheme for liver metabolism. The liver is a major organ for nitrogen balance (urea cycle), glucose homeostasis (gluconeogenesis), and lipid homeostasis, including beta-oxidation. Oxidative phosphorylation via the electron transport chain and ATP synthase is shown on the *bottom left*. PEP phosphoenolpyruvate; GSH glutathione; MTHF methyltetrahydrofolate.

total (51); this is solely caused by the metabolism and incorporation of the administered ^{13}C -labeled molecule. Obtaining an absolute fractional enrichment for a particular metabolite therefore allows fluxes to be measured typically via dynamic methods. On the other hand, in order to determine relative flux, isotopomer analysis is executed within a single spectrum. Numerous isotopomers observed within one data set allow for relative ratios to be established between them. Classically, such isotopomer analysis finds applications in static measurements, although dynamic measurements have also been done. NMR methods for determining isotopomer fractional enrichments have been extensively reviewed elsewhere (20, 21, 51, 52). For single time point analysis, flux ratios can only be calculated at isotopic steady state

In vivo ^{13}C NMRS is a powerful technology in metabolic engineering for metabolic flux and control analysis where prokaryotes are used to produce proteins and the majority of the fluxome is experimentally measured (8, 52, 53). In mammals, using 2- ^{13}C -glucose multiple net fluxes are quantified for various pathways and

can be used to determine metabolic flux through various reaction pathways including gluconeogenesis, glycolysis, Krebs' cycle, and the pentose phosphate pathway (PPP) (54–62). Figure 2 depicts a biochemical schematic of the many biochemical reactions that have been quantified by in vivo NMRS in liver. However, these fluxes for the various reactions depicted in Fig. 2 have not been measured simultaneously by in vivo NMRS. Therefore, fluxomics remains to be performed by this method.

A key reaction in the Krebs cycle is the formation of succinate (Fig. 2), which is a symmetric molecule and ultimately will create multiple glutamate isotopomers that can be used to determine Krebs' flux (54, 63). This is described in Chap. 14 by Fan. Biochemical reactions with high activation energy are accelerated by enzymes, which lower the activation energy. Coupling an energetically unfavorable to a favorable reaction, such as the hydrolysis of ATP, drives biochemical reactions to completion. The coupling is catalyzed by an enzyme or system of enzymes. ATP is made primarily by glycolysis and by oxidative phosphorylation. In glycolysis, ATP is generated from ADP and inorganic phosphate by substrate-level phosphorylation, which utilizes energy released during the oxidation of glucose via the glycolytic reactions. In oxidative phosphorylation, energy from the Krebs cycle is transferred to the respiratory chain by electron shuttles, which creates an electrochemical gradient between the inner and outer leaflet of the inner mitochondrial membrane (Fig. 2). The phosphorylation of ADP is catalyzed by ATP synthase by coupling to the reduction of oxygen to water and this is where most ATP is created in a normal cell (Fig. 2). Moving reducing equivalents (electrons) generated from glycolysis across the mitochondrial membrane depends on shuttles (i.e., malate-aspartate, α -glycerol-phosphate), which require compartmentation of cytosolic and mitochondrial enzyme isozymes for the same reaction. For example, in Fig. 2, two transaminases are shown for the formation of aspartate and alanine from their ketoacids. Therefore, isozymes with similar functions exist in both mitochondrial and cytosolic compartments (114, 170). Figure 2 shows aspartate exiting the mitochondria and entering the urea cycle. Aspartate can also reform oxaloacetate via the cytosolic aspartate transaminase, which in turn is reduced by NADH to malate via malate dehydrogenase and malate reenters the mitochondria shuttling cytosolic reducing equivalents. Measuring redox invasively requires quantifying redox couples in mitochondria and cytosol (64) or use of fluorescence markers (65). Indeed, the action of these shuttles and functional electron transport within the mitochondria are necessary for the continued function of glycolysis in the cytoplasm. In the early 1980s, Robert E. London not only pioneered the use of glutamate and glutamine isotopomers to determine Krebs' flux (54) along with Shulman (63), but also was the first to use ^{13}C -labeled nicotinic acid (essentially vitamin B₃ or

niacin) which is incorporated into NADH and ultimately could be used to extrapolate the intracellular redox state from the NADH/NAD⁺ ratio (66). NADH is used to drive the electron transport chain and ultimately drives oxidative phosphorylation (Fig. 2). Other redox couples have been used to measure redox state such as lactate-pyruvate, acetoacetate, and β -hydroxybutyrate (67) and oxidized to reduced glutathione (68), which are included in Table 1. In addition, the oxygenation state of myoglobin (69) and hemoglobin (70) has been measured by ¹H NMRS. The problem with the NMR measurement of these couples is that they are typically a global measurement and do not distinguish between different compartments, resulting in an averaged overall total cellular ratio affected by the total volume of the various cellular compartments.

2.2. Metabolic Steady and Nonsteady State Conditions: Example of Hepatic Glucose Metabolism

Organisms in their natural environment are in a chronic nonsteady state predictably changing diurnally and unpredictably changing in response to nutritional status and energy demand, which requires substrate fluxes to change by as much several orders of magnitude. A complex metabolic regulatory network controls flux, and this is dominated by a network of signaling pathways in which the enzymes are regulated by interactions with metabolites. This includes covalent modification of kinases via phosphorylation/dephosphorylation, as well as noncovalent (“allosteric”) interactions. The latter includes feedback inhibition or activation of key homeostatic enzymes such as PFK-1 (activated by fructose 2,6 biphosphate, and inhibited by ATP and citrate). In both cases, metabolic regulation is exerted by changes in enzyme activity due to interaction with metabolites.

Although normal metabolism is in nonsteady state most of the time, experimentally, fluxes are best measured at steady state. This is due to the mathematics used, which becomes analytically unmanageable without steady state assumptions. For a linear system, the formal math is rather simple, but the algebra is very tedious. Nonlinearity complicates the treatment of metabolic systems, and regrettably (for modelers), many parts of metabolism are inherently nonlinear. Specifically, the overall enzyme activity will depend on the enzyme, reactant, and product concentrations, but also on allosteric and nonallosteric effectors that may lead to inhibition or activation effects, generally controlled by signaling pathways. This process can be written according to a simple interconversion between reactant and product ratio:



where v_f and v_r are the enzyme-catalyzed rates in the forward and reverse direction, respectively.

Table 1
Metabolic investigations of liver

Animal intact isolated tissue extract	Treatment	Metabolic pathway measured	Stable isotopic tracer	Rate/outcome	References
Human	Normal (fed, fasted)	Glycogenesis	Natural abundance	Surface coil; Hepatic glycogen repletion rate of 0.2 mM/min/ g of liver (normal hepatic glycogen ~230 mM)	(173)
Human	Normal	Glycogen	Natural abundance	Direct and proton-detected ¹³ C pulse sequences detected glycogen	(174)
Baboon (intact)	Normal (fasted)	Glycogenesis	[1- ¹³ C] Glucose	Surface coil; direct (65%)/indirect (35%) glycogenesis	(175)
Human	Normal (fed, fasted)	Glycogenesis Glycogenolysis	[1- ¹³ C] Glucose	Under net glycogenesis in humans, glycogen syn. and degradation occur simultaneously; Net glycogenesis is 0.24 μmol/mL of liver per minute in fed state vs. 0.28 in fasted state	(176)
Rabbit (intact, tissue, and extract)	Normal (fed)	Glycogenesis	Natural abundance	Surface coil; Hepatic glycogen levels monitored	(177)
Rabbit (intact and extract)	Normal (fed)	Glycogen	Natural abundance	¹³ C NMR signal of glycogen C-1 100% visible using in vivo and nat. abundance	(98)
Rabbit (extract)	Normal (fasted)	Krebs'	[U- ¹³ C] Lactate	Krebs' flow rates; Glutamate labeling by lactate at rate of ~6.0 μmol/ kg/min	(178)

(continued)

Table 1
(continued)

Animal intact isolated tissue extract	Treatment	Metabolic pathway measured	Stable isotopic tracer	Rate/outcome	References
Rat (intact and tissue)	Normal (varied diet)	Lipids (triglycerides and phospholipids) Glycogenesis Glycogenolysis Gluconeogenesis	Natural abundance	Surface coil; monitor effects of dietary fat (lipids like triglycerides and phospholipids) and carbohydrate dietary modifications	(179)
Rat (intact and extract)	Normal (fasted)	Ketogenesis Krebs'	[1- ¹³ C] Butyrate	Surface coil; Observe ketone body formation via carbonyl spectral region	(180)
Rat (isolated)	Normal (fed)	Krebs'	[2- ¹³ C] Acetate	C-4 of glutamate labeled first; monitor glutamine-glutamate futile cycling	(181)
Rat (extract)	Normal (fasted)	Glycogenesis	[1- ¹³ C] Glucose	One-third glycogenesis via direct pathway; large amount of glycogen synthesis via another	(62)
Rat (intact and extract)	Normal (fasted, fed)	Krebs' Gluconeogenesis	[3- ¹³ C] Alanine	Surface coil; Alanine flows mostly through PC and not PDH	(182)
Rat (extract)	Normal (fasted)	Glycogenesis	[U- ¹³ C] Glucose	35% of glycogen synthesized via direct pathway	(183)
Rat (extract)	Normal (fasted)	Krebs' Glycogenesis	[1- ¹³ C] Glucose	34% glycogen synthesized directly; Alanine and lactate contribute 55% to glycogen formation	(184)
Rat (extract)	Normal (fasted)	Krebs' Gluconeogenesis	[2- ¹³ C] Acetate	7% glucose carbons from Krebs' cycle	(185)
Rat (intact and extract)	Normal (fed, fasted)	Glycolysis Glycogenesis β-Oxidation	[1,2,1,1,12- ¹³ C ₄] Dodecanedioic acid [1,2- ¹³ C ₂] Glucose [1,6- ¹³ C ₂] Glucose	Apply multilabeled substrates; ¹³ C- ¹³ C spin couplings distinguish between endogenous metabolites vs. others	(186)

Rat (intact and extract)	Normal (fasted)	Gluconeogenesis Glycogenesis	[3- ¹³ C] Alanine [1- ¹³ C] Glucose	Surface coil; 0.075 vs. 0.025 per minute of direct vs. indirect glycogen synthesis (187)
Rat (intact and tissue)	Normal (fed, fasted)	Glycogenesis Glycogenolysis	Natural abundance [1- ¹³ C] Glucose	Surface coil; novel NMR techniques involving gradients allow increased natural abundance detection (188)
Rabbit (extract) Rat (intact)	Normal (fasted)	Glycogenesis	Natural abundance [1- ¹³ C] Glucose	T_1 field dependent while T_2 is not; in vitro and in vivo measurements similar; T_1 (65 ms at 2.1 T, 142 ms at 4.7 T, 300 ms at 8.4 T) T_2 (6 ms at 2.1 T, 9 ms at 4.7 T, 9 ms at 8.4 T) (189)
Rat (extracts)	Normal (fed)	Fatty acid metabolism	[2- ¹³ C] Acetate	Quantitative measurements of exogenous acetate enable acid metabolism monitoring (190)
Rat (intact)	Normal (fed)	Glycogen	Natural abundance	Surface coil; Adiabatic RF pulses attenuate saturated carbon signals improving glycogen detection (191)
Rat (extract)	Normal (fasted)	Glycogenesis PPP	[1- ¹³ C] Glucose [6- ¹³ C] Glucose	29% direct glycogenesis; negligible amount to PPP from infused glucose (192)
Rat (isolated)	Normal (fasted)	Gluconeogenesis Krebs' PPP	[1,2,3- ¹³ C ₃] Propionate	PPP insignificant; method for determining fractional enrichment of each ¹³ C isotopomer (193)
Rat (isolated and extract)	Normal (fasted)	Gluconeogenesis Krebs'	[1,2,3- ¹³ C ₃] Propionate	Gluconeogenic flux 1.2 times Krebs' flux (0.37 vs. 0.32 $\mu\text{mol/gww/min}$) (116)
Rat (intact and extracts)	Normal (fasted)	Krebs'	[2- ¹³ C] Ethanol	Measured Krebs' flux of $0.33 \pm 0.09 \mu\text{mol/g/min}$ (194)
Rat (intact and extract)	Normal (fed)	Glucose metabolism, ascorbic acid metabolism	[1,2- ¹³ C] Glucose [1- ¹³ C] Glucose	Turnover rate of hepatic ascorbic acid (vitamin C) in vivo: $1.9 \pm 0.4 \text{ (nmol/min/g)}$ (195)

(continued)

Table 1
(continued)

Animal intact isolated tissue extract	Treatment	Metabolic pathway measured	Stable isotopic tracer	Rate/outcome	References
Rat (intact, isolated, and extract)	Normal	Lipogenesis β-Oxidation Lipolysis	[1- ¹³ C] Arachidonic acid and [3- ¹³ C] γ-linolenic acid	Mobility and turnover of tissue lipids	(196)
Rat (intact and extract)	Normal	Glutathione metabolism	[2- ¹³ C] Glycine	GSH fractional isotopic enrichment at rate 0.316 per hour	(45)
Mouse (isolated)	Normal (fasted)	Krebs' Gluconeogenesis	[3- ¹³ C] Alanine [2- ¹³ C] Ethanol	Krebs' entry when both alanine and ethanol present; alanine enters via carboxylation of pyruvate and ethanol via acetyl-CoA	(80)
Mouse (isolated)	Normal (fasted)	Glycogenesis Glycogenolysis Gluconeogenesis Recycling of triacylglycerols	[2- ¹³ C] Glycerol [1,3- ¹³ C] Glycerol	Gluconeogenic flux from glycerol followed	(117)
Human	Normal vs. glycogen type IIIA storage disease	Glycogenesis Glycogenolysis	Natural abundance	Surface coil; dietary and exercise effects; glycogen level 2–3 times higher in disease state	(197)
Human	Normal vs. hepatic steatosis	Lipogenesis	Natural abundance	Hepatic triglycerides determination (range of hepatic fat content values for several patients)	(198)
Human	Normal (fed, fasted); insulin and glucagon	Glycogenesis Glycogenolysis Gluconeogenesis	Natural abundance [1- ¹³ C] Glucose	Insulin and glucagon influences on glycogenesis and turnover rates (many rates given)	(199)
Human	4 Hypoglucagonemic conditions (fasted); insulin and glucagon	Glycogenesis Glycogenolysis	[1- ¹³ C] Glucose	Surface coil; Extensive flux rates in table (e.g., range for net glycogenesis: −0.25 to 0.36 mmol L of liver per minute)	

Rat (intact and extract)	Normal (fed, fasted) vs. phosphorylase kinase deficiency (<i>gsd/gsd</i>)	Glycogen	Natural abundance	Surface coil; 3× normal glycogen in <i>gsd/gsd</i> strain; NMR can diagnose glycogen storage disease (200)
Rat (isolated and extract)	Normal (fasted); with and without insulin	Gluconeogenesis Glycogenesis Glycogenolysis Krebs'	[2- ¹³ C] Pyruvate [1,2- ¹³ C] Ethanol	³¹ P and ¹³ C both recorded glycogen increase at 17 μmol of glucose units/g of liver/h and glucose increased at 17 μmol/g of liver/h (76)
Rat (isolated and extract)	Normal (fed); glucagon	Glycogenolysis Glycolysis Glycogenesis	Natural abundance [1- ¹³ C] Glucose	Glycogen T ₁ 's (0.11–0.24 s) and T ₂ 's (16–31 ms) for in situ and in vitro measurements (201)
Rat (intact)	Normal (fed, fasted); glucagon	Glycolysis Glycogenesis Glycogenolysis	Natural abundance [1- ¹³ C] Glucose	Surface coil; monitor C-1 carbons of glucose to glycogen (202)
Rat (intact)	Normal (fasted); glucagon and insulin	Glycogenesis Glycogenesis Glycogenolysis	[1- ¹³ C] Glucose	Insulin and glucagon effects on glucose; glycogen synthesis increases linearly with glucose concentration (203)
Rat (intact and extract)	Normal (fasted) vs. diabetic	Ketogenesis Krebs' Gluconeogenesis	[1,3- ¹³ C] Butyrate [3- ¹³ C] Butyrate [1- ¹³ C] Butyrate	Surface coil; Disposal of acetyl-CoA different between fasted/fed rats (204)
Rat (intact, tissue, and extract)	Normal (fasted) vs. diabetic	Ketogenesis Krebs' Gluconeogenesis	[1,3- ¹³ C] Octanoate	Surface coil; Ketone body production control in inner mitochondria space (205)
Rat (isolated)	Normal (fed, fasted) vs. diabetic; insulin	Gluconeogenesis Krebs'	[3- ¹³ C] Alanine [2- ¹³ C] Pyruvate	Pyruvate kinase flux = 0.74 of gluconeogenic rate in liver of controls; undetectable in diabetes (206)
Rat (isolated and extract)	Normal (fed, fasted) vs. diabetic	Krebs' Lipogenesis	[3- ¹³ C] Alanine	Flux through Krebs' of PDH vs. PC for control fed (1:1.2), control fasted (1:7.7), diabetic (1:2.6) (207)
Rat (isolated and extract)	Normal (fasted) vs. diabetic	Gluconeogenesis Krebs'	[3- ¹³ C] Alanine [2- ¹³ C] Pyruvate	Diabetic gluconeogenesis 2–4-fold greater compared to control (206)

(continued)

Table 1
(continued)

Animal intact isolated tissue extract	Treatment	Metabolic pathway measured	Stable isotopic tracer	Rate/outcome	References
				(diabetic 52 vs. control 24) units of [$\mu\text{mol(g of liver per wet weight)}/\text{h}$]	
Rat (isolated)	Normal (fasted); insulin	Glycogenolysis Glycogenesis	[1- ^{13}C] Glucose [3- ^{13}C] Alanine [3- ^{13}C] Lactate	Net glycogenesis rate is 0.1–0.15 $\mu\text{mol/g/min}$	(208)
Rat (intact, tissue, and extract)	Normal (fed, fasted) vs. diabetic	β -Oxidation Krebs' Ketogenesis	[1,12- $^{13}\text{C}_2$] or [1,2,11,12- $^{13}\text{C}_4$] dodecanedioic acid	Metabolism differences between monocarboxylic acids and dicarboxylic fatty acids	(209)
Rat (isolated)	Normal vs. tumor (fasted)	Gluconeogenesis Glycogenesis	[3- ^{13}C] Alanine	Tumor cells show changes in hepatic metabolism of alanine; also decreased glycerol utilization and Krebs' cycle	(210)
Rat (intact)	Normal (fed, fasted); insulin	Glycogenesis Glycogenolysis	[1- ^{13}C] Glucose [2- ^{13}C] Glucose	Compared fed and fasted; glycogenesis (0.3 $\mu\text{mol/min/g}$) vs. glycogenolysis (0.045 $\mu\text{mol/min/g}$) for fasted rats	(211)
Rat (intact and extract)	Normal (fed, fasted); [1,3- ^{13}C] ribose	Glycogenesis	[1,2- ^{13}C] Glucose	Fed rats: Direct pathway (67%), no indirect detected; Fasted rats: Direct pathway (13%) and some via indirect	(212)
Rat (isolated)	Normal vs. tumor (fasted)	Gluconeogenesis	[3- ^{13}C] Alanine	Increases [3- ^{13}C] aspartate production and demonstrates increased PC activity in tumors	(213)

Rat (extract)	Normal (fasted); insulin	Gluconeogenesis	[1- ¹³ C] Glucose	Hyperglycemia under hyperinsulinemia shows increased hepatic glycogen via direct pathway; glycogenesis rates of 0.16, 0.41, 0.13 μ mol glucosyl U g/liver/min under various conditions	(214)
Rat (intact and tissue)	Normal (fed); 2,2- dichloro-1-(2- chlorophenyl)-1- (4-chlorophenyl)- [3- ¹³ C]-pronane [¹³ C-DDP]	Xenobiotics	¹³ C-DDP	Surface coil; No metabolites detected; Monitor drug induced intrahepatic changes for 12 days	(215)
Rat (intact and tissue)	Normal (fed); 1-(<i>o</i> - chlorophenyl)-1-(<i>p</i> - chlorophenyl)-2,2- dichloro-3- ¹³ C- propane	Xenobiotics	¹³ C-DDP	Surface coil; xenobiotic product can be followed noninvasively	(216)
Rat (isolated and extract)	Normal (fasted) vs. triiodothyronine treated, hydroxymalonnate	Glycolysis Gluconeogenesis Krebs'	[3- ¹³ C] Alanine	Flux through pyruvate kinase + malic enzyme to PC 0.18 \pm 0.04 in normal rats vs. 0.44 \pm 0.08 in treated; following hydroxymalonnate addition, <i>T</i> ₃ treated flux decrease to 0.15 \pm 0.04	(217)
Rat (intact and extract)	Normal vs. ischemia (fasted)	Krebs' Glycogenesis Gluconeogenesis	[1- ¹³ C] Glucose	Glucose and energy metabolism indicates ATP level participates in glycogenesis and gluconeogenesis in liver	(218)
Rat (intact and extract)	Normal vs. endotoxemia (fasted)	Gluconeogenesis Krebs'	[3- ¹³ C] Alanine	Endotoxin cause inhibition of gluconeogenesis activity and Krebs' cycle	(219)

(continued)

Table 1
(continued)

Animal intact isolated tissue extract	Treatment	Metabolic pathway measured	Stable isotopic tracer	Rate/outcome	References
Rat (intact and extracts)	Normal pregnancy (ad libitum vs. routine meal feeding) (fed, fasted)	Glycogenesis	[1- ¹³ C] Glucose	Meal feeding regimes in pregnant rats have increased glycogenesis as compared to ad libitum diets	(220)
Rat (intact and extract)	Burn vs. sham (fasted)	Gluconeogenesis Krebs'	[U- ¹³ C] Lactate	Up-regulation of gluconeogenesis and pyruvate to oxaloacetate at expense of non-Krebs' sources; Increased gluconeogenesis from lactate; Table of fluxes	(221)
Rat (extract)	Burn vs. sham (fasted)	Gluconeogenesis Krebs' cycle	[1,2,3- ¹³ C] Propionate	Gluconeogenesis vs. Krebs' not altered by burn; Burn trauma stimulate hepatic anaplerosis	(222)
Rat (intact and isolated)	Normal (fed); insulin and glucose	Glycogenolysis	Natural abundance	Glycogenolysis in control: $-0.53 \pm 0.021\%/min$	(223)
Mouse (isolated and extracts)	Normal vs. malaria (fasted)	Gluconeogenesis Krebs'	[2- ¹³ C] Pyruvate	56% reduction of glucose production in malarial animals	(224)
Mouse (isolated)	Normal vs. disease (African trypanosomes)	Krebs'	[3- ¹³ C] Alanine	Disease causes no permanent damage to hepatic alanine metabolism	(225)
Mouse (isolated)	Normal vs. leukemia (fasted)	Krebs' Gluconeogenesis Glycolysis	[3- ¹³ C] Alanine [1- ¹³ C] Glucose	Gluconeogenesis rate lower for leukemia; 34.0 ± 8 vs. $4.0 \pm 2 \mu mol$ glucose/h/g for control vs. leukemia	(226)

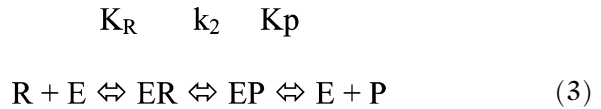
Mouse (isolated and extract)	Normal vs. <i>Ob/ob</i> mouse model of obesity and insulin resistance; glucagon	Lipogenesis Gluconeogenesis	[2- ¹³ C] Pyruvate	Leptin influence on hepatic metabolism monitored; Gluconeogenesis in control, leptin in vitro, and leptin in vivo over 3 h was, respectively, 0.56, 0.75, and 1.18 μmol/gww/min	(227)
Mouse (intact)	Normal vs. diabetes (fasted)	Glycogenesis Gluconeogenesis	[1- ¹³ C] Glucose	Net glycogen synthesis rate 2× higher ADM group vs. control	(228)
Mouse (isolated)	Normal (express human glucagon receptor); glucagon; several antagonists	Glycogenolysis Gluconeogenesis	[3- ¹³ C] Pyruvate	Efficacy of glucagon receptor antagonists at different concentrations	(229)

Allosteric and nonallosteric effectors modulate the reaction rates by acting on the enzyme. Rate and flux may be defined by analogy to the two types of electricity, direct current (DC) vs. alternating current (AC). Rate and flux have the same units, which are typically gram or moles per unit time per cell number or weight of tissue—or some other measure of tissue volume such as grams of protein or DNA or cell number. In this model, the net flux, J , is the difference between the two unidirectional rates, i.e.,

$$J = v_f - v_r \quad (2)$$

Net flux is sometimes used to define the total flux through a metabolic pathway, in the same manner as rate is used, as some of the individual fluxes can be in reverse of the net flux direction for the entire metabolic pathway. Also, “flux rate” is often used to define flux. In fact, when performing a kinetic study on an isolated enzyme, generally only the enzyme and substrate are present initially and the “initial velocity,” v_0 , of product formation is measured in the form of millimoles or milligrams of product per unit time at a given enzyme concentration. This in fact is a rate according to our definition.

The simplest possible mechanism for a single substrate single product reaction as in the above scheme is as follows:



k_{-2}

where R , E , and P represent reactant, enzyme, and product, respectively. Under the simplifying assumption that reactants and product very rapidly equilibrate with the enzyme, the initial velocities (rates) in the forward and reverse direction are given by:

$$v_f = dp/dt = k_2 e_t r_0 / (K_R + r_0) \quad (4a)$$

$$v_r = ds/dt = k_{-2} e_t p_0 / (K_P + p_0) \quad (4b)$$

where p_0 and r_0 are the initial concentrations of R and P , K_R and K_P are the dissociation constants from the enzyme, k_2 and k_{-2} are the catalytic rate constants, and e_t is the total enzyme concentration. In general, in a cell, the initial rate conditions do not apply. More generally, the flux for the mechanism is given by:

$$J = e_t (k_2 r - k_{-2} K_R p / K_P) / [r + K_R (1 + p / K_P)] \quad (5)$$

k_2 , k_{-2} , K_R , and K_P are not all independent; they are related by the overall equilibrium constant for the reaction, which is independent of the enzyme, according to:

$$K_{eq} = (k_2 / K_R) / (k_{-2} / K_P) \quad (6)$$

This also embodies the Haldane relationship. The flux J can thus be rewritten as:

$$J = \frac{k_2 e_t r [1 - p/rK_{eq}]}{[r + K_R(1 + p/K_p)]} \quad (7)$$

Effectors can influence the value of K_R , k_2 , etc., but not K_{eq} .

Thus, the flux is determined not only by the enzyme properties (k_{cat} and K_m values), but also on the absolute concentrations of the enzyme, reactants, and the deviation or their ratio from the equilibrium value. The thermodynamic disequilibrium component is expressed in the square brackets in the numerator of (7) and this defines the direction of the reaction. Thus, if p/rK_{eq} is equal to unity, there is no net flux (the reaction is at equilibrium), whereas if it is different from unity, the reaction goes in either the forward or the reverse direction.

In the context of an isolated enzyme, at steady state, the rate of production of P is a constant. However, if the substrate is allowed to deplete, then the flux will decrease. Furthermore, the product builds up there will be product inhibition, and eventually the flux will reach zero as equilibrium is approached. In the context of a metabolic pathway, generally homeostatic mechanisms tend to maintain both r and p constant at each step along the pathway, such that at steady state, the flux at each point is the same. Only the end product of the pathway then changes as a function of time. This is described in more detail in Chaps. 1 and 9.

For example, during the short steady state that occurs after a meal, there will be a net production of hepatic glycogen, or during exercise, muscle will produce lactate. In the case of glucose after a meal, the steady state for the organism would be the point where the *rates* of intestinal absorption and hepatic liver formation of glycogen and glucose consumption do not change. In the case of exercise, the steady state could be defined at the point where the rate of lactate production and its secretion into the blood stream and the rate of kidney excretion and hepatic metabolism do not change. As mentioned above, a true steady state is rare for an organism that maintains homeostasis. However, short periods may occur, whereby a pseudosteady state can be assumed. The organism compartmentalizes these reactions in different organs or organelles, whereby one organ has a steady state production of lactate and alanine, for example muscle, and another has a steady state consumption, for example liver. In fact, this transfer of lactate and alanine to liver from muscle and then reformation of glucose and transport of glucose back to the muscle is called the Cori cycle. So, during exercise a steady state can be created even though there is a constant rate of glycogen mobilization from the liver, Cori cycling of lactate, alanine, and glucose, and a net loss of lactate from the kidneys. If the product were to accumulate in one of these organs, this would

decrease the rate of product formation according to Eq. (7) and the system would enter a nonsteady state. Organisms have evolved ingenious inter and intracellular compartmentation strategies to achieve metabolic stability, some of which are discussed in Sect. 3.3.

Using stable or radioactive isotopes, one can determine the rate, k , from the initial slope of the time course of incorporation or decay of isotopically labeled reactant. A steady state is typically maintained in perfused organs or perfused cell systems, because the concentration of nutrients in media can be maintained relatively constant, which in turn maintains constant intracellular concentrations and thus the flux does not change. The intracellular complement of small molecules is the so-called the metabolomic “fingerprint.” In batch mode where the media is changed completely at a given time interval, common in cell culture, the waste products can accumulate in the extracellular media, giving the so-called the metabolomic “footprint” and represents the secreted products or consumed nutrients by the cell (71). However, the nutrients, such as glucose, are typically at sufficiently high concentrations, near the V_{\max} , such that the fluxes do not change significantly. Although perfused cells and organs permit a reductionist approach to study metabolomics and fluxomics, ultimately the organism contains all the paracrine and endocrine signaling required for normal metabolism and must be used to obtain the complete scope of the metabolic network.

Metabolic regulation is the sum of the biochemical processes that may increase or decrease substrate flux through the various metabolic pathways and nearly always include cell signaling pathways (allosteric effectors). Besides simply increasing reactants of metabolic pathways, the enzymes can be allosterically or nonallosterically modified, whereby the enzyme is actually covalently modified to change its macromolecular structure or to increase the enzymes activity. A good example of metabolic regulation controlling the response to changes in nutritional status is that of glucose metabolism, in fed and starved states. In order to understand the change in substrate fluxes of metabolic pathways, a detailed analysis of the metabolic regulators must be included, such as, allosteric modification of transporters, signaling proteins (i.e., kinases/phosphatases), and enzymes by covalent modification such as phosphorylation or by noncovalent interactions with small molecules (<1 kDa) such as ATP. Figure 3a is a diagram of the metabolic regulation of signaling proteins and the covalent modification via phosphorylation, thus depicting the effect of hormones, insulin, and glucagon on the small molecule secondary messenger, cyclic adenine mono phosphate (cAMP). Ultimately, these hormones regulate the activity of glycogen synthase (GS) and glycogen phosphorylase (GP) as well as breakdown of triglycerides to free fatty acids (FFA) resulting in the formation of ketone bodies.

Mathematical models are used to plan ^{13}C NMR experiments and to interpret or predict the resulting data (20). The metabolic

to secrete insulin, which causes an increase in glycolysis and glycogen synthesis via allosteric dephosphorylation of glycogen synthase (GS). Upon fasting, glucagon is secreted and glycogen phosphorylase (GP) is phosphorylated, leading to increased glycogenolysis and glucose secretion so that blood glucose levels are maintained. A pseudosteady state is depicted in Fig. 3, at the fed and fasted states at the two ends of the time course, although reactant and product concentrations are changing significantly in the middle of the time course, where clearly a nonsteady state condition is apparent.

2.3. Dynamic and Static ^{13}C NMR Measurement of Flux at Steady State and Nonsteady State

In vivo fluxomics is required to noninvasively obtain mass balance in live animals. Simply measuring concentration will underestimate the total mass consumed or produced by a metabolic pathway, unless all masses entering and exiting the boundaries of the biosystem are accounted for. Quantifying all masses in a culture dish is relatively easy, whereby the edges of the media and cell mass define the boundary conditions, and metabolites are invasively quantified. However, noninvasive quantification of mass balance in a liver inside an intact animal is far more difficult. As stated earlier, substrate flux can be derived from statically or dynamically acquired NMR data. *Static* measurements consist of using a single spectrum to obtain relative fluxes. This is accomplished by analysis of the isotopomer ratios to solve for relative fluxes. At the end of the experiment, the relative fluxes are converted to absolute fluxes. This is accomplished by tissue extraction and quantification of isotope fractional enrichment of the metabolites (see Chap. 2). Typically, concentration is determined by ^1H NMR or mass spectrometry (21, 73, 74). Static measurements are obtained at a single time point once metabolic steady state ($dC/dT = 0$) and *isotopic steady state* have been attained (i.e., the point where isotope fractional enrichment of the measured metabolites does not change). This is generally in perfused organs (21) or human biofluids (75), where higher field magnets are used to resolve ^{13}C isotopomers (21, 52). However, these perfused organ models are actually at pseudosteady state (21, 76). For example, with perfused Langendorff preparations, the excised heart is taken from a condition of being bathed in a rich mixture of plasma nutrients, to a saline solution composed of a single or mixture of several nutrients. Under these conditions, the tissue relies on more on endogenous substrates (21) that are not typical of normal metabolism. Sometimes blood is used (76, 77). However, although these organs are relatively short-lived, the kinetics are rapid compared to the initial equilibrium phase of the study and are in a pseudosteady state by the time the ^{13}C studies begin (21, 78). Comparing to metabolism of whole organisms always has caveats. Mammalian animal studies are always tainted by the need for anesthesia. In short, one must always consider the limitations of the model as it relates to steady state conditions that are of physiological relevance.

Dynamic measurements of fluxes obtain multiple spectra using dynamic in vivo NMRS to measure isotope enrichment of nutrients (41, 79). This can require several hours of noninvasive monitoring of the biosystem (45). As discussed above, these studies are typically performed under pseudosteady state conditions, so concentrations do not change ($dC/dT = 0$). In contrast, at *isotopic nonsteady state* (i.e., isotope fractional enrichment of the measured metabolites is changing), the time course of isotopic incorporation can be analyzed to derive the rates of the desired metabolic reaction(s). Most *metabolic nonsteady state* NMR fluxomic studies (i.e., concentration changes during kinetic measurement) have been performed dynamically in perfused organs where substrates are controlled and have focused on substrate utilization and citric acid (aka Krebs or TCA) cycle flux (21). Dynamic NMR flux studies using intact organism have used two-state models where fluxes are measured once the new metabolome representing a pathology, nutritional status, or drug/toxicant exposure has reached a new metabolic steady state. Since both flux and concentrations are changing during nonsteady state conditions, one must obtain dynamic measurements of both concentration by ^1H NMRS and the corresponding ^{13}C NMR spectra in order to derive the changing flux in response to the changing reactant/product concentrations. This is very complex (Chap. 8). Therefore, two-state models are preferred.

2.3.1. In Vivo ^{13}C NMR Studies in Intact Mammals and Perfused Organs

In vivo ^{13}C NMRS of liver was the first organ studied by this method (80). Very soon after brain, heart, kidney, skeletal muscle, and other tissues were studied using this approach (52). Liver is the central metabolic organ for the entire organism. However, liver produces the poorest NMR spectral conditions because of movement, magnetic susceptibility issues, and short T_2 values, all of which compromise signal-to-noise ratio (SNR) and resolution. Abdominal motion of liver in vivo has been overcome by use of ex vivo perfusion, but this eliminates organ interactions present at the organismal level. The liver is the best organ to monitor for system effects on the metabolome or fluxome, because the liver is the central organ responsible for detoxification, synthesis, storage, and energy generation, and thus the hub through which all organs interact metabolically. The application of in vivo ^{13}C NMR methodology in whole animals has measured all major metabolic pathways including the Citric acid cycle, gluconeogenesis, glycolysis, β -oxidation, glycogenesis, lipogenesis, protein synthesis, nucleotide metabolism, even signaling, and fluxes simultaneously (see Table 1).

Table 1 illustrates the current state of in vivo ^{13}C liver studies in mammals. Not mentioned are other NMR active nuclei such as ^2H (81) and ^{31}P (82), which have been utilized in conjunction with ^{13}C tracers to gather metabolism data. The information in Table 1 reveals the widespread and ongoing developments in the

field. These studies started with monitoring natural abundance ^{13}C in intact animals and progressed to perfusion and infusion of ^{13}C -labeled nutrients in perfused liver and intact animals, respectively. Presently, only a few fluxes have been quantified simultaneously in the same organism with five metabolic pathways using *static* method in human biofluids (i.e., gluconeogenesis, glycogen synthesis, glycolysis, Krebs', and PPP) (75) and eight metabolites using the *dynamic* method in brain from intact rat (83, 84). Applications in the areas of diabetes, obesity, burns, leukemia, and tumors are just a few examples where these efforts have been successfully applied to liver (Table 1).

Although intact brain and perfused heart are perhaps the most published organs for in vivo ^{13}C NMRS, we have focused on thoroughly reviewing the liver literature. For reviews of in vivo ^{13}C NMR of brain (85, 86) and heart (21, 87–89), refer to the indicated literature. Table 1 presents a comprehensive review of mammalian liver in vivo ^{13}C NMR literature. Four categories of animal sample preparation are examined as indicated in the first column including “non-invasive” intact (whole animal), isolated (excised, perfused liver), tissue (excised pieces of liver tissue), and extracts (“invasive” sample preparation). Advantages and disadvantages accompany each study choice, with typically lower signal-to-noise data in whole animal studies collecting in situ data or increased resolution in isolated liver ex vivo experiments performed under certain assumptions. It is typically necessary to end each ^{13}C time course study with an extraction of the tissue to validate the noninvasive in vivo measurements.

The chronological table is divided into two groups according to treatment type. The first group encompasses normal states and is immediately followed by disease or chemical treatment conditions. Each group is arranged from the largest to the smallest mammals with the most abundant studies exploiting both intact and isolated rat livers.

Within the first normal class, subjects are either fed or fasted and various metabolic pathways are measured using stable isotopic tracers. Typical pathways studied are gluconeogenesis, glycolysis, glycogenesis, glycogenolysis, Krebs' (tricarboxylic or citric acid) cycle, and ketogenesis. Selected references analyze β -oxidation, fatty acid metabolism, and PPP, or simply demonstrate glycogen detection and no flux is measured. Employing appropriate “metabolic” tracers such as 1- ^{13}C -glucose or 2- ^{13}C -acetate among others and in all the cases not a “massless” tracer as can be assumed with radioactive isotope studies, the authors determine suitable pulse sequences and hardware choices to monitor percentages and flow rates of particular pathways.

The second group of studies primarily focuses on diabetes and the effects of insulin and glucagon on metabolism while also addressing glycogen storage disease, tumors, ischemia, burn

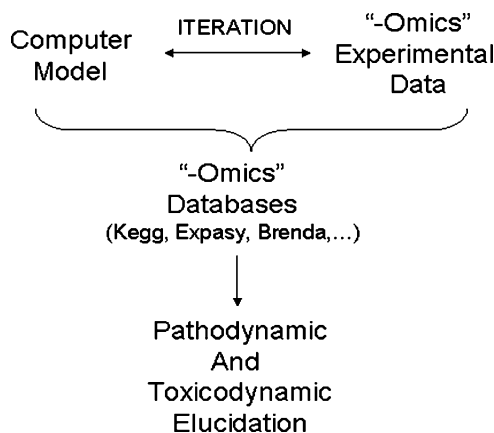


Fig. 4. Pathodynamic and toxicodynamic algorithm.

injuries, and malaria. Similar isotopic tracers as in the normal experiments are utilized with multiple tracers such as 3- ^{13}C -alanine and 2- ^{13}C -pyruvate in single studies becoming prominent. Turn-over rates, T_1 and T_2 measurements, and drug xenobiotics are monitored in the previously mentioned metabolic pathways.

2.3.2. *In Silico* Mass Balance Models and Algorithm for Toxicodynamics and Pathodynamics

In general, the global analysis accrued by the “-omics” experiments can be arrayed with computational analysis and metabolic databases, to elucidate etiologies of disease and toxicity by defining the cascade of pathological or toxic events. Figure 4 is the “-omics” toxicodynamic or pathodynamic algorithm incorporating the global analysis of all the “-omics” methodologies in an iterative manner with mathematical modeling with the goal of identifying the upstream and downstream toxic or pathological events that define the etiology of toxicity or pathology. Similar to macromolecular structure determination algorithms, empirical data impose constraints on the computer calculations macromolecular structure (90). However, unlike the structure determination algorithm, the “-omics” algorithm has significant dynamic events that occur at a different time scale, a period of seconds to years rather than picoseconds, depending on acute or chronic aspects of the study. To first create these models from scratch, one must perform metabolic reconstruction using metabolic pathway databases, such as KEGG, which can be queried to list the metabolic connections to a substrate, thereby generating your network (91). Next, the boundary conditions of the biosystem must be defined. For example, in a perfused liver system, one can consider the liver “well-stirred” (i.e., homogeneous), and have a three-compartment model defining the boundary conditions: the perfusate, the hepatocytes, and the mitochondria within the hepatocytes. In dynamic PET imaging of the brain, (described in Sect. 1), a three-compartment model was used to define the boundary conditions such as the blood–brain barrier,

the plasma in the brain, and the brain cells (49). Finally, a network that includes the signaling molecules as well as the micromolecules creating the architecture of the mathematical model is derived and translated into a computer program permitting input and output, as shown in Sect. 2.2 (Fig. 3).

3. Examples of ^{13}C NMR Studies

3.1. Dynamic Measurements

As an example of the dynamic NMR measurement, an in vivo ^{13}C NMRS study of liver from anesthetized rats infused with 2- ^{13}C -glycine is used in order to illustrate the various parts of the experiment. The steady state study was performed by (45) and the non-steady state study was performed as part of Dr. Macdonald's doctoral work in Dr. T.L. James laboratory (92). Although dated, these studies illustrate the multiple hurdles one must consider in performing dynamic in vivo ^{13}C NMR studies.

3.1.1. Steady State, Dynamic Measurements from In Vivo ^{13}C NMR Spectral Time Course Datasets

Figure 5 shows in vivo ^{13}C NMR spectra of liver from intact rat obtained using an implanted surface coil localized to the liver (45) prior (Fig. 5b) and 4 h after (Fig. 5a) 2- ^{13}C -glycine infusion (4.4 mM/kg/h), and the high resolution ^{13}C NMR analysis of the perchloric acid extract of the liver (Fig. 5c) corresponding the 4 h time point (Fig. 5a) (figure taken from (92)). Note the superior spectral

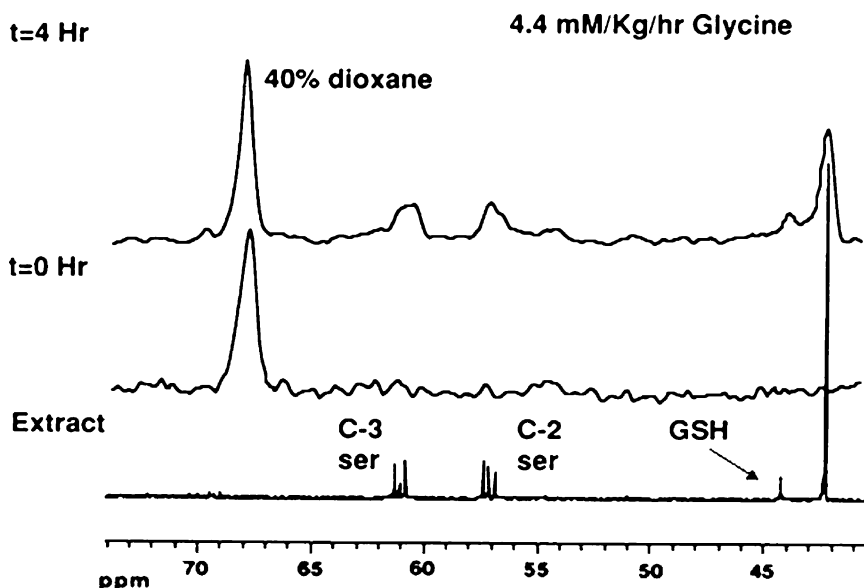


Fig. 5. ^{13}C NMR spectroscopy of rat liver. In vivo ^{13}C NMR spectra (*top, middle*) and the high resolution ^{13}C NMR spectrum of the perchloric acid extract (*bottom*) from an anesthetized rat infused with 2- ^{13}C -glycine. Modified from (92). *Gly* glycine; *GSH* glutathione; *C-2 ser* C2 carbon of serine; *C3 ser* C3 carbon of serine.

resolution of the perchloric acid extract, demonstrating the effect of iron and motion in decreasing the in vivo T_2 and the T_2^* values (see Chap. 6, for causes of inhomogeneity associated with T_2^*). One notes the increase of four sets of peaks [C2 ser ($2\text{-}^{13}\text{C}$ -serine), C3 ser ($3\text{-}^{13}\text{C}$ -serine), GSH ($[2\text{-}^{13}\text{C}\text{-glycyl}]\text{glutathione}$), and Gly ($2\text{-}^{13}\text{C}$ -glycine)], with a fifth peak 40% dioxane which is present in vivo but not in the perchloric acid extract. This section will explain the analysis of the peaks representing GSH, Gly, and 40% dioxane. Section 3 describes the analysis of the triplet of C2-Ser and C3-Ser in the perchloric acid extract (Fig. 5c). Clearly, the relatively large amount of glycine infused in conjunction with relatively similar kinetics as that of glycine resulting in poor temporal resolution means serine is not at metabolic steady state. Although plasma glycine concentration was not determined, a quick estimation of 4.4 mM/kg/h or about 1.1 mM/h for these 250 g rats infusing into about a 10 mL blood volume would result in 110 mM if it were not metabolized or excreted by the kidneys. The blood concentration of glycine is about 0.3 mM (93). The caveats for why glutathione is at a pseudosteady state are described below and are very important to understand: (1) the glycine is at the V_{max} of glutathione synthetase, and (2) the temporal resolution is sufficient to derive the rate.

3.1.2. Peak Area Determination from Dynamic In Vivo ^{13}C NMR Spectra

The 40% dioxane peak (Fig. 5a, b) is an external standard and that is why it is not present in the perchloric acid extract (Fig. 5c). The external standard is used for quality control and quantification. For example, if experimental conditions suddenly degrade the spectral quality due to pulses affected by detuning of the circuit or uncharacteristic tissue movement, the standard will also be affected, and it is assumed in the same manner as the in vivo peaks of interest. In some cases, an internal standard such as choline *N*-methyl carbons resonances at 54.6 ppm can be used as a reference or calibrant (94); however, an external standard is most commonly used. Typically, a magnetic glass capillary or sphere is placed between the tissue of interest and the NMR probe (45). Magnetic susceptibility effects (see Chap. 6) are still present even with proper placement and container shape, especially for surface coil liver analysis, so the chemical shift difference from pure dioxane can be as much as 0.3 ppm in error, e.g., 68.7 vs. 69.0 ppm.

The peak areas of glutathione and glycine were compared to the dioxane peak area resulting in a peak area ratio that is plotted with respect to time. The temporal resolution of this study was 10 min, and it is important to have sufficient temporal resolution in order to obtain at least four points defining the curve, preferably eight points or more, especially if there is more than one rate that requires derivation. For the peaks representing C-3 ser and C-2 ser, this temporal resolution would need to be at least 3 min in order to analyze the rapid kinetics of serine formation. Also, as mentioned above, serine is not at steady state and would belong in the

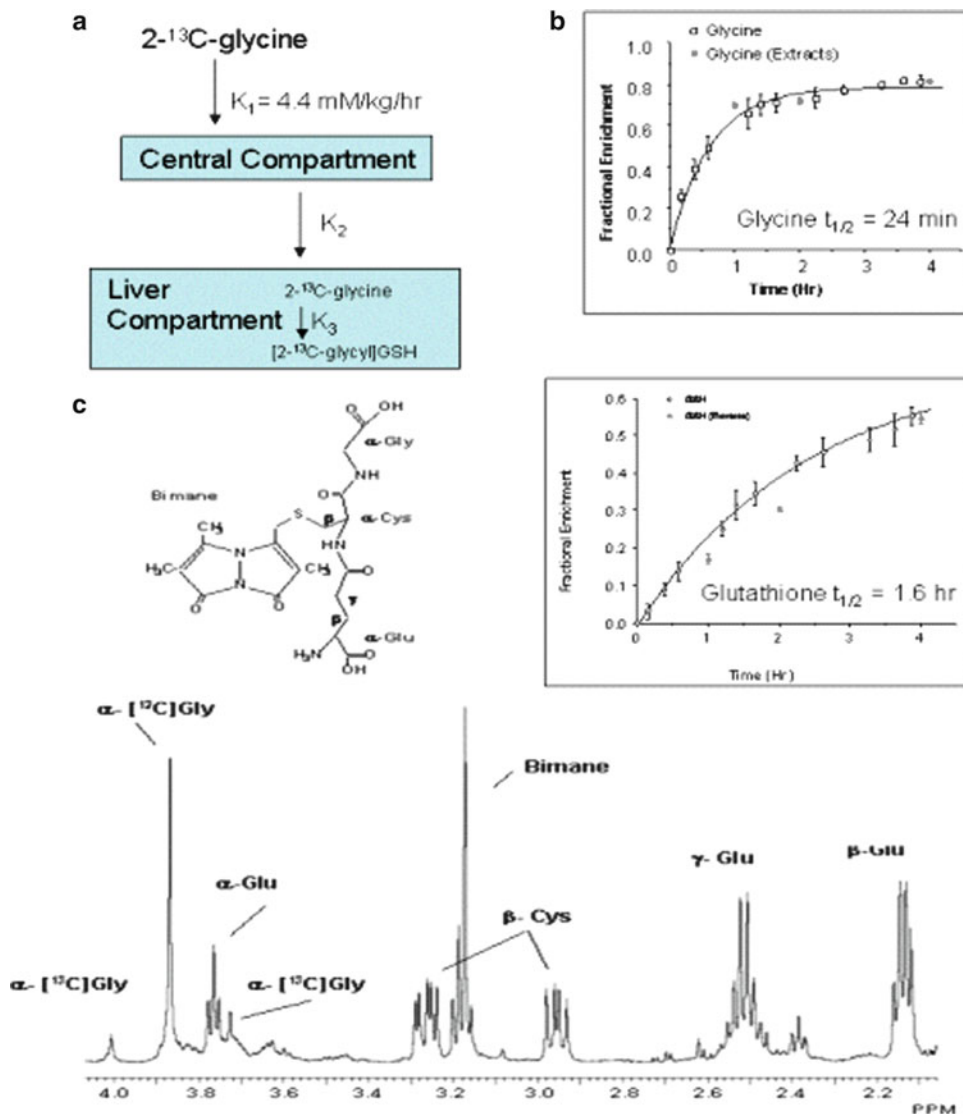


Fig. 6. Compartment Model. (a) Definition of kinetic parameters. (b) Time courses of ^{13}C enrichment in glycine and glutathione with fits defined by the model in (a). (c) Structure of bimane and proton spectrum showing fractional enrichments. From ref. (45).

following section on nonsteady state kinetics. Various commercial vendors specialize in software for NMR analysis, and the NMR processing software packages are available, (LCModel, ACD), and some have free downloadable 1D processing versions online (Mestrec, Acorn NMR, Swan, NMR Pipe). MacFid (Tecmag Inc., Houston, TX) was used on a MacIntosh computer to fit the peaks in the study shown in Figs. 5 and 6.

The area of the various peaks appearing in a series of in vivo ^{13}C NMR spectra recorded over a period of time can be *integrated* or determined with a least squares fitting algorithms, known as peak

fitting or *deconvolution*. *Deconvolution* is used when there are overlapping peaks that are not baseline resolved. Deconvolution is a peak fitting procedure in which a Gaussian or Lorentzian (or commonly a combination of the two) peak shapes plus, in some cases, a baseline function is iteratively fitted to the experimental spectrum using a least squares criterion for example. The peak areas are recovered from the best fit. *Integration* is a point-by-point summation of area. Integration can be done by linearly interpolating the point (trapezoid rule) or polynomial interpolation (Simpson's rule), but both have systematic errors associated with baseline offset or distortion. Correct zero-filling to properly define the shape, peak phasing, baseline correction, and suitable data acquisition parameters are key features in obtaining proper integrals. Due to incomplete baseline separation of the glycine and glutathione peaks, peak fitting, or deconvolution, was used to obtain peak areas in this study (45). Figure 6b shows plots of peak area ratios of glycine-to-dioxane and glutathione-to-dioxane after conversion ^{13}C fractional enrichment.

Single Component Curve Fitting

The in vivo ^{13}C peak intensities obtained as a function of time are fit to the appropriate rate equations to solve for kinetic rate constants using standard mathematical-based software programs, such as, Excel™, Mathematica™, and Matlab™. First, one creates a metabolic model for the biological system. This is done by compartmental analysis whereby the external and internal boundaries of the system are defined. Compartmental analysis is a routine data analysis methodology used in biomedical engineering (95) pharmacokinetics and many other disciplines. Using the example of 2- ^{13}C -glycine infusion in rats, we first defined the compartments in Fig. 6a (45, 92). This describes a very simple model in which constant glycine infusion into the central compartment (the blood) is relatively rapid for glycine (~60 min) and is defined by the volume of distribution. The volume of distribution is a pharmacokinetic term described as the volume by which the infused glycine will equilibrate and fill the various compartmental of a biosystem. Essentially, this is the time needed for the central compartment (blood) to reach steady state concentrations with all the organs of the body. It takes some time to fill these compartment(s) and that is defined by the glycine time course shown in Fig. 6b with a half-life of 24 min. It takes five half-lives to reach steady state (45). Once inside the hepatocytes, glycine is metabolized by cytosolic glutathione synthetase to yield the tripeptide glutathione. Glutathione is an antioxidant needed to protect the cell. It has a relatively long half-life (i.e., turnover in order of tens of hours). After being made in the cytosol, glutathione is transported into the mitochondria. Since import into mitochondria is rapid compared to glutathione synthesis in the cytosol, its mitochondrial glutathione was not detected in the time course from the in vivo ^{13}C NMRS (45). Another potential reason mitochondrial

glutathione was not detected is that it became NMR-invisible upon import. In the mitochondria, glutathione may noncovalently bind to macromolecules, rendering it NMR-invisible. From the results, we are unable to exclude this possibility (see below) (45). Figure 6b shows the time courses of glycine (top) and glutathione (bottom) from which the kinetic parameter, half-life, was derived. Both glycine and glutathione were fit using a least squares algorithm to the one-compartment model (i.e., monoexponential) to derive the rate constant (k) according to:

$$y = A(1 - e^{-kx}) \quad (8)$$

Since glutathione did not reach a similar fractional enrichment as glycine, it is obvious that the reactions have not reached steady state. The fact that glycine isotopic equilibration was not at steady state until 60 min after start of infusion would affect the kinetic analysis of glutathione if the kinetics were on similar time scales and (8) would need to be modified to subtract the glycine curve representing volume of distribution phase. However, because the half-life of glycine was 24 min and that of glutathione was 1.6 h, it was possible to neglect the rapid glycine exponential when deriving the glutathione kinetic equations. Another potential problem in determining accurate turnover rates is the time course of the observations. Ideally, one should acquire data for five half-lives to obtain the most accurate measure of kinetic parameters. However, this would have been 8 h and the rats could not tolerate 8 h with the surgery they had undergone (45). The physiological perturbation would have had more effects on accurate physiological glutathione kinetic determination than truncating the time course. This study was run for nearly three half-lives and this is sufficient to estimate the turnover rate. However, any time course followed for less than three half-lives should have some proportional error associated with the rate derivation. However, a single exponential can be rather well determined by a small number of very precise measurements.

Although the infused 2- ^{13}C -glycine was fit with a one-compartment model, in fact, there is a second component to the curve, and the curve is composed of two rate constants of vastly different rate time scales. The first occurs within 2 h as discussed above—the time it takes glycine to distribute throughout the body to fill the volume of distribution. This extremely fast rate was not detected with this 10 min temporal resolution, the uptake of glycine from the blood to the hepatocytes. The second component takes 3 days to reach equilibrium and is the protein pool becoming labeled and is the reason only 80% of glycine is labeled after 4 h of infusion (25). Therefore, as long as rates are resolved with sufficient temporal resolution so that the peak fitting algorithms can separate out the various resonances, multiple rates can be determined from a single dynamic ^{13}C NMR time course. In short, glycine kinetics reflect the volume of distribution plus whole body protein turnover, whereas the glutathione label represents de novo synthesis.

In the time course (Fig. 6b), the y -axis represents the absolute fractional enrichment rather than relative fractional enrichment. To obtain absolute fractional enrichment, a tissue extract of metabolites was made using the previously described perchloric acid extraction method and a high-resolution NMR spectra was obtained and metabolite concentrations were determined. The *in vivo* time point was calibrated to this value. Figure 6c is a high-resolution ^1H NMR spectrum of the tissue extract. The extract was treated with bromobimane, which reacts with free sulfhydryl groups including that of the reduced form of glutathione. Last, the extract was passed over a C18 cartridge to eliminate coresonating biochemicals within the liver extract. The $[2\text{-}^{13}\text{Cglycyl}]$ glutathione satellite peak areas in the ^1H -spectra in Fig. 6c are represented by the $[2\text{-}^{13}\text{Cglycyl}]$ glutathione peak areas plus $[2\text{-}^{12}\text{Cglycyl}]$ glutathione peak area. These peak areas are summed up to determine the fractional enrichment. This method of fractional enrichment determination is considered the “gold standard” in NMRS (20, 21, 51, 52). The fractional enrichment obtained at the end of the experiment is then assigned to the peak area ratio of the final *in vivo* time point and the previous peak area ratios are calibrated to this value to generate the graphs shown in Fig. 6b.

There are several other factors that must be considered that could affect the accurate measurement of turnover rate. In addition to exchange kinetics vs. *de novo* synthesis that can affect the turnover rate of metabolites (96), factors such as differential saturation of peaks and NMR visibility may alter results as well. To correct for saturation effects (see Chap. 6), saturation factors should be determined (45). The visibility of a metabolite by NMR depends on its SNR and detection limit. Most metabolites interact with macromolecules (see Fig. 1), e.g., the metabolic enzymes, membranes, and polynucleotides, so this is a common recurring problem in metabolite analysis. The bound fraction metabolites are typically broadened (and may also be shifted along the x -axis, or chemical shift represented by δ) below the detection limits. Owing to the slow tumbling rate of the protein, R_2 is shortened and peaks broaden (see Chap. 6). NMR detects predominantly the free metabolites. Thus, the total concentration can in some instances be substantially larger than what is actually observed by NMR, and the bound fraction varies from metabolite to metabolite. This raises the issue of how to deal with metabolic fluxes at all if most is bound and NMR-invisible. A classic example of this was the controversy over glycogen (97, 98) ATP (99, 100) and polyamine (101). One solution is to cast all of the appropriate equations in terms of free concentrations when analyzing NMR datasets, rather than total concentrations. However, *in vivo* NMR visibility should always be determined when possible.

NMR visibility is typically determined by comparing peak area ratio *in vivo* to the same peak ratios in the extract. Obviously, it is

important to know the NMR visibility of one of these metabolites represented by the peak ratio in order to obtain an accurate measure of the peak of interest. Glutathione, for example, binds to the protein compartment in cells creating a mixed disulfide pool (bound fraction) or coordinates with iron or other macromolecules, which broadens the *in vivo* NMR peak to the point of becoming invisible (see Chap. 6) (45). Macromolecular binding or chelation with paramagnetic ions resulting in NMR invisibility can often be misinterpreted as being a normal condition of the biosystem. However, it could be the nonphysiological conditions of the biosystem causing the protein binding. For example, glutathione rapidly forms mixed-disulfides when cells experience stress conditions. In an early study, Nicholson et al. (102) concluded that glutathione was not ^1H NMR-visible due to protein binding in packed hepatocyte suspensions-administered acetaminophen. In fact, they were likely correct and the glutathione was bound, but this was due to the highly hypoxic environments of the packed hepatocytes, which release iron from ferritin pools and ultimately increase the bound fraction and cell death. Later, in perfused MCF-7 cells (103) and intact liver (45), glutathione was ^{13}C NMR-visible. Even the superior R_2 values of ^{13}C (e.g., roughly the width in Hz at half peak height in the spectrum shown in the top spectrum in Fig. 5) compared to ^1H nuclei could account for this lack of NMR visibility. Therefore, it is very important to investigate the physiological relevance of the biosystem before blaming NMR visibility. At the back-end of the *in vivo* NMR experiment, the extraction procedure is very important and can lead to macromolecular binding and loss of micromolecules/metabolites (see Chap. 2). In fact, perchloric acid extraction generates peroxy radicals from the heavy iron load and increases the bound fraction of glutathione. This made the results from the experiment shown in Fig. 5 to be noninterpretable regarding glutathione NMR-visibility (45).

This effect of line broadening or shortening R_2 values is best illustrated with the endogenous chelator, citrate, and binding to divalent cations such as manganese. In fact, these cations are often added to extracts to shorten R_1 values, so spectra can be obtained more rapidly (104). Depending on the binding constant, the binding of cations can affect the chemical shift, and this phenomenon has been used to determine intracellular magnesium and calcium ions concentrations using endogenous and exogenous chelators such as ATP and FBAPTA, respectively (41, 105). The use of chelators and their relaxation mechanism are used as contrast agents in MRI. Desferrioxime, sold as DesferalTM, is used to bind endogenous iron and secreted into the biliary tree from the liver and is an imaging contrast agent, decreasing R_1 values (106). For a physical description of mechanisms of relaxation, the reader is referred to Chap. 6.

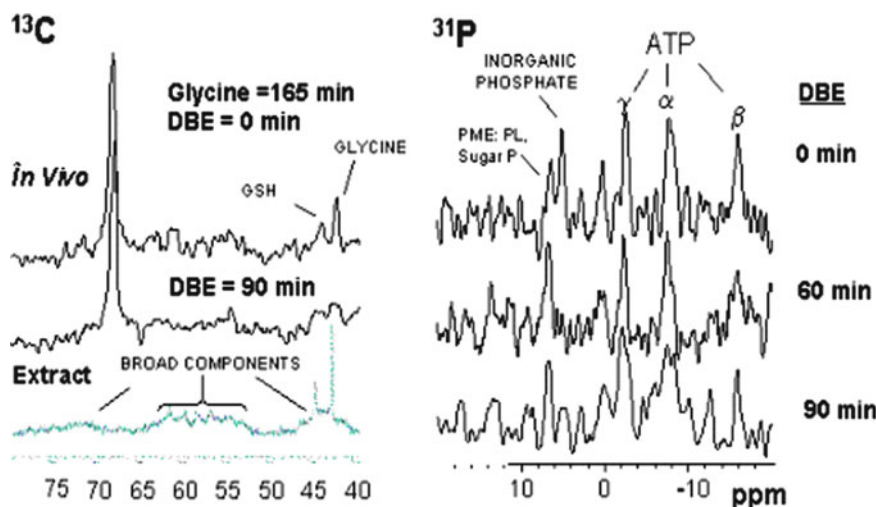


Fig. 7. The time course of in vivo ^{13}C and ^{31}P NMR spectra of liver from intact rats infused with 2- ^{13}C -glycine. The glycine was infused for 165 min and followed by administration of half the LD_{50} dose of dibromoethane. Note very little change to the ^{31}P spectra, yet significant changes in the ^{13}C spectra. Adapted from ref. (92).

Finally, there is always the potential of unanticipated physiological perturbation during in vivo experiments as a result of the continual fight for improved NMR spectral quality at the cost of maintaining normal physiology. Often in the process of setting up a biological NMR experiment, experimental parameters may skew results. Parameters affected include hypoxia (e.g., decreasing perfusion of organs, or increasing anesthesia to animals to decrease motion effects), or increase in stress hormones such as adrenalin or IL-6 (e.g., surgical implantation of the NMR surface probe to increase sensitivity). These perturbations will cause rate changes to compensate for the stress and binding effects—both of which will taint in vivo fluxomics data.

3.2. Nonsteady State, Dynamic Measurements from In Vivo ^{13}C NMR Spectral Time Course Data

An example of nonsteady state, dynamic measurement of flux by in vivo ^{13}C NMRS is the administration of dibromoethane during glycine infusion using the same rat model as previously described (45), except 1.1 mM/kg/h infusion was used instead 4.4 mM/kg/h (92), thus the smaller glycine and serine peak areas. Figure 7 shows the results from interleaved in vivo $^{31}\text{P}/^{13}\text{C}$ NMRS, a method first described by experiments by Cohen (76) using perfused liver. After 165 min intravenous infusion of 1.1 mM/kg/h of 2- ^{13}C -glycine (^{13}C = 0 min, left; ^{31}P = 0 min, right), a LD_{50} of the carcinogen dibromoethane dissolved in corn oil was administered by intraperitoneal injection and serial 10 min acquisition $^{31}\text{P}/^{13}\text{C}$ spectra were obtained during the first 90 min postinjection. While the spectra are very noisy, it is clear that there was little change in the inorganic phosphate and ATP peaks in the ^{31}P spectra, while there is a greater change in the ^{13}C spectrum.

The defined glycine and glutathione peaks redistribute to unknown broad peaks in the ^{13}C spectrum of the perchloric acid extract of the liver taken at the end of the experiment (time = 90 min postinjection or 255 min post $2\text{-}^{13}\text{C}$ -glycine infusion), which were never observed in similar extracts obtained after the same time of $2\text{-}^{13}\text{C}$ -glycine infusion (Fig. 5c). Clearly multiple concentrations, and thereby fluxes, are changing with time, but the only concentration that was identified was inorganic phosphate and ATP from the ^{31}P spectra. In order to obtain concentrations and thereby interpret the $2\text{-}^{13}\text{C}$ NMR spectral time course in order to derive fluxes, not only significantly better SNRs are required, but also the in vivo ^1H NMR spectra in order to obtain relative concentrations. To our knowledge, this has never been performed by in vivo NMRS. As mentioned in the previous section (Sect. 3.3.1), rat liver is overloaded with iron resulting in very few resolved peaks by in vivo ^1H NMRS, and these first studies would be the most feasible in brain, which delivers some of the spectral quality of any tissue.

3.3. Steady State, Static Measurement of Isotopomer Ratios and Compartmentation

Isotopomers are identical molecules with ^{13}C in different locations. In some metabolic pathways, a single carbon label in a substrate can be incorporated into multiple positions of a downstream metabolite depending on enzymes. Examples showing how such isotopomers can be generated are described in a previous chapter (see Chap. 6) and in Sect. 2.1.1. ^{13}C NMRS has the advantage over other analytical methods, such as mass spectrometry, in analyzing isotopomers because positional information is inherently present in the NMR spectra, and the ^{13}C - ^{13}C coupling patterns resolve the various isotopomers. Although MS/MS and analysis of fragmentation patterns can also obtain positional isotope information (see Chap. 4), it is destructive and is not “non-invasive”—the topic of this chapter. The best example of how isotopic scrambling can occur involves the production of succinate in the Krebs’ cycle (Fig. 2). Isotopomer analysis can be used to determine the Krebs’ flux and anaplerosis by analyzing the glutamate molecule and location of ^{13}C labels (54, 107).

3.3.1. Quantifying Tissue Compartmentation from ^{13}C NMR Spectra

In conjunction with isotopomer analysis, NMR can determine metabolic compartmentalization not only noninvasively in vivo, but the positional isotopomers obtained directly by a single 1D or 2D high-resolution NMR spectrum from tissue extracts (see Chap. 2). The data can be confirmed by MS/MS analysis (see Chap. 4). Metabolism in glia and neurons is encoded with isotopomer information, precluding the need for microdissection of these tissues. These isotopomers contain a “memory” of the metabolic processes or relative fluxes occurring in the various compartments. Compartmentation of neurotransmitters in the various type of cell of the brain is extremely important for proper functioning of the central nervous system;

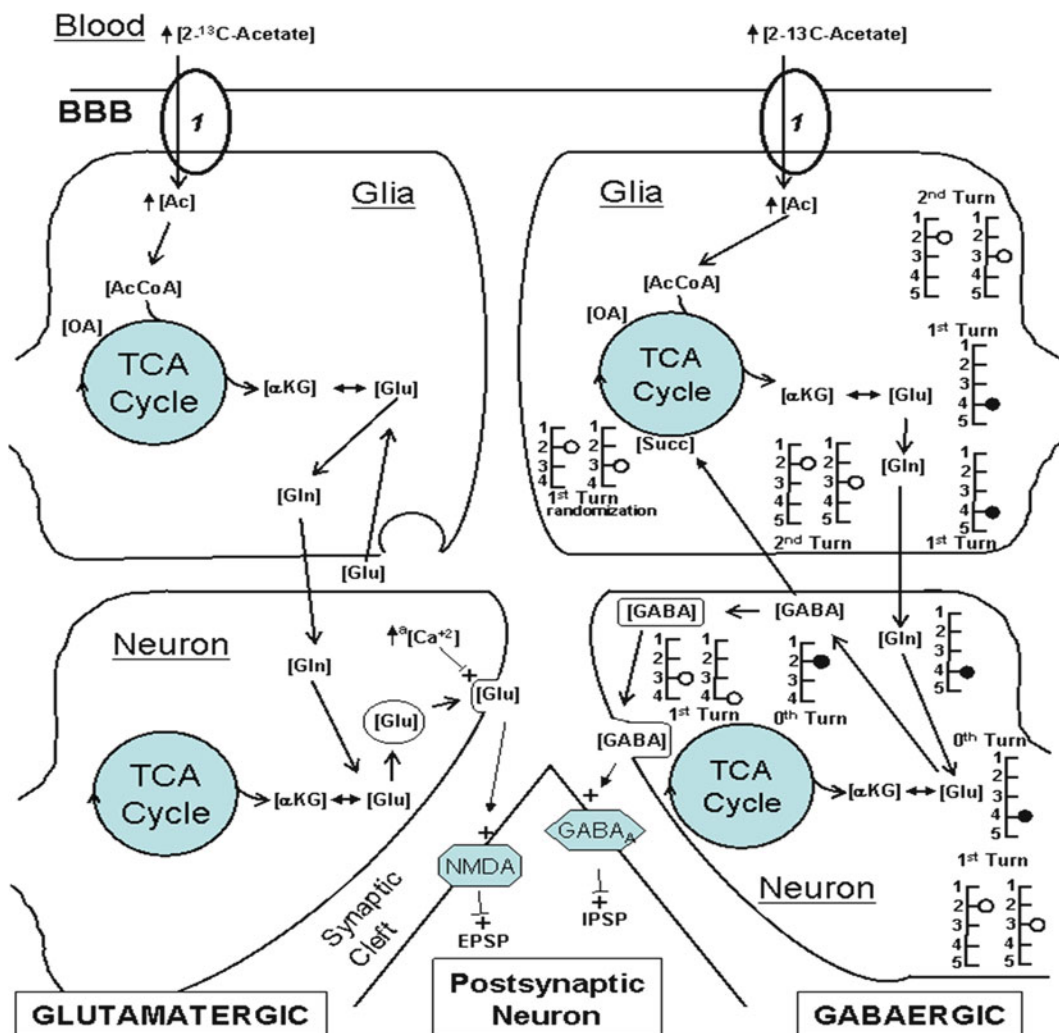


Fig. 8. The compartmentation of $2\text{-}^{13}\text{C}$ -acetate metabolism in brain. Isotopomeric analysis of the glutamine, glutamate, and GABA was used to determine the relative metabolic control between the glutamergic and GABAergic neurons. The various isotopomers are given as stick diagram on the right side. BBB blood-brain barrier; NMDA *N*-methylaspartate receptor; GABA gamma-butyric acid; EPSP excitatory postsynaptic; IPSP inhibitory postsynaptic; OA oxaloacetate; $\alpha\text{-KG}$ α -ketoglutarate; *Gln* glutamine; *Glu* glutamate; *Ac* acetate.

isotopomer analysis has been extensively used to quantify kinetics and compartmentation (108, 109). The best example of this is the use of glutamine/glutamate cycling in the brain using $2\text{-}^{13}\text{C}$ -acetate (110–112). Figure 8 is a diagram of the tissue compartmentation of acetate metabolism in the brain, demonstrating the use of in vivo ^{13}C NMR to map metabolism. The key to quantifying Krebs' flux is the molecular randomization of the ^{13}C -label at the formation of the symmetrical molecule, succinate (Fig. 8). Succinate is a symmetrical compound and the carbons at the 2 and 3 positions are chemically equivalent. If $2\text{-}^{13}\text{C}$ -acetate is metabolized by astrocytes, then

α -ketoglutarate is labeled at the three position; there is an equal chance of this label being incorporated into the two and three positions of succinate (Fig. 8). That is, what should become the C3 of succinate due to symmetry is the same as the C2 of succinate. As the four-carbon molecule continues through the Krebs' cycle, it becomes nonsymmetric at malate forming 1:1 ratio of 2- ^{13}C -oxaloacetate to 3- ^{13}C -oxaloacetate on the first turn of the Krebs' cycle (Fig. 8). On the second turn of the Krebs' cycle, α -ketoglutarate is equally labeled at the two and three positions (Fig. 8).

The key to determining metabolic compartmentation in the brain is the fact that 2- ^{13}C -acetate is metabolized to glutamine only in glial cells, and then the glutamine is transported to the neuron (Fig. 8). Once inside the neuron, the glutamine is metabolized to glutamate and incorporated into vesicles, which in turn are secreted into the synaptic cleft once activated. In addition to glutamatergic neurons, GABAergic neurons also form GABA from astrocytic formation of glutamine. Any difference in relative abundance of the isotopomers dynamically or at steady state is due to metabolic processes in the different compartments, and therefore one can elucidate on metabolic demand and control by comparing the isotopomers between glutamine, glutamate, and GABA. That is, by using the metabolic "trick" of the scrambling of the succinate labeling and the metabolic memory encoded by the isotopomers of these three biochemical, not only can the Krebs' flux be determined in glia (i.e., astrocytes) and neurons, but so can the relative uses and demand for the glutamine substrate for neurochemical activity. For example, if the C2-to-C3 isotope ratio of glutamine differs from glutamate or GABA, then one can make conclusions regarding regulation of metabolic coupling between these two tissue types under different conditions (113). Hassel et al. showed that in the steady state, the C3/C4 ratio in glutamine and glutamate (and the corresponding C3/C2 ratio in GABA) gives an indication of the fraction of carbon skeletons that exit the Krebs' cycle on each turn (113). Further, they state that the comparison of this ratio in GABA (C3/C2) to that in glutamate and glutamine (C3/C4) allows an assessment of the fraction of GABA derived from glutamine carbon skeletons vs. skeletons from the glutamate pool that have traversed the neuronal Krebs' cycle.

3.3.2. Quantifying Cellular Compartmentation from ^{13}C NMR Spectra

Figure 9 is a schematic representation of the two different compartments of the cell where the various serine isotopomers are formed, the cytosol and the mitochondria. To the right is a portion of a representative ^{13}C NMR spectrum of PCA extract of rat infused for 3 h with 2- ^{13}C -glycine, demonstrating the various peaks corresponding to the three isotopomers. The methyl donor depends on substrate (114), but glycine is a major methyl donor in the mammalian mitochondria (115). The cytosolic methylating

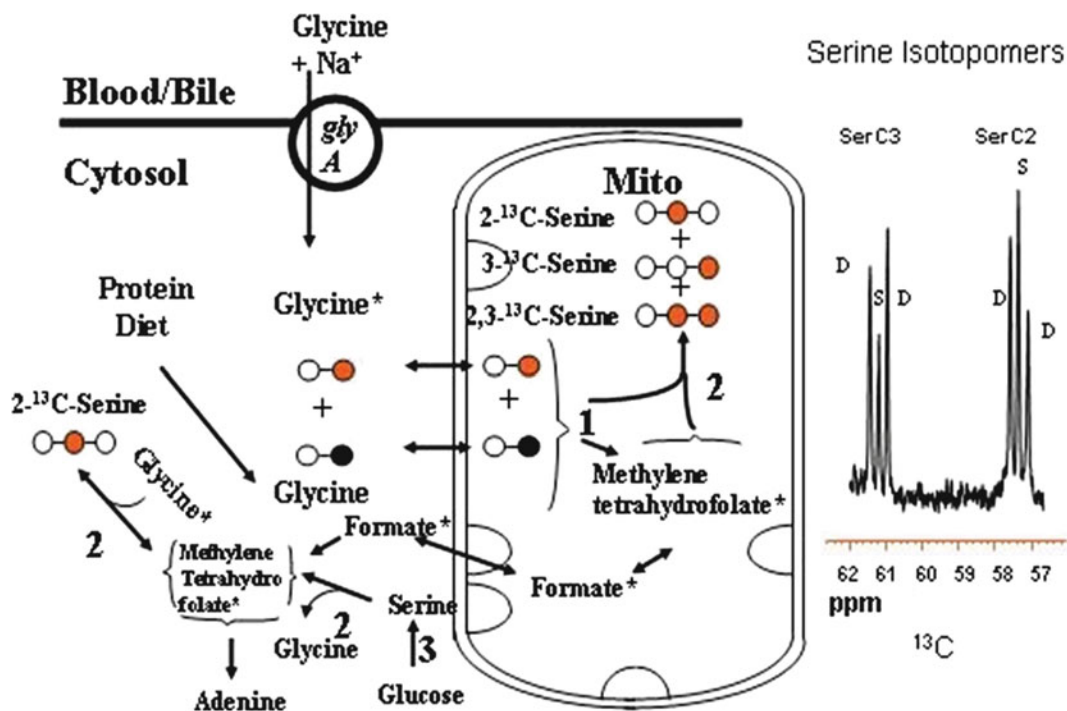


Fig. 9. Compartmentation of serine synthesis and the use of isotopomeric analysis and ^{13}C MRS to determine compartmentation biochemistry and monitor mitochondrial function.

agent, *S*-adenosylmethionine, was unlabeled in this study of anesthetized Sprague-Dawley rat (92), therefore the peak pattern at the C2 and C3 of serine should be the same; however, the singlet C2 peak representing $2\text{-}^{13}\text{C-serine}$ isotopomer is larger than the singlet C3 peak, representing the $3\text{-}^{13}\text{C-serine}$ isotopomer. The additional C2 singlet represents 20% of the total serine C2 and C3 peak area, and therefore 20 and 80% was formed in the cytosol and mitochondria, respectively (92).

Specifically, the mitochondrial matrix and the cytosol require exchange of metabolites across two mitochondrial membranes: inner and the outer. The difference in glycine metabolism in mitochondria and cytosol provides the approach to quantitatively monitor the activity of these pathways in hepatocytes from profiling of individual serine isotopomers in cellular extracts. Mitochondrial compartment contains four enzymes of the so-called Glycine Cleavage System (GCS). Four reactions facilitate decarboxylation and deamination glycine resulting in generation and transfer of CH_2 group of glycine to *TetraHydroxyFolate* (THF), a cofactor of mitochondrial Serine *HydroxyMethyl Transferase* (*mSHMT*), thus forming methylene-THF (Fig. 10). At next step, this methyl group from $\text{CH}_2\text{-THF}$ transferred on another molecule of glycine,

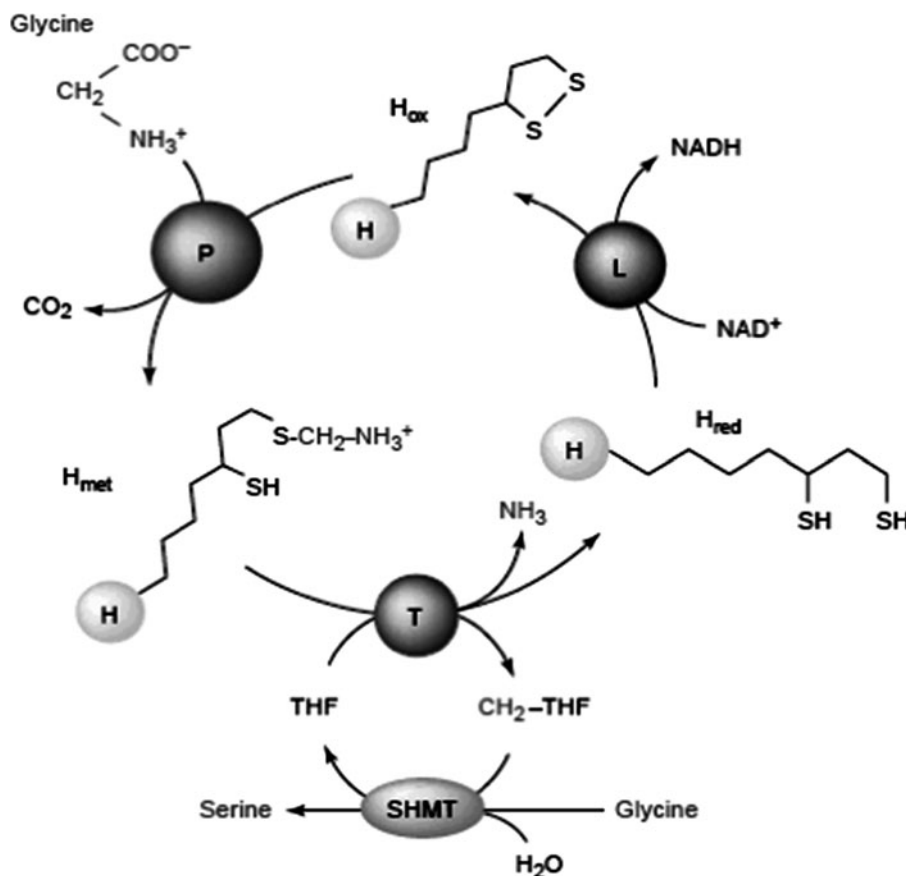


Fig. 10. Glycine cleavage system of mitochondria. P-glycine decarboxylase, T-deaminase, L-reductase, *SHMT* Serine Hydroxymethyl Transferase; *THF* TetraHydroxyFolate, $\text{CH}_2\text{-THF}$ -methylated THF, H-pyridoxal phosphate: H_{red} , H_{ox} , and H_{met} oxidized, reduced, and methylated forms, respectively.

thus forming the molecule of serine (Fig. 10). This reaction is highly irreversible and this determines unidirectional flow of substrates in mitochondrial GCS from glycine to serine. The carbon atom of methyl group derived from glycine molecule comes from β -position (2C) and incorporated into serine as γ -carbon (3C). The absence of such system in the cytosol results in synthesis of different serine isotopomers by cytosolic SHMT from methyl groups generated using the sources different from glycine (115).

3.4. Multiple Pathway Analysis for Fluxomics

There are a few in vivo ^{13}C NMR studies measuring multiple metabolic fluxes. Jones et al. elegantly demonstrate the feasibility of relating glucose and glutamate ^{13}C -NMR multiplets to corresponding metabolic pathways of gluconeogenesis and pyruvate recycling (116). The study focuses on glucose and glutamate for several reasons with the main goals centering on human applications. Noninvasive collection of urine from human subjects is

clinically advantageous and preferred over blood tissue biopsy by patients. The logic behind choosing uniformly $[1,2,3-^{13}\text{C}_3]$ labeled propionate as a tracer as opposed to a single-labeled carbon is that it manifests multiplets for glucose and glutamate as opposed to singlets, resulting in additional biochemical information; also, utilizing propionate simplified quantification because it enters the Krebs cycle via a single irreversible anaplerotic pathway as opposed to multiple entries for other substrates like alanine or lactate.

The observed isotopomers derived from $[1,2,3-^{13}\text{C}_3]$ propionate of glucose and glutamate combined with simple mathematical equations of the metabolic model involved was the strategy for obtaining fluxes in this work. A comparison between isolated perfused livers and livers from intact animals showed little difference in the rates (116). Accordingly, gluconeogenesis and pyruvate recycling is easily and reliably measured in a ^{13}C spectrum of blood after an oral dose of $[1,2,3-^{13}\text{C}_3]$ propionate, without unknown metabolites crowding the multiplets.

4. In Vivo NMR Experimental Considerations

Some tissues have innate biological characteristics resulting in superior NMR spectra (i.e., sharper peaks resulting in better resolution and SNR) as compared to others. It is for this reason that the majority of in vivo multinuclear NMR studies have been on brain and the fewest on internal organs, particularly liver, kidney, spleen, lungs, and intestine, even though the very first ^{13}C NMR studies were on liver (117). Poor NMR spectral quality of these organs is due to high ferromagnetic load, motion, or having air–water interface. To reduce the problem of motion and iron in the blood and enhance sensitivity by the use of higher field magnets with superior NMR probes, the majority of NMR studies on internal organs have used excised tissues that can be perfused in a high-resolution NMR spectrometer (117).

4.1. Animal Handling and NMR Hardware

Animals can be anesthetized with pentobarbital or some other general anesthetic, but a volatile anesthetic such as 3% isoflurane/nitrous oxide/oxygen and maintained with about 2% isoflurane/oxygen is preferred. Anesthetics, especially general anesthetics, decrease body temperature and animals must be placed on a heating pad to maintain body temperature during the NMR experiment. Animals typically undergo a survival surgical procedure to implant a catheter into the jugular, femoral, or tail vein through which stable-isotope-labeled amino acids can be infused. Although the label can be administered via intraperitoneal injection or gavage, the kinetics is nonsteady state and complex. The animals are anesthetized during the cannulation procedure and kept warm on a warming pad.

The chronic jugular vein cannulation procedure (118) is the most effective and common. An incision across the right side of the neck will reveal the right jugular vein which will be cannulated with polyurethane tubing. The catheter is subcutaneously routed to the back and exteriorized between the shoulder blades. The animal is fitted with a jacket/harness to hold the infusion line in place. The surgical procedure takes a trained surgeon about 20 min to complete. The catheterized animal wakes up from the anesthesia and can be free to move about its cage as the infusion line is attached to a swing arm allowing unhindered mobility. The animal recovers for a day to make sure the surgery does not affect metabolism, as alpha and beta adrenergic hormones (fight or flight hormones) are released during surgery and corticosteroid during the healing process. Once healed, the infusion line is used to deliver stable-isotope-labeled amino acids for periods up to 24 h or more.

4.2. Hardware

Besides the NMR console and magnet, the hardware for in vivo ^{13}C NMRS consists of the NMR probe and the perfusion loop for excised liver and animal infusion and monitoring system for intact animals. High-resolution probes cost in the range of \$20,000–50,000, whereas in vivo surface coils range from \$5,000 to \$10,000 and can be easily constructed with minimal experience beyond a novice education in radiofrequency engineering (119). For animal studies, knowledge of building one's own NMR probe construction is essential due to the fact that one may need to change coil geometries based on the region of interest. Perfused organ studies use a volume coil wherein the entire liver is contained within the NMR coil, and the NMR probe is designed for vertical bore magnets. For animals, typically surface coils are used to localize to the tissue of interest, and typically the NMR probe is designed for a horizontal bore magnet for rats or larger. A drawing of a perfused liver in a volume coil is shown in Fig. 11a with the various components of the perfusion loop (76). It is very important to place a bubble trap just before the media line enters the bore of the vertical bore magnet from the top. Bubbles can get trapped inside the liver and destroy spectral quality due to enormous magnetic susceptibility effects caused by the air–water interface. A picture of a surface coil used for rat studies is drawn in Fig. 11b. The surface coil is localized to liver by implanting or placing it on the right side of the rat over liver (45). Implantation of surface coils was first reported in 1986 (120), and many sophisticated surface coils such as phase-arrays (121, 122), as well as RF coils for microscopy (123) have since been developed. The reader is directed to reviews for in-depth description of RF coil design, theory, and construction (123, 124).

For the direct detection of ^{13}C , various NMR radiofrequency (RF) NMR probes designs have been used for receiving ^{13}C signal and decoupling the ^1H signal $\#$: (1) two dual surface coils

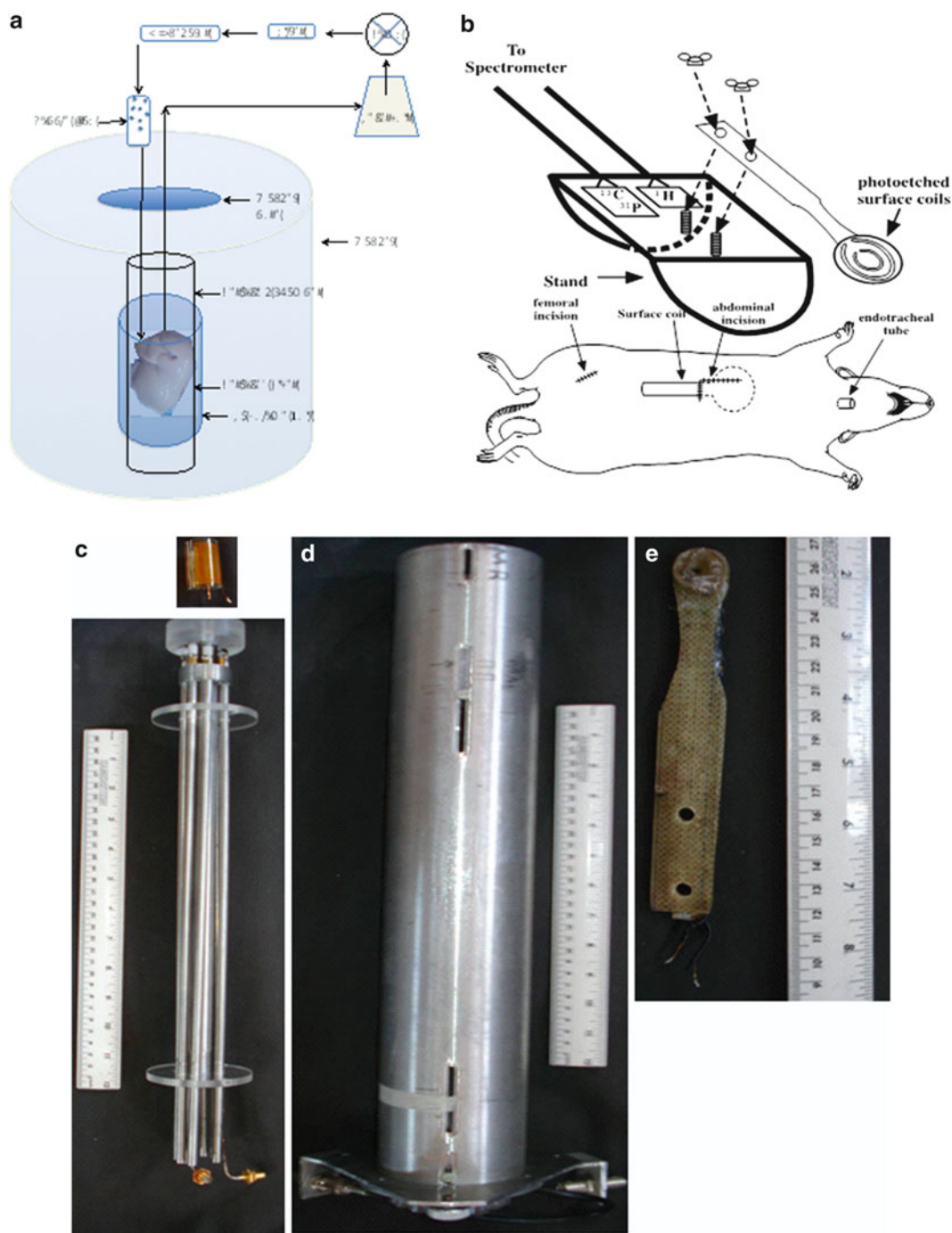


Fig. 11. NMR probes. Examples of the volume (a, c), and surface (b, e) NMR probes. The housing (d) is necessary to shield from RF noise. Schematic (b) was modified from ref. (45), from Macdonald.

in-plane (45) or orthogonal to one another (125), (2) surface coil receive/volume coil decouple designs have been used (85), or (3) two volume coils can be used (125). An implanted coil was used in the experiments shown in Figs. 5–7, which consists of an outer loop tuned to the ^1H frequency, and twice the diameter as the inner loop tuned to the ^{13}C frequency when placed on the same plane, or more typically placed orthogonally to the ^{13}C . The ^1H is used for decoupling in direct ^{13}C detection. This configuration is swapped for indirect detection of ^{13}C through ^1H . Difference pulse sequences are used for direct and indirect detection, as described below. As a rule of thumb, a hemispherical excitation profile is achieved defined by the function of a half circle, four-thirds pi multiplied by radius cubed ($4\pi r^3/3$), for sensitive volume (126). For example, a 6.5 cm diameter surface coil has a sensitive volume (i.e., the volume detected by the coil) of 70 cm^3 , but tissue is typically on just one side of the surface coil, so this would be half of this volume, or 35 cm^3 of tissue. The best way to empirically measure the proportion of tissue under the surface coil is to obtain a ^1H MRI and the limits of the image will define the sensitive volume (126). The sternum of the animal is placed on a nonmagnetic transducer to measure heart rate and placed on a water bath or heating pad for temperature control. An infusion line is typically used for chronic infusion of the ^{13}C -labeled substrate, and sometimes anesthesia. Preferably, volatile anesthesia is used. The rat and attached surface NMR probe, warm pad, anesthesia and infusion lines, and heart monitoring transducer are contained on a stand and the entire assembly is inserted into the magnet. As many as five lines can be extending from the magnet, including lines for volatile anesthesia, infusion, warm water, heart rate monitor, and NMR probe (45).

Many volume and surface NMR probe designs have been published, but consist of the same primary components. The various components of a NMR probe for vertical bore magnets are shown in Fig. 11c. The volume coil sits at the top of the probe and will be at the isocenter of the magnet during operation. Shown at the top of Fig. 11c is a photoetched Helmholtz coil. A broadband coil consists of an inner coil tuned to ^{13}C Larmor frequency and orthogonally placed to an outer coil tuned to ^1H Larmor frequency; an indirect coil configuration has this design in reverse. The implanted surface coil used in the in vivo ^{13}C NMR animal studies of 2- ^{13}C -glycine metabolism is shown in Fig. 11e. It consists of a photo-etched surface described in Fan and Higashi (127), which is attached to leads and glued to a fiberglass support coated with polyethylene spray to insulate the circuit. As mentioned above, long leads can cause spurious resonances and so twisting leads can eliminate any large loops that could create an undesired resonating inductor in the circuit. However, in this case, since the NMR surface coil was implanted, the leads needed to be long enough to attach to a circuit outside the animal. More recent studies do not

implant the surface and the length of the leads is minimized and localization is achieved using the gradients (125).

4.3. Statistical Analysis of Flux Data

Data obtained in flux experiments can undergo statistical analyses using standard techniques such as Student's *t*-test or ANOVA, depending on the experimental design. The simplest type of statistical problem is when only one experimental measure, such as metabolite concentration or its flux, is collected in a number of experiments under two different naturally occurring or experimentally induced conditions. In Table 1, the fluxes were minimal and Student's *t*-test was sufficient for use. However, as the datasets get large and multiple fluxes are compared, ANOVA and other multivariate statistical analyses will need to be applied.

5. Mathematical Models: Metabolic Flux Balance (MFA) and Metabolic Control Analysis (MCA)

5.1. Metabolic Flux Balance Analysis and Metabolic Control Analysis

Mathematical modeling and computational analysis in conjunction with experimental studies can enhance the understanding of metabolic systems greatly (128). Due to various experimental limitations in finding all the metabolic fluxes, to construct a fluxome of a complex metabolic system is very difficult if not impossible. Modeling biological data can be predictive given less, little, or no empirical data or, using empirical NMR-derived fluxomic data using known metabolic pathways is defined as “discrete” models. Using the stoichiometric properties of reactions involved, one can calculate unknown fluxes in metabolic systems, knowing a few of the fluxes by using experimental methods such as ^{13}C NMR. One can use metabolic flux balance analysis (FBA) for this purpose (129, 130). In FBA, one is interested in calculating the intracellular steady state fluxes using a stoichiometric model and applying mass balances around those fluxes. Steady state is assumed to occur in the time scales involved in such experiments, in most biological systems (131). Measured fluxes usually are the uptake rates of substrates and secretion rates of metabolites. MFA assumes reaction stoichiometry, but there is no need to know the kinetic properties of any enzymes involved. How these steady state fluxes and metabolite concentrations are influenced by enzyme properties or other parameters in the system can be understood using a mathematical technique called MCA (131, 132). MCA helps us to predict the metabolic effects of perturbations on the system and tells us how metabolic system properties are controlled and shared among different enzymes in the pathway. One important aspect of biochemical systems is that the control is distributed over the entire system.

5.2. Flux Balance Analysis

One can write the rate equations for metabolic concentrations using simple mass balance; the rate of change of a metabolite at a specific time is equal to the net difference of incoming fluxes and outgoing fluxes (131). Consider a metabolic network with m metabolites and r reactions. We can write the rate of change of the metabolite concentration as:

$$\frac{dx_i}{dt} = \sum_{j=1}^n S_{ij}v_j, \quad i = 1, \dots, m \quad \text{and} \quad j = 1, \dots, r \quad (9)$$

Here x_i is the concentration of the i th metabolite, S_{ij} is the ij th element of the stoichiometric matrix, and v_j is the flux through reaction j . In matrix form, we can write it as:

$$\frac{dx}{dt} = Sv \quad (10)$$

Here, the rate v is a function of metabolite concentrations x , kinetic parameters p , and time t : $v = v(x, p, t)$. v is in general a nonlinear function. At steady state, $dx/dt = 0$, and hence $Sv = 0$.

If we know a few steady state fluxes, we can write the above equation as a sum of two parts, containing the k known fluxes, v_k , and the u unknown fluxes v_u .

$$S_u v_u = -S_k v_k \equiv -b \quad (11)$$

Therefore, the unknown fluxes are given by: $v_u = -S_u^{-1}b$

When S_u is a square matrix and all the rows are linearly independent, one can calculate the inverse of S_u , S_u^{-1} . Using that one can easily calculate the unknown fluxes by Gaussian elimination.

However, in most of the real situations, S_u is not a square matrix and there will be linear dependencies between different rows. In general, number of reactions r will be more than the number of metabolites, m . Here are some of the different situations that can arise.

- When the rank of S_u is less than u , the system is underdetermined. In such cases, one can use constraints based on biological reasoning and try to find the unknown fluxes using linear optimization and other methods.
- When rank of S_u is equal to u , it is a determined system.
- When rank of $S_u < m$, we have a redundant system. In such cases, one can still use the above equation to find the unknown fluxes using the generalized inverse of S_u . Generalized inverse provides a least square solution to this overdetermined system. In such systems, some of the rows are linearly dependent and give rise to redundancies. These redundancies can be utilized to estimate errors in the flux values.
- When rank of $S_u = u = m$, S_u is a square matrix and one can use simple linear algebra, as mentioned above to find the unknown fluxes.

5.3. Metabolic Control Analysis

MCA deals with understanding the effects of changes in the parameters such as enzyme concentrations, temperature, pH, etc., on the metabolic system quantities such as flux or metabolite concentrations (131, 132). Basically, it deals with estimating the sensitivity of a metabolic network function to system parameters. Sensitivity of metabolic flux and concentrations on the enzyme activities or other parameters are characterized by control coefficients.

MCA was introduced to biochemical systems in the 1970s by Kacser and Burns (133) and Heinrich and Rapoport (134, 135). The theory of MCA is given in Chap. 9. Below is an example of MCA using results obtained using *in vivo* ^{13}C NMR spectral data.

5.4. Example of an MCA NMR Experiment

Jucker et al. (136) used MCA to calculate the distributed control of insulin-stimulated skeletal muscle glucose disposal in awake rats. Due to the limitations of NMR experiments, a top-down approach to MCA where the control is defined over a few metabolic components each consisting of a number of enzymes was used, instead of a bottom-up approach where all the individual components are separately measured. Control of glucose disposal was considered to be distributed between (1) glucose transport through insulin-stimulated GLUT-4 and phosphorylation via hexokinase; (2) glycogen synthesis consisting of phosphoglucomutase, UDP-glucose pyrophosphorylase, and glycogen synthesis enzymes; and (3) glycolysis consisting of numerous enzymes including phosphofructokinase and pyruvate kinase in skeletal muscle.

Using the summation theorem, connectivity theorem, and branch point theorem (132, 137) involving the fluxes of glycolysis, glycogen synthesis, and glucose disposal, and elasticity coefficients with respect to G-6-P concentrations, they calculated the three flux control coefficients. Most of the control of glucose disposal during hyperinsulinemia was determined to be at the glucose transport/phosphorylation step (0.55 ± 0.10) and the rest distributed between glycogen synthesis (0.30 ± 0.06) and glycolysis (0.15 ± 0.02).

For this calculation, three separate hyperinsulinemic infusion protocols were used:

1. Protocol 1: Euglycemic (~ 6 mM)-hyperinsulinemic (10 mU/kg/min)
2. Protocol 2: Hyperglycemic (~ 11 mM)-hyperinsulinemic (10 mU/kg/min) clamp with somatostatin
3. Protocol 3: Euglycemic (~ 6 mM)-hyperinsulinemic (10 mU/kg/min)-lipid/heparin clamp

In this study, $[1-^{13}\text{C}]$ glucose was administered in all these protocols for a 3-h period, during which its incorporation into $[1-^{13}\text{C}]$ -glycogen, $[3-^{13}\text{C}]$ -lactate, and $[3-^{13}\text{C}]$ -alanine was determined in the hindlimb of awake rats via ^{13}C -NMR. Glucose-6-phosphate was measured using *in vivo* ^{31}P -NMR. The three

different protocols differentially modulate both the fluxes and intramuscular glucose-6-phosphate (G-6-P) concentrations so that they could calculate the elasticities. Blood samples were taken at different time points to measure the plasma glucose and lactate concentrations. Glycogen synthesis rates were calculated using the individual time point glycogen concentrations. Using the label incorporation into lactate and alanine, the glycolytic flux was calculated. ADP, ATP, Mg^{2+} , pH, and Pi were measured using in vivo ^{31}P -NMR and were constant, in all the three protocols. Such a large number of measurements are essential because the system comprises several intersecting pathways. It is difficult to obtain accurate flux measurements under these conditions, especially with single time point analyses. Furthermore, the influence of branch points makes the MCA analysis more complex, though rigorous matrix approaches have been developed (see Chap. 9). A key to all MCA models is the assumptions of the summation theorem. In many cases, where multiple experimental treatments are applied, this is false and calculated fluxes may be incorrect. Nevertheless, the study indicates that glycolysis itself contributes little control over the utilization of glucose under insulin stimulation.

5.5. Software for the Analysis of Metabolic Systems

There are several software packages available to do metabolic FBA and MCA. Many of them have both the capabilities and can be used to model and to simulate biochemical systems also. Here we mention a few of them, which are free for academic use.

1. FluxAnalyzer (<http://www.mpi-magdeburg.mpg.de/projects/fluxanalyzer>) (138): FluxAnalyzer is a Matlab package for integrated pathway and flux analysis with graphical user interface. This can be used for different types of stoichiometric network analysis including FBA.
2. MetaFluxNet (<http://mbel.kaist.ac.kr/mfn>) (9): MetaFluxNet is a software package for quantitatively and interactively analyzing metabolic fluxes.
3. COPASI (<http://www.copasi.org>) (139): COPASI is a software application for simulation and analysis of biochemical networks. Functionality of COPASI includes MFA and MCA along with several other biochemical modeling and analysis tools, with a graphical user interface.

6. Novel Technology for Fluxomics: Dynamic Nuclear Polarization

It is well known that ^{13}C NMRS (as well as other nuclei) has been limited in its ability to characterize metabolic states due to its low sensitivity. This low sensitivity is a result of the low natural

abundance of ^{13}C (1.1%) in addition to the low gyromagnetic ratio of carbon (6.728284×10^7 rad/T s). These characteristics reduce the overall sensitivity of ^{13}C nearly four orders of magnitude in comparison to ^1H NMR (6,400 fold without NOE or INEPT, 1,600 fold if include INEPT—cf. Chap. 6) and even more impressively for ^{15}N (up to 270,000 fold). Traditionally, the low nuclear polarization and low abundance were compensated by high concentrations of sample as well as the introduction of ^{13}C -enriched substrates. Depending on the nucleus, these direct detection methods require hours to days to record spectra with sufficient signal-to-noise for analysis.

With this difficulty in mind, a number of techniques have been proposed to increase the polarization of nuclear spins to overcome their low gyromagnetic ratios. In addition to enrichment, indirect detection methods have been widely practiced, but these require a convenient scalar coupled proton (cf. Chap. 6). Newer methods that provide a much greater sensitivity enhancement have recently been developed. These methods of hyperpolarization include: *para*-hydrogen-induced polarization (PHIP) (140), optical pumping (141), and DNP (142, 143). Each of these methods has the potential to generate 100% nonthermal polarization of the chosen $\frac{1}{2}$ spin nucleus. PHIP, also known as PASADENA (144, 145) and ALTADENA (146), relies on the introduction of a *para*-hydrogen substrate through catalytic hydrogenation (146). Though this method has been shown to be successful (147), it is only applicable to reactions involving substrates with double and triple bonds. Optical pumping utilizes circularly polarized laser light and has been successfully applied to the hyperpolarization of ^3He and ^{129}Xe (141). This method is restricted to a subset of the noble gases and has limited application to the study of metabolism. The final method, DNP, is based on the polarization of nuclear spins in an amorphous solid state at ~ 1 K through coupling of the nuclear spins and unpaired electrons via an organic-free radical. Recent advances in the field of low temperature physics, electronic paramagnetic resonance (EPR), and NMR have provided for the adaptation of the DNP technique, described as early as the 1950s (148), to metabolically appreciable systems (149–151). Due to its applicability, the purpose of this section is to describe this emerging technique of hyperpolarization and its application to the investigation of metabolic systems.

6.1. DNP Physics: The Solid State Effect and Hyperpolarization

Conceptually, what we consider DNP is an extension of what has been previously described as the “solid state effect” (148). In the early 1950s, Overhauser postulated that an NMR signal could be increased as a result of the interaction between a nucleus and the electrons of a metal (152). This principle was later applied to nonmetals by Abragam (153), and in 1974 (154), demonstrated

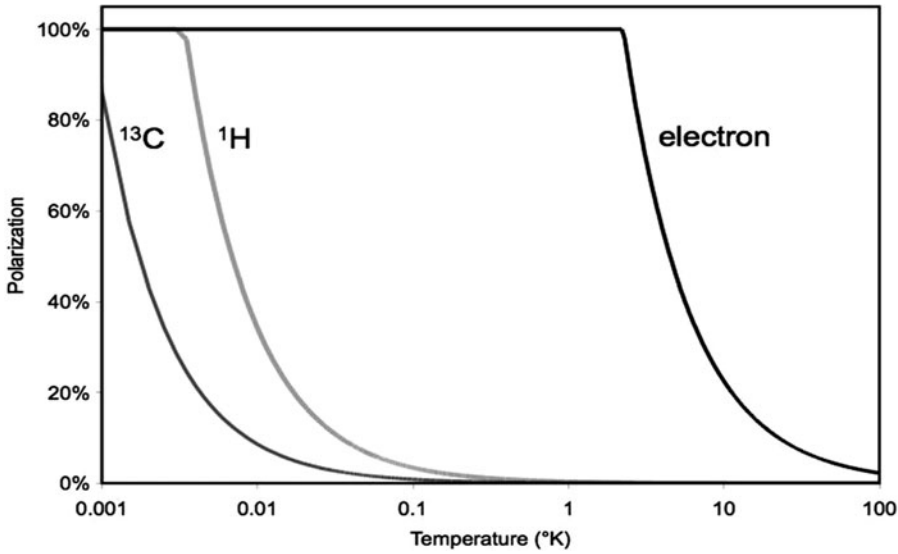


Fig. 12. Fraction polarization for different spins. Plot of the percent polarization as a function of time for each indicated spin. These were calculated using (12) at a magnetic field strength of 3.35 T.

that through thermal contact between nuclear and electronic spins, DNP can be produced (154).

To investigate the underlying physics of the solid state effect, first consider a set of nuclear spins I embedded in a solid containing a small percentage of paramagnetic impurities with spins S . These spins are of $\frac{1}{2}$ and have Larmor frequencies ω_I and ω_S . For a given spin, the spin density where all magnetization is along the z -axis corresponds to the equilibrium among states governed by the Boltzmann distribution. A spin $I = \frac{1}{2}$ can be characterized by two states $|\alpha\rangle$ and $|\beta\rangle$. The probability of finding a spin in each of the states is then proportional to (12):

$$P_\alpha \propto e^{(-E_\alpha/kT)} \approx 1 - \frac{E_\alpha}{kT}, \quad E_\alpha = \frac{-\hbar\gamma_I B_0}{2} \quad (12a)$$

$$P_\beta \propto e^{(-E_\beta/kT)} \approx 1 - \frac{E_\beta}{kT}, \quad E_\beta = \frac{\hbar\gamma_I B_0}{2} \quad (12b)$$

The overall spin polarization of this system is the population difference between the $|\alpha\rangle$ and $|\beta\rangle$ states. This population difference or percent polarization is demonstrated in Fig. 12 for electron, proton, and carbon spins with respect to temperature.

At low temperatures (on the order of 1 K) in a strong magnetic field, the electron polarization is near unity while other nuclei are not, yielding a distribution of uniformly oriented spins S and disoriented spins I (Fig. 13). These spins I and S are coupled through dipolar interactions and this permits the simultaneous reversal of these spins in the same direction (producing two “up” spins) or opposite directions (producing one spin “up” and one spin “down”) if the spins

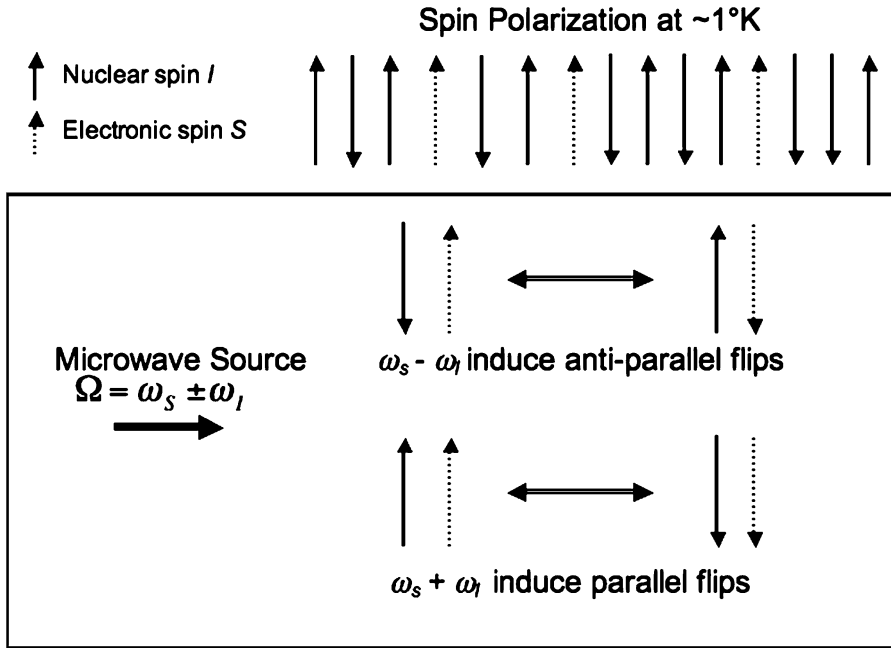


Fig. 13. A graphical representation of spin polarization of the nuclear spin I and electron spin S .

were originally antiparallel. These spin “flips,” which require energy $\hbar(\omega_S \pm \omega_I)$ to occur, are analogous to the spin-lattice relaxation mechanism (T_1 spin relaxation). At low temperatures, the time of this “flip” process for the target nucleus I is on the order of 10^3 s, while it is 10^{-3} s for a lone electron spin S , as a result of its coupling to the lattice. By providing energy via a laser with frequency $\Omega = \omega_S \pm \omega_I$, these flips can be induced and because the order of electron relaxation is much faster than that of the target nucleus, the spins S will bring all of the spins I to their “up” position. It has been shown (Abragam 1978) that the case of antiparallel flips is impossible leading to the association of spin change with $\Omega = \omega_S + \omega_I$. When all of the I spins are in their “up” position, the target material can be deemed hyperpolarized.

It follows that for a low electronic concentration; each spin S must “flip” many nuclear spins. For this to occur, it has been shown that the following condition is required (148):

$$f = \left(\frac{N_I}{T_n} \right) \left(\frac{N_S}{T_c} \right)^{-1} \ll 1$$

where N_I and N_S are the number of respective spins and T_n and T_c are the respective longitudinal relaxation times. With this dipolar coupling as the only means of relaxation, it is assumed that the polarization P_n of the nuclei would reach unity (i.e., that of the electron spins). Due to other mechanisms, such as leakage relaxation as a

result of coupling with another species or saturation by microwaves of frequency ω_s , this nuclear polarization can be much less than P_e (148). In practice, Boer et al. were able to increase the polarization of natural abundance ^{13}C to ~46% in a complex of 1,1,2,2-ethanediol- $(\text{CD}_2\text{OH})_2$ and Cr^{V} (154). Recently, Ardenkjaer-Larsen et al. have shown a method of DNP polarization utilizing a labeled compound at liquid helium temperatures with the introduction of an organic-free radical. These studies have shown polarizations of 37% for ^{13}C and 7.8% for ^{15}N , corresponding to a 44,400- and 23,500-fold enhancement over the equilibrium room temperature polarizations, respectively (143), when the hyperpolarized sample is brought to a liquid at room temperature. It should be pointed out, and as shown in Fig. 12, that at liquid helium temperatures (i.e., 1 K) there is a significant increase equilibrium polarization of approximately 300-fold over room temperature (310 K).

6.2. Hardware and Pulse Sequences

Aside from the traditional NMR spectrometer, DNP-NMR requires the addition of a unit composed of multiple components collectively termed a “polarizer.” The key components of this DNP system are as follows: polarizing magnet, microwave source, variable temperature insert (VTI), sample holder, dissolution system, control electronics, and solid-state NMR monitor (polarimeter). These elements work in concert to take a sample from its native spin polarization state at room temperature to a highly polarized state at room temperature by way of polarization at liquid helium temperatures.

Figure 14 demonstrates a graphical representation of the polarizer and an adjoining high-field magnet. The method described here is analogous to the method described by Ardenkjaer-Larsen et al. (143) though there are other methods of generating DNP (140, 144). A concentrated mixture of ^{13}C -labeled substrate is mixed with an organic-free radical and placed inside of the sample holder. This sample holder is then lowered into the VTI to the center of the magnet. The sample chamber is filled with liquid helium from the magnet dewar and vacuum pumped to a vapor pressure of ~0.8 mbar, resulting in a temperature of ~1.2 K. The sample is then irradiated for typically 60 min at the microwave frequency associated with the free radical (on the order of 94 GHz). As the electron spins polarize the nuclear spins, the polarimeter monitors the percent polarization. Once the solid-state sample has reached maximum polarization, it is mixed with a super-heated buffer (450 K, 10 bar) through the dissolution system. This process takes less than 2–3 s and brings the sample to room temperature while still preserving the low-temperature nuclear polarization (143). The sample is then injected into the medium of interest and observed in a conventional MRI or NMR spectrometer. Control electronics allow for this process of dissolution and injection to be on the order

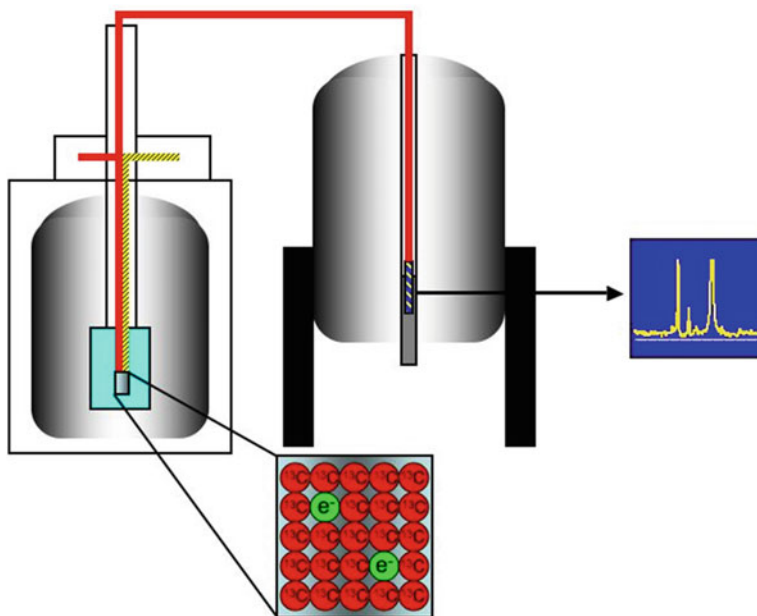


Fig. 14. Schematic of the DNP polarizer/NMR system. DNP (*left*) and high-field NMR system (*center*). The *red line* indicates the flow of the sample after hyperpolarization. The *yellow line* represents the microwave source and its irradiation of the sample chamber. The sample chamber houses the amorphous solid at ~ 1.2 K. After polarization, the sample is observed in the NMR spectrometer. After exposure to an RF signal at frequency $\Omega = \omega_S \pm \omega_I$, the induced flips are shown.

of seconds. At physiological temperatures, the T_1 value of pyruvate carboxyl carbon is the order 40 s, which implies that the initial polarization in the animal is very close to that at the end of the polarization in the microwave polarizer. The effective experimental time available is around $5T_1$ or ca. 200 s, when the sensitivity has decreased to $<1\%$ of its initial value (and see below). Observed magnetization changes can be corrected for the exponential magnetization loss due to relaxation.

Due to the limited lifetime of the substrate polarization, which is proportional to the T_1 relaxation, fast pulse sequences must be implemented *in vivo* and *ex vivo* to capture the real-time substrate metabolism. For both *ex vivo* spectroscopy and *in vivo* single voxel spectroscopic imaging, the task is fairly simple. Generally, a standard direct detected one-dimensional carbon sequence is used with a very small flip angle (on the order of $5\text{--}10^\circ$) for a single scan, and by using a low flip angle, the bulk polarization is preserved in the I_z vector. A 10° flip angle preserves 98% of the magnetization along z , and the x component is 17% of the equilibrium value. This allows for multiple scans to be taken as the substrate is metabolized. Recent studies have shown the effectiveness of small flip angles in hyperpolarized tissue culture experiments, with ^{13}C

signals lasting for minutes of continuous pulses (50, 151, 155). This procedure has also been adapted for in vivo single voxel spectroscopy in rat (149) and mouse models (147, 156) to explore changes in metabolic kinetics. Other pulse sequences have been developed for the probing of polarization transfer experiments as a result of the hyperpolarized substrate (157) as well as the measurement of polarization through dipolar coupling (158). DNP-NMR has also been applied to spectroscopic imaging (all animal experiments) through the development of fast pulse sequences and sampling techniques to achieve both spatial localization and selective spectral resolution on the order of the DNP experiment. Different *k*-space sampling techniques have been utilized to reduce scan time, including centric (150), ellipsoid (159), and spiral (160). This in addition to adiabatic refocused double spin echo sequences (171) and echo planar fly back encoding (150) allow for the acquisition of a $8 \times 8 \times 16$ MRSI matrix with 0.135 cc spatial resolution in under 14 s (150). Least squares chemical shift imaging has also been applied, with a priori knowledge of resonances of interest, to further reduce the number of necessary data points (159).

6.3. Determination of Flux by DNP

There are many applications of DNP for the study of in vivo processes and mechanisms. A recent advancement is the ability to determine flux, through the real-time metabolism of hyperpolarized substrates. This developing technology has been applied to the study of cell slurries (50), perfused organ (151), and cell bioreactor systems (155). The purpose of these studies has been to create a viable and sustained system where hyperpolarized substrates can be introduced. Monitoring of hyperpolarized substrates over time can then produce an assessment of the dynamic net flux at the time of injection.

Many studies have shown the relationship between tumor metabolism and increased aerobic glycolysis, which has been called the Warburg effect after the original discoveries of Otto Warburg in the 1920s (17). DNP ^{13}C NMR allows for spectroscopy on the order of real-time metabolic reaction kinetics and thus visualization of the kinetics associated with fast reactions, such as glycolysis. To date, $^{13}\text{C}_1$ -pyruvate has been the only tracer successfully applied to the study of in vivo hyperpolarized kinetics in order to provide a net flux measurement.

This method that determines flux by DNP and hyperpolarized pyruvate has only been performed in a perfused cell bioreactor model, and not in animals or perfused organs. A bioreactor similar to that described by Gamcsik et al. (103), but using alginate encapsulated cells (161), was used. As has been previously discussed, ^{31}P measurements over time can be utilized as a method to monitor cell health and determine cell viability. A recent study of rat hepatoma cell (JM1) encapsulates perfused in a 3D NMR compatible bioreactor (155) and demonstrates the use of this

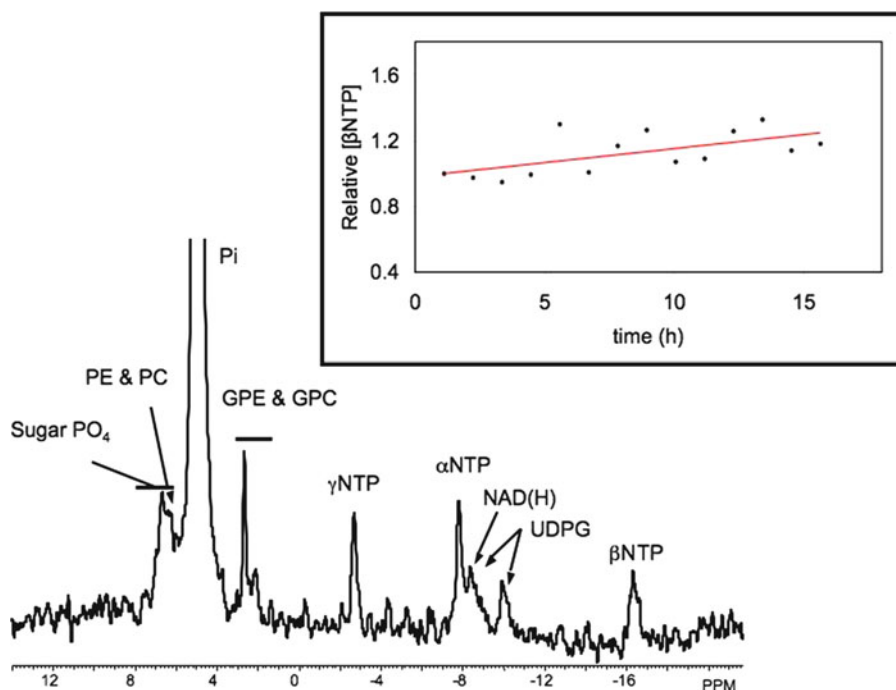


Fig. 15. Representative ^{31}P spectrum of JM1 encapsulated cells after 9 h of perfusion. Peaks corresponding to NTPs demonstrate cell health. The above time course reaffirms the extended cell health over time. Modified from ref. (169).

monitoring and its relationship to DNP. In this study, JM1 cells were monitored using ^{31}P (Fig. 16) to assess cell health and growth. A typical ^{31}P spectrum at 9 h of perfusion shows NTP resonances which imply cells are producing ATP. Increases in these resonances over time demonstrate the growth of these cells (Fig. 15, inset).

After developing a sustainable system, these are then probed using hyperpolarized $1\text{-}^{13}\text{C}$ -pyruvate. Figure 16 demonstrates the labeled lactate produced as a result of infusion of hyperpolarized pyruvate. A representative spectrum at 60 s postinjection of 2 mM $1\text{-}^{13}\text{C}$ -pyruvate shows a lactate resonance with relatively high signal-to-noise. Time course data of lactate production after injection of 2 and 4 mM hyperpolarized pyruvate demonstrate that these concentrations are below enzyme saturation on the order of the experimental time scale, since there is an increase (i.e., doubling of area under the curve) with a doubling of $1\text{-}^{13}\text{C}$ -pyruvate concentration. Taking this data one step further, one can fit the conversion of pyruvate to lactate using a simple two-state model of lactate dehydrogenase (162). This was presented for this study on sequential days of injection of 2 mM pyruvate, as shown in Fig. 17. Though there is a doubling of the apparent rate (k_{app}), when normalized for a doubling of the cell concentration as a result of cell growth (Fig. 15, inset) the flux (V_{app}) is unchanged. This use of

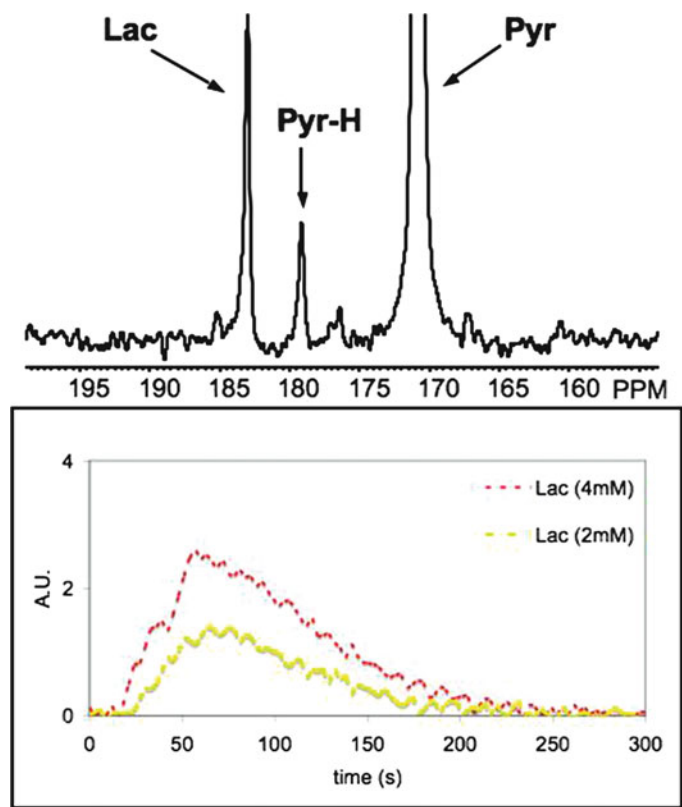


Fig. 16. Representative ^{13}C DNP time courses of JM1 cells. ^{13}C resonances of the carboxylates of pyruvate, lactate, and pyruvate hydrate in JM1 cell encapsulates (top). The time course demonstrates the kinetics of pyruvate metabolism (bottom). Modified from ref. (169).

Injections of 2mM $^{13}\text{C}_1$ Pyruvate

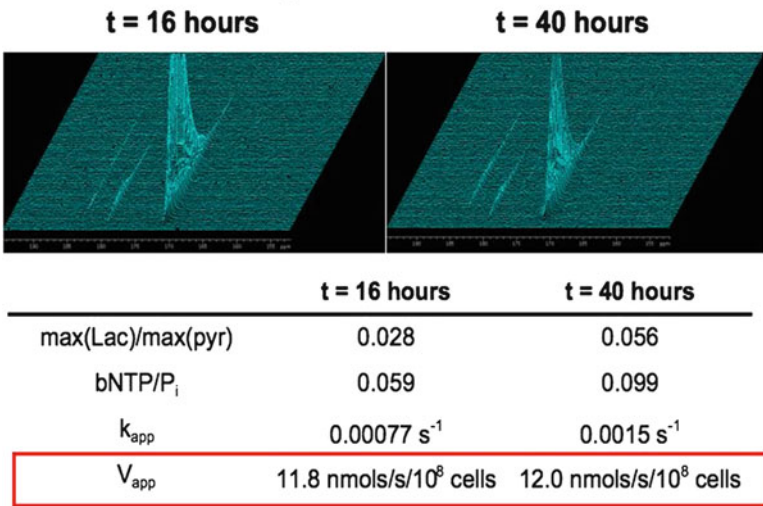


Fig. 17. Stacked plot of the ^{13}C NMR DNP spectra. Top, spectra from Fig. 15 bottom the resulting fitted kinetic parameters. Modified from ref. (169).

simple kinetic modeling in conjunction with a reproducible system, the NMR-compatible perfusion system, allows for the application of DNP and net flux to the characterization of systems and the further understanding of changes in metabolism. These studies demonstrate the first applications of hyperpolarized ^{13}C NMR by the DNP in a viable cell culture system and pave the way for the application of flux determination to both animal and potentially human studies. However, this is a single flux measurement and the concentration of substrate is higher so that the steady state is perturbed, but in a similar manner as Michaelis-Menten constants (K_m) are generated so can this be performed in vivo (162). In order to measure multiple flux rates, liver cells with a normal metabolism, or intact animals, multiple hyperpolarized substrates might be used in the future.

7. Translation ^{13}C NMR Fluxomics to Humans

The fluxomic application of in vivo ^{13}C NMRS in humans has been demonstrated using biofluids and analysis of multiple metabolic processes such as gluconeogenesis, anaplerosis, and pyruvate recycling (75). This patented method uses the ^{13}C NMR spectra of the hepatic metabolism of [U- ^{13}C]-propionate to measure the rates of these metabolic processes and includes a more recent ingenious use of isotope labels and analysis of glucose in human serum (172). Uniformly labeled propionate was selected to ensure that the ^{13}C NMR spectra would contain multiplets to address cases where the ^{13}C enrichment of metabolic products is low (163). Some technical issues relating to human experimentation are provided in Chap. 3.

Specific metabolite spectra measured in this method include glucose, glutamate, glucuronide, and phenylacetylglutamate. The method presents simple equations that relate these measurements to the relative fluxes through anaplerosis, gluconeogenesis, and oxaloacetate-pyruvate recycling. However, the method is applicable to any pathway that intersects the citric acid cycle of the liver.

In humans, blood and urine samples were collected after ingesting [1,2,3- ^{13}C]-propionate, phenylacetate, and acetaminophen to respectively produce the ^{13}C NMR spectrum from glucose and glucuronide or phenylacetylglutamine. The ^{13}C - ^{13}C spin-coupled multiplets of gluconate C2, phenylacetylglutamine C2, and β -D-glucuronate C5 were then utilized to provide estimates of net gluconeogenic flux, OAA-pyruvate recycling, and anaplerotic inflow into oxaloacetate.

The use of stable isotopes has been demonstrated for metabolic functions in humans using biofluid analysis, but most rely on mass spectroscopy analysis. For example, a measurement of cytochrome (CYP) P450 activity was developed using ^{14}C -erythromycin (164).

In this study, gas chromatography-selective ion mass spectrometry (GC-MS) was utilized to measure the amount of a common sedative, midazolam, in plasma as a surrogate measure of the rate of CYP P450 activity. It is known that the cytochrome P450 CYP3A enzymes are the major contributors to midazolam metabolism (165) and specifically CYP3A4 is the dominant isozymes of CYP3A that resides in the liver (166). Therefore, this relationship was used to predict the clearance of midazolam by measuring the activity of a specific enzyme, CYP3A4. This enzyme solely catalyzes the *N*-demethylation of [^{14}C -*N*-methyl]erythromycin in liver (167), forming formaldehyde and ultimately $^{14}\text{CO}_2$ which is quantified in the breath by GC-MS (168). Although this measures just a single reaction, one could combine this breath test with the fluxomic urine analysis-patented fluxomic method to determine additional metabolic pathways.

8. Conclusions and Future Directions

Fluxomics is in its infancy, and with the advent of isotopomeric analysis of human biofluids, a routine yet robust metabolic diagnostic could be translated to humans. However, at present only a handful of metabolic pathways have simultaneously been determined by both static or dynamic methods. In general, dynamic methods are hindered by a lack of temporal resolution required for accurate description of isotopic incorporation and accurate derivation of kinetic parameter from the time course. This is due to the inherent lack of sensitivity of NMRS. This has been overcome by the introduction of DNP technology, which increases ^{13}C NMR sensitivity four orders of magnitude. Static measurements have the best possibility of translating to humans, since these are convenient and require minimal effort and do not require expensive imaging equipment. Finally, nonsteady state is the typical state of most organisms, in a state of maintaining homeostasis at the expense of increasing flux through metabolic pathways. Simpler analytical models of nonsteady state isotopomeric datasets are required in the future to obtain mass balance in biosystems.

Acknowledgments

Funding for the studies was provided by NIH grants GM075941-01, CA114365-01A1, P30ES10126, and RR-000046.

Glossary

Allosteric modification	Usually refers to an enzyme whose activity is modified by the presence of a ligand that binds reversibly to a site other than the active site. In the context of multisite enzyme, such allosteric effectors change the state of the enzyme to enhance or diminish substrate affinity and/or turnover number.
Cellular compartmentation	In cell biology comprise all closed parts within a cell whose lumen is usually surrounded by a single or double lipid layer membrane. Most organelles are compartments like mitochondria, chloroplasts (in photosynthetic organisms), peroxisomes, lysosomes, the endoplasmic reticulum, the cell nucleus, or the Golgi apparatus. Smaller elements like vesicles, and sometimes even microtubules can also be counted as compartments. In general, there are three main cellular compartments, they are: (1) The nuclear compartment comprising the nucleus; (2) The intercisternal space which comprises the space between the membranes of the endoplasmic reticulum (which is continuous with the nuclear envelope); and (3) The cytosol. Metabolically, the mitochondria comprise a very important compartment, even though they are by volume fraction small (from Wikipedia).
Curve fitting	Finding a curve, which matches a series of data points and possibly other constraints. This section is an introduction to both interpolation (where an exact fit to constraints is expected) and regression analysis. Both are sometimes used for extrapolation. Regression analysis allows for an approximate fit by minimizing the difference between the data points and the curve (from Wikipedia).

Dynamic flux measurement method	The measurement of isotope steady state being reached by a time series measure. In the context of this chapter, it is the serial measurement of an NMR-observable tracer, such as ^{13}C , ^{15}N , ^{19}F , ^3H , or ^2H , and its incorporation into a metabolite.
Dynamic nuclear polarization (DNP)	Transfer of polarization from electrons to nuclei, which occurs in a magnetic field, close to absolute zero. This is done by inducing transitions, via oscillating microwave RF pulses, between the allowed energy states of the electrons and nuclei, thus transferring polarization from the electrons to the nuclei. This results in more nuclei aligned with the magnetic field, thus resulting in enhancements of the signal-to-noise on the order of several magnitudes.
Flux	The net rate or the difference between the (unidirectional) rates of the forward and reverse reactions.
Helmholtz NMR coil	A volume coil design for an NMR radiofrequency probe consisting of two connecting loops spanning 120° and separated by 60° .
In vivo fluxomics	The measuring of multiple fluxes in live biosystems using noninvasive analytical instrumentation.
Isotope tracer	Use of isotopically labeled compounds administered at levels that do not affect steady state and can be used to trace flow of atoms through reaction networks.
Isotopic balance	The distribution of a single or multiple isotopes within metabolites of a biosystem.
Mass balance	An application of conservation of mass to the analysis of physical systems. By accounting for material entering and leaving a system, mass flows can be identified. The exact conservation law used in the analysis of the system depends on the context of the problem, but all revolve around mass conservation, i.e., that matter cannot

	disappear or be created spontaneously (from Wikipedia).
Metabolic control analysis	A method for modeling metabolism in which equations are used to describe metabolite concentration and flux, signaling pathways, and genetic pathways.
Metabolic flux analysis (MFA)	An analysis where metabolites are measured such that the amount of metabolite formation can be measured over a given period of time. This allows for the calculation of the rate of formation, or flux, of a metabolite.
Multiple component curve-fit	The mathematical curve fitting of residuals in a time series dataset whereby the various components represent time constants for multiple rates. In the context of this chapter, this relates to metabolite turnover rate within the biosystem.
Net flux	Net flux is sometimes used to define the total flux through a metabolic pathway as some of the individual fluxes can be in reverse of the net flux direction for the entire metabolic pathway.
Non-Steady State Nonallosteric modification	This is usually a description of covalent modification of proteins (cf. post-translational modification) such as phosphorylation that changes the properties of the target protein, e.g., recognition in signal transduction pathways or in chromatin remodeling.
Pool	Like a compartment, a <i>pool</i> is completely defined by the model describing the system. A pool can contain all the members of a particular chemical species for instance, even if they are in several different compartments. A pool can also describe those molecules in a particular physical environment, such as pyruvate in plasma, mitochondria, or cytosol. It can also be a purely theoretical physical space; when a tracer is infused into the bloodstream of an intact animal, the volume of its initial distribution (in plasma, intracellular space, etc.) is thought to describe its pool of entry (20).

Pseudosteady state	A situation in which all state variables remain effectively constant, at least on the macroscopic scale (from Wikipedia).
Quality factor	A dimensionless parameter describing the efficiency of a transceiver, and in context to this chapter, specifically the efficiency of an NMR radiofrequency probe and a measure of the amount of power transmitted to the amount received.
Rate	Speed of a reaction under specified conditions. For simple chemical kinetics, the rate is the first derivative of the product concentration with respect to time, dp/dt , and is equal to a rate constant multiplied by reactant concentrations.
Rate constant	Rate is the product of a rate constant and concentration (strictly, activity). Thus, the units of a rate constant depend on the order of the reaction. For a first order reaction, the rate is $v = k_1 a$, and the first order rate constant k_1 has dimensions in seconds. For a second order reaction, $v = k a.b$ and k has dimensions in M/s. Enzymes saturated with substrate show zero order kinetics with respect to the substrate, $v = V_m$.
Redox state	Redox (shorthand for reduction/oxidation reaction) describes all chemical reactions in which atoms have their oxidation number (oxidation state) changed (from Wikipedia).
Signal-to-noise ratio	The ratio of signal peak to the average noise factor. Specifically, the ratio of NMR peak heights of peaks from measurable compounds to noise peaks. To improve the signal-to-noise ratio by a factor of 2, one must acquire a factor of 4 more transients.
Single component curve-fit	The mathematical curve fitting of residuals in a time series dataset whereby a single component represents a time constant for a rate. In the context of this chapter, this relates to metabolite turnover rate within the biosystem.

Solenoid NMR coil	A volume coil design for an NMR radiofrequency probe consisting of a wound wire or coil, like a spring, whereby the optimum spacing f loops is equal to the wire diameter.
Static flux measurement method	A method of flux analysis whereby ^{13}C fractional enrichment or isotopomers are quantified in a single sample at steady state.
Steady state	A situation in which all state variables are constant in spite of ongoing processes that strive to change them. For an entire system to be at steady state, i.e., for all state variables of a system to be constant, there must be a flow through the system (compare mass balance) (from Wikipedia).
Volume of distribution	A value used to describe the distribution of a xenobiotic between blood plasma and the rest of the body. Xenobiotics with higher volumes of distribution are generally lipid-soluble and thus have low blood plasma concentrations after dosing. Those with lower volumes of distribution are generally more polar and thus have high blood plasma concentrations after dosing.

References

1. Murray RK, Granner DK, Rodwell VW, editors. Harper's illustrated biochemistry, 27th ed. New York: The McGraw-Hill Companies Inc.; 2006.
2. Nelson DL, Cox MM, editors. Lehninger principles of biochemistry, vol. 4. 4th ed. New York: W.H. Freeman & Company; 2004.
3. Wegener G, Krause U. Different modes of activating phosphofructokinase, a key regulatory enzyme of glycolysis, in working vertebrate muscle. *Biochem Soc Trans.* 2002;30(2):264–70.
4. Hunsucker SA, Mitchell BS, Spychala J. The 5'-nucleotidases as regulators of nucleotide and drug metabolism. *Pharmacol Ther.* 2005;107(1):1–30.
5. Huang M, Graves LM. De novo synthesis of pyrimidine nucleotides; emerging interfaces with signal transduction pathways. *Cell Mol Life Sci.* 2003;60(2):321–36.
6. Mathews CK. DNA precursor metabolism and genomic stability. *FASEB J.* 2006;20(9):1300–14.
7. Yeung M, Thiele I, Palsson BO. Estimation of the number of extreme pathways for metabolic networks. *BMC Bioinformatics.* 2007;8(1):363.
8. Vo TD, Palsson BO. Isotopomer analysis of myocardial substrate metabolism: a systems biology approach. *Biotechnol Bioeng.* 2006;95(5):972–83.
9. Lee DY, Yun H, Park S, Lee SY. MetaFluxNet: the management of metabolic reaction information and quantitative metabolic flux analysis. *Bioinformatics.* 2003;19:2144–6.
10. Wiechert W, Schweissgut O, Takanaga H, Frommer WB. Fluxomics: mass spectrometry versus quantitative imaging. *Curr Opin Plant Biol.* 2007;10(3):323–30.

11. Droste P, Weitzel M, Wiechert W. Visual exploration of isotope labeling networks in 3D. *Bioprocess Biosyst Eng.* 2008;31(3):227–39.
12. Massou S, Nicolas C, Letisse F, Portais JC. NMR-based fluxomics: quantitative 2D NMR methods for isotopomers analysis. *Phytochemistry.* 2007;68(16–18):2330–40.
13. Ataullakhanov FI, Vitvitsky VM. What determines the intracellular ATP concentration. *Biosci Rep.* 2002;22(5–6):501–11.
14. Diaz J, Hetzer G, Tello L. An energy balance climate model with hysteresis. *Nonlinear Anal.* 2006;64(9):2053–74.
15. Hatzianastassiou N, Fotiadi A, Matsoukas C, Pavlakis KG, Drakakis E, Hatzidimitriou D, Vardavas I. Long-term global distribution of Earth's shortwave radiation budget at the top of atmosphere. *Atmos Chem Phys.* 2004;4:1217–35.
16. Cai M. Dynamical amplification of polar warming. *Geophys Res Lett.* 2005;32(22):22710.
17. Warburg O, Wind F, Negelein E. The metabolism of tumors in the body. *J Gen Physiol.* 1927;3:519–30.
18. Gruetter R, Magnusson I, Rothman DL, Avision MJ, Shulman RG, Shulman GI. Validation of ^{13}C NMR measurements of liver glycogen in vivo. *Magn Reson Med.* 1994;31(6):583–8.
19. Lee K, Berthiaume F, Stephanopoulos GN, Yarmush DM, Yarmush ML. Metabolic flux analysis of postburn hepatic hypermetabolism. *Metab Eng.* 2000;2(4):312–27.
20. Laughlin MR, Kelleher JK. Tracer theory and ^{13}C NMR. In: Berliner LJ, Robitaille P-M, editors. *Biological magnetic resonance: in vivo carbon-13 NMR.* New York: Kluwer Academic Publishers; 2002.
21. Sherry AD, Malloy CR. Biological magnetic resonance: in vivo carbon-13 NMR: ^{13}C isotopomer analysis of glutamate. A NMR method to probe metabolic pathways intersecting in the citric acid cycle. In: Berliner LJ, Robitaille PM, editors. *Biological magnetic resonance: in vivo carbon-13 NMR.* New York: Kluwer Academic Publishers; 2002.
22. Geissler A, Kanamori K, Ross BD. Real-time study of the urea cycle using ^{15}N NMR in the isolated perfused rat liver. *Biochem J.* 1992;287:813–20.
23. Grunder W, Krumbiegel P, Gersonde K. ^{15}N NMR of glycine metabolism in liver, muscle, and kidney using a new pulsed overhauser technique (POE). *Isotopenpraxis Isot Environ Health Stud.* 1992;28:81–4.
24. Gabel SA, London RE. A deuterium surface coil nmr study of the metabolism of D-methionine in the liver of the anesthetized rat. *Biochemistry.* 1988;27(20):7864–9.
25. Nissim I, Lapidot A. Plasma amino acid turnover rates and pools in rabbits: in vivo studies using stable isotopes. *Am J Physiol.* 1979;237(5):E418–27.
26. Wagenmakers AJ. Tracers to investigate protein and amino acid metabolism in human subjects. *Proc Nutr Soc.* 1999;58(4):987–1000.
27. Guillet C, Boirie Y, Walrand S. An integrative approach to in-vivo protein synthesis measurement: from whole tissue to specific proteins. *Curr Opin Clin Nutr Metab Care.* 2004;7(5):531–8.
28. Zawulich WS. Modulation of insulin secretion from beta-cells by phosphoinositide-derived second-messenger molecules. *Diabetes.* 1988;37(2):137–41.
29. Lodish H, Berk A, Zipursky SL, Matsudaira P, Baltimore D, Darnell J. *Molecular cell biology.* New York: W.H. Freeman & Company; 1999.
30. Jahoor F, Burrin DG, Reeds PJ, Frazer M. Measurement of plasma protein synthesis rate in infant pig: an investigation of alternative tracer approaches. *Am J Physiol.* 1994;267(1 Pt 2):R221–7.
31. Berthold HK, Jahoor F, Klein PD, Reeds PJ. Estimates of the effect of feeding on whole-body protein degradation in women vary with the amino acid used as tracer. *J Nutr.* 1995;125(10):2516–27.
32. Morell P, Ousley AH. Metabolic turnover of myelin glycerophospholipids. *Neurochem Res.* 1994;19(8):967–74.
33. Rapoport SI. In vivo approaches and rationale for quantifying kinetics and imaging brain lipid metabolic pathways. *Prostaglandins Other Lipid Mediat.* 2005;77(1–4):185–96.
34. Ritz P, Coward WA. Doubly labelled water measurement of total energy expenditure. *Diabete Metab.* 1995;21(4):241–51.
35. Damjanovich S, Nagy I, Somogyi B. Application of a molecular enzyme kinetic model for aging cells and tissues. *Arch Gerontol Geriatr.* 1989;8(1):37–45.
36. Finch CE, Morgan DG. RNA and protein metabolism in the aging brain. *Annu Rev Neurosci.* 1990;13:75–88.
37. Grimble GK, Malik SB, Boza JJ. Methods for measuring tissue RNA turnover. *Curr Opin Clin Nutr Metab Care.* 2000;3(5):399–408.
38. Preston CC, Oberlin AS, Holmuamedov EL, Gupta A, Sagar S, Syed RH, Siddiqui

- SA, Raghavakaimal S, Terzic A, Jahangir A. Aging-induced alterations in gene transcripts and functional activity of mitochondrial oxidative phosphorylation complexes in the heart. *Mech Ageing Dev.* 2008;129(6):304–12.
39. White RJ. RNA polymerases I and III, growth control and cancer. *Nat Rev Mol Cell Biol.* 2005;6(1):69–78.
 40. Kurhanewicz J, Bok R, Nelson SJ, Vigneron DB. Current and potential applications of clinical ^{13}C MR spectroscopy. *J Nucl Med.* 2008;49(3):341–4.
 41. Gadian DG, editor. *NMR and its applications to living systems.* New York: Oxford University Press; 1995.
 42. Mashimo K, Ohno Y. Ethanol hyperpolarizes mitochondrial membrane potential and increases mitochondrial fraction in cultured mouse myocardial cells. *Arch Toxicol.* 2006;80:421–8.
 43. Thurman RG, Kauffman FC, Ji S, Lemasters JJ, Conway JG, Belinsky SA, Kashiwagi T, Matsamura T. Metabolic heterogeneity in the perfused rat liver. *Pharmacol Biochem Behav.* 1983;18 Suppl 1:415–9.
 44. Testa C, Schiavina R, Lodi R, Salizzoni E, Corti B, Farsad M, Kurhanewicz J, Manferrari F, Brunocilla E, Tonon C, Monetti N, Castellucci P, Fanti S, Coe M, Grigioni WF, Martorana G, Canini R, Barbiroli B. Prostate cancer: sextant localization with MR imaging, MR spectroscopy, and ^{11}C -choline PET/CT. *Radiology.* 2007;244(3):797–806.
 45. Macdonald JM, Schmidlin O, James TL. In vivo monitoring of hepatic glutathione in anesthetized rats by ^{13}C NMR. *Magn Reson Med.* 2002;48(3):430–9.
 46. Robbins E. Radiation risks from imaging studies in children with cancer. *Pediatr Blood Cancer.* 2008;51(4):453–7.
 47. Isambert A, Bonniaud G, Lavielle F, Malandain G, Lefkopoulou D. A phantom study of the accuracy of CT, MR and PET image registrations with a block matching-based algorithm. *Cancer Radiother.* 2008;12(8):800808.
 48. Pichler BJ, Wehrl HF, Judenhofer MS. Latest advances in molecular imaging instrumentation. *J Nucl Med.* 2008;49 Suppl 2:5S–23.
 49. Ikoma Y, Watabe H, Shidahara M, Naganawa M, Kimura Y. PET kinetic analysis: error consideration of quantitative analysis in dynamic studies. *Ann Nucl Med.* 2008;22(1):1–11.
 50. Day SE, Kettunen MI, Gallagher FA, Hu DE, Lerche M, Wolber J, Golman K, Ardenkjaer-Larsen JH, Brindle KM. Detecting tumor response to treatment using hyperpolarized ^{13}C magnetic resonance imaging and spectroscopy. *Nat Med.* 2007;13(11):1382–7.
 51. Szyperski T. ^{13}C -NMR MS and metabolic flux balancing in biotechnology research. *Q Rev Biophys.* 1998;31(1):41–106.
 52. London RE. Carbon-13 labeling in studies of metabolic regulation. *Prog Nucl Magn Reson Spectrosc.* 1988;20:337–83.
 53. Stephanopoulos G, Aristidou A, Nielsen J. *Metabolic engineering.* San Diego: Academic; 1998.
 54. Walker TE, Han CH, Kollman VH, London RE, Matwiyoff NA. ^{13}C nuclear magnetic resonance studies of the biosynthesis by microbacterium ammoniaphilum of L-glutamate selectively enriched with carbon-13. *J Biol Chem.* 1982;257:1189–95.
 55. Beylot M, David MV, Landau BR, Brunen-graber H. Tracing hepatic gluconeogenesis relative to citric acid cycle activity in vitro and in vivo. comparisons in the use of $[3-^{13}\text{C}]$ lactate, $[2-^{13}\text{C}]$ acetate, and α -keto $[3-^{13}\text{C}]$ isocaproate. *J Biol Chem.* 1995;270:1509–14.
 56. Jones JG, Le TH, Storey CJ, Sherry RA, Malloy CR, Burton KP. Effects of different oxidative insults on intermediary metabolism in isolated perfused rat hearts. *Free Radic Biol Med.* 1996;20:515–23.
 57. Jones JG, Sherry RA, Malloy CR. Quantitation of gluconeogenesis by ^2H nuclear magnetic resonance analysis of plasma glucose following ingestion of $^2\text{H}_2\text{O}$. *Anal Biochem.* 2000;277:121–6.
 58. Jones JG, Solomon MA, Sherry RA, Jeffrey FM, Malloy CR. ^{13}C NMR measurements of human gluconeogenic fluxes after ingestion of $[\text{U}-^{13}\text{C}]$ propionate, phenylacetate, and acetaminophen. *Am J Physiol Endocrinol Metab.* 1998;275:843–52.
 59. Magnusson I, Chandramouli V, Schumann WC, Kumaran K, Wahren J, Landau BR. Pentose pathway in human liver. *Proc Natl Acad Sci.* 1988;85:4682–5.
 60. Magnusson I, Schumann WC, Bartsch GE, Chandramouli V, Kumaran K, Wahren J, Landau BR. Noninvasive tracing of Krebs cycle metabolism in liver. *J Biol Chem.* 1991;266:6975–84.
 61. Mancuso A, Sharfstein ST, Fernandez EJ, Clark DS, Blanch HW. Effect of extracellular glutamine concentration on primary and secondary metabolism of a murine hybridoma: an in vivo ^{13}C nuclear magnetic resonance study. *Biotechnol Bioeng.* 1998;57:172–86.

62. Shulman GI, Rothman DL, Smith D, Johnson CM, Blair JB, Shulman RG, et al. Mechanism of liver glycogen repletion in vivo by nuclear magnetic resonance spectroscopy. *J Clin Invest.* 1985;76(3):1229–36.
63. Ugurbil K, Brown TR, Hollander JAD, Glynn P, Shulman RG. High-resolution ^{13}C nuclear magnetic resonance studies of glucose metabolism in *Escherichia coli*. *Proc Natl Acad Sci U S A.* 1978;75(8):3742–6.
64. Sato K, Kashiwaya Y, Keon CA, Tsuchiya N, King MT, Radda GK, Chance B, Clarke K, Veech RL. Insulin, ketone bodies, and mitochondrial energy transduction. *FASEB J.* 1995;9(8):651–8.
65. Mayevsky A, Nioka S, Chance B. Fiber optic surface fluorometry/reflectometry and ^{31}P -NMR for monitoring the intracellular energy state in vivo. *Adv Exp Med Biol.* 1988;222:365–74.
66. Unkefer CJ, London RE. In vivo studies of pyridine nucleotide metabolism in *Escherichia coli* and *Saccharomyces cerevisiae* by carbon- ^{13}C NMR spectroscopy. *J Biol Chem.* 1984;259(4):2311–20.
67. Chung Y, Jue T. ^1H NMR observation of redox potential in liver. *Biochemistry.* 1992;31(45):11159–65.
68. Willis JA, Schleich T. Oxidative-stress induced protein glutathione mixed-disulfide formation in the ocular lens. *Biochim Biophys Acta.* 1996;1313(1):20–8.
69. Kreutzer U, Jue T. ^1H -nuclear magnetic resonance deoxy myoglobin signal as indicator of intracellular oxygenation in myocardium. *Am J Physiol.* 1991;261(6 Pt 2):H2091–7.
70. Tran TK, Kreutzer U, Jue T. Observing the deoxy myoglobin and hemoglobin signals from rat myocardium in situ. *FEBS Lett.* 1998;434(3):309–12.
71. Seagle C, Christie MA, Winnike JH, McClelland RE, Ludlow JW, O'Connell TM, Gamcsik MP, Macdonald JM. High-throughput nuclear magnetic resonance metabolomic footprinting for tissue engineering. *Tissue Eng Part C Methods.* 2008;14(2):107–18.
72. Todd A. Inclusion of a glycogen regulation mathematical model into a contextual metabolic framework. In: *Applied mathematics*. Chapel Hill: University of North Carolina; 2007. p. 193.
73. Sherry AD, Malloy CR. Isotopic methods for probing organization of cellular metabolism. *Cell Biochem Funct.* 1996;14:259–68.
74. Ratcliffe RG, Shachar-Hill Y. Measuring multiple fluxes through plant metabolic networks. *Plant J.* 2006;45:490–511.
75. Jones JG, Sherry D, Jeffrey FMH, Cottam GL, Malloy CR. Methods for determining gluconeogenesis, anaplerosis, and pyruvate recycling. Patent US6,329,208 B1; 2001.
76. Cohen SM. Simultaneous ^{13}C and ^{31}P NMR studies of perfused rat liver. Effects of insulin and glucagon and a ^{13}C NMR assay of free Mg^{2+} . *J Biol Chem.* 1983;258(23):14294–308.
77. Chatham JC, Forder JR. Metabolic compartmentation of lactate in the glucose-perfused rat heart. *Am J Physiol.* 1996;270(1 Pt 2):H224–9.
78. Chatham JC, Forder JR, Glickson JD, Chance EM. Calculation of absolute metabolic flux and the elucidation of the pathways of glutamate labeling in perfused rat heart by ^{13}C NMR spectroscopy and nonlinear least squares analysis. *J Biol Chem.* 1995;270(14):7999–8008.
79. Sandström J. Dynamic N.M.R. spectroscopy. London: Academic; 1982. p. 1226.
80. Cohen SM, Shulman RG, McLaughlin AC. Effects of ethanol on alanine metabolism in perfused mouse liver studied by ^{13}C NMR. *Proc Natl Acad Sci U S A.* 1979;76(10):4808–12.
81. London RE. In vivo ^2H NMR studies of cellular metabolism. In: Berliner LJ, Reuben J, editors. *Biological magnetic resonance: NMR of paramagnetic molecules*. New York: Kluwer Academic Publishers; 1998.
82. Thoma WJ, Ugurbil K. Saturation-transfer studies of ATP-Pi exchange in isolated perfused rat liver. *Biochim Biophys Acta.* 1987;893(2):225–31.
83. Henry PG, Adriany G, Deelchand D, Gruetter R, Marjanska M, Oz G, Seaquist ER, Shetov A, Ugurbil K. In vivo ^{13}C NMR spectroscopy and metabolic modeling in the brain: a practical perspective. *Magn Reson Imaging.* 2006;24(4):527–39.
84. Henry PG, Tkac I, Gruetter R. ^1H -localized broadband ^{13}C NMR spectroscopy of the rat brain in vivo at 9.4 T. *Magn Reson Med.* 2003;50(4):684–92.
85. Gruetter R, Adriany G, Choi IY, Henry PG, Lei HX, Oz G. Localized in vivo ^{13}C NMR spectroscopy of the brain. *NMR Biomed.* 2003;16(6–7):313–38.
86. deGraaf RA, Mason GF, Patel AB, Behar KL, Rothman DL. In vivo ^1H - ^{13}C -NMR spectroscopy of cerebral metabolism. *NMR Biomed.* 2003;16(6–7):339–57.
87. Seymour AML. Imaging cardiac metabolism in heart failure: the potential of NMR

- spectroscopy in the era of metabolism revisited. *Heart Lung Circ.* 2003;12:25–30.
88. Lewandowski ED. Biological magnetic resonance: in vivo carbon-13 NMR: metabolic flux and subcellular transport of metabolites. In: Berliner LJ, Robitaille PM, editors. *Biological magnetic resonance: in vivo carbon-13 NMR*, vol. 15. New York: Kluwer Academic Publishers; 1998.
 89. Weiss RG, Gerstenblith G. Biological magnetic resonance: in vivo carbon-13 NMR. In: Berliner LJ, Robitaille PM, editors. *Assessing cardiac metabolic rates during pathologic conditions with dynamic ¹³C NMR spectra* biological magnetic resonance: in vivo carbon-13 NMR, vol. 15. New York: Kluwer Academic Publishers; 1998.
 90. Borgias BA, James TL. Two-dimensional nuclear Overhauser effect: complete relaxation matrix analysis. *Methods Enzymol.* 1989;176:169–83.
 91. Mendes P. Emerging bioinformatics for the metabolome. *Brief Bioinform.* 2002;3(2):134–45.
 92. Macdonald JM. Toxicological applications of cell and animal models for in vivo nuclear magnetic resonance spectroscopy. San Francisco: University of California at San Francisco; 1995.
 93. Silbernagl S, Volker K, Dantzer WH. Compartmentation of amino acids in the rat kidney. *Am J Physiol.* 1996;270(1 Pt 2):F154–63.
 94. Alger JR, Sillerud LO, Behar KL, Gillies RJ, Shulman RG, Gordon RE, Shaw D, Hanley PE. In vivo carbon-13 nuclear magnetic resonance studies of mammals. *Science.* 1981;214:660–2.
 95. Enderle JD, Blanchard SM, Bronzino JD. *Introduction to biomedical engineering*. Boston: Elsevier Academic Press; 2005.
 96. York MJ, Kuchel PW, Chapman BE, Jones AJ. Incorporation of labelled glycine into reduced glutathione of intact human erythrocytes by enzyme-catalysed exchange. *Biochem J.* 1982;207:65–72.
 97. Roser W, Beckmann N, Wiesmann U, Seelig J. Absolute quantification of the hepatic glycogen content in a patient with glycogen storage disease by ¹³C magnetic resonance spectroscopy. *Magn Reson Imaging.* 1996;14(10):1217–20.
 98. Gruetter R, Magnusson I, Rothman DL, Avision MJ, Shulman RG, Shulman GI. Validation of ¹³C NMR measurements of liver glycogen in vivo. *Magn Reson Med.* 1994;31(6):583–8.
 99. Murphy E, Gabel SA, Funk A, London RE. NMR observability of ATP: preferential depletion of cytosolic ATP during ischemia in perfused rat liver. *Biochemistry.* 1988;27(2):526–8.
 100. Masson S, Quistorff B. The ³¹P NMR visibility of ATP in perfused rat liver remains about 90%, unaffected by changes of metabolic state. *Biochemistry.* 1992;31(33):7488–93.
 101. Kurhanewicz J, Swanson MG, Nelson SJ, Vigneron DB. Combined magnetic resonance imaging and spectroscopic imaging approach to molecular imaging of prostate cancer. *J Magn Reson Imaging.* 2002;16(4):451–63.
 102. Nicholson JK, Timbrell JA, Bales JR, Sadler PJ. A high resolution proton nuclear magnetic resonance approach to the study of hepatocyte and drug metabolism. Application to acetaminophen. *Mol Pharmacol.* 1985;27(6):634–43.
 103. Gamcsik MP, Millis KK, Colvin OM. Noninvasive detection of elevated glutathione levels in MCF-7 cells resistant to 4-hydroperoxycyclophosphamide. *Cancer Res.* 1995;55(10):2012–6.
 104. Tian J, Yin Y, Sun H, Luo X. Magnesium chloride: an efficient ¹³C NMR relaxation agent for amino acids and some carboxylic acids. *J Magn Reson.* 2002;159(2):137–44.
 105. London RE, Rhee CK, Murphy E, Gabel S, Levy LA. NMR-sensitive fluorinated and fluorescent intracellular calcium ion indicators with high dissociation constants. *Am J Physiol.* 1994;266(5 Pt 1):C1313–22.
 106. Hoener BA, Tzika AA, Englestad BL, White DL. Hepatic transport of the magnetic resonance imaging contrast agent Fe(III)-N-(3-phenylglutaryl)desferrioxamine B. *Magn Reson Med.* 1991;17(2):509–15.
 107. Chance EM, Seeholzer SH, Kobayashi K, Williamson JR. Mathematical analysis of isotope labeling in the citric acid cycle with applications to ¹³C NMR studies in perfused rat hearts. *J Biol Chem.* 1983;258(22):13785–94.
 108. Novotny EJ, Fulbright RK, Pearl PL, Gibson KM, Rothman DL. Magnetic resonance spectroscopy of neurotransmitters in human brain. *Ann Neurol.* 2003;54 Suppl 6:S25–31.
 109. Waagepetersen HS, Sonnewald U, Schousboe A. Compartmentation of glutamine, glutamate, and GABA metabolism in neurons and astrocytes: functional implications. *Neuroscientist.* 2003;9(5):398–403.
 110. Shen J, Petersen KF, Behar KL, Brown P, Nixon TW, Mason GF, Petroff OA, Shulman GI, Shulman RG, Rothman DL.

- Determination of the rate of the glutamate/glutamine cycle in the human brain by in vivo ^{13}C NMR. *Proc Natl Acad Sci.* 1999;96(14):8235–40.
111. Sonnewald U, Westergaard N, Hassel B, Muller TB, Unsgard G, Fonnum F, Hertz L, Schousboe A, Petersen SB. NMR spectroscopic studies of ^{13}C acetate and ^{13}C glucose metabolism in neocortical astrocytes: evidence for mitochondrial heterogeneity. *Dev Neurosci.* 1993;15(3–5):351–8.
 112. Melo TM, Nehlig A, Sonnewald U. Neuronal-glial interactions in rats fed a ketogenic diet. *Neurochem Int.* 2006;48(6–7):498–507.
 113. Hassel B, Sonnewald U, Fonnum F. Glial-neuronal interactions as studied by cerebral metabolism of $[2-^{13}\text{C}]$ acetate and $[1-^{13}\text{C}]$ glucose: an ex vivo ^{13}C NMR spectroscopic study. *J Neurochem.* 1995;64(6):2773–82.
 114. Snell K, Walker DG. The adaptive behaviour of isoenzyme forms of rat liver alanine aminotransferases during development. *Biochem J.* 1972;128(2):403–13.
 115. Pasternack LB, Laude DA, Appling DR. ^{13}C NMR detection of folate-mediated serine and glycine synthesis in vivo in *Saccharomyces cerevisiae*. *Biochemistry.* 1992;31(37):8713–9.
 116. Jones JG, Naidoo R, Sherry AD, Jeffrey FM, Cottam GL, Malloy CR. Measurement of gluconeogenesis and pyruvate recycling in the rat liver: a simple analysis of glucose and glutamate isotopomers during metabolism of $[1,2,3-(^{13}\text{C})_3]$ propionate. *FEBS Lett.* 1997;412(1):131–7.
 117. Cohen SM, Rognstad R, Shulman RG, Katz J. A comparison of ^{13}C nuclear magnetic resonance and ^{14}C tracer studies of hepatic metabolism. *J Biol Chem.* 1981;256(7):3428–32.
 118. Healing G, Smith D. *Handbook of pre-clinical continuous intravenous infusion.* New York: Taylor & Francis; 2000.
 119. Myers R. *The radio amateur's handbook: the standard manual of amateur radio communication.* Newington: The American Radio Relay League; 1995.
 120. Schmidt HC, Gooding CA, James TL. In vivo ^{31}P -MR spectroscopy of the liver in the infant rabbit to study the effect of hypoxia on the phosphorus metabolites and intracellular pH. *Invest Radiol.* 1986;21(2):156–61.
 121. Wald LL, Carvajal L, Moyher SE, Nelson SJ, Grant PE, Barkovich AJ, Vigneron DB. Phased array detectors and an automated intensity-correction algorithm for high-resolution MR imaging of the human brain. *Magn Reson Med.* 1995;34(3):433–9.
 122. Wald LL, Moyher SE, Day MR, Nelson SJ, Vigneron DB. Proton spectroscopic imaging of the human brain using phased array detectors. *Magn Reson Med.* 1995;34(3):440–5.
 123. Benveniste H, Blackband SJ. Translational neuroscience and magnetic-resonance microscopy. *Lancet Neurol.* 2006;5(6):536–44.
 124. Wright SM, Wald LL. Theory and application of array coils in MR spectroscopy. *NMR Biomed.* 1997;10(8):394–410.
 125. Thelwall PE, Yemin AY, Gillian TL, Simpson NE, Kasibhatla MS, Rabbani ZN, Macdonald JM, Blackband SJ, Gamcsik MP. Noninvasive in vivo detection of glutathione metabolism in tumors. *Cancer Res.* 2005;65(22):10149–53.
 126. Bottomley PA, Edelstein WA, Hart HR, Schenck JF, Smith LS. Spatial localization in ^{31}P and ^{13}C NMR spectroscopy in vivo using surface coils. *Magn Reson Med.* 1984;1(3):410–3.
 127. Fan TW, Higashi RM. Reproducible nuclear magnetic resonance surface coil fabrication by combining computer-aided design and a photoresist process. *Anal Chem.* 1989;61(6):636–8.
 128. Mulquin PJ, Kuchel PW. *Modeling metabolism with mathematica.* Boca Raton: CRC Press; 2003.
 129. Stephanopoulos GN, Aristidou AA, Nielsen J. *Metabolic engineering: principles and methodologies.* San Diego: Academic; 1998.
 130. Palsson BO. *Systems biology: properties of reconstructed networks.* New York: Cambridge University Press; 2006.
 131. Heinrich R, Schuster S. *The regulation of cellular systems.* New York: Chapman & Hall; 1996.
 132. Fell DA. *Understanding the control of metabolism.* London: Portland Press; 1997.
 133. Kacser H, Burns JA. The control of flux. *Symp Soc Exp Biol.* 1973;27:65–104 (reprinted with modern terms in: Kacser H, Burns JA, Fell DA. *Biochem Soc Trans.* 1995;23:341–66).
 134. Heinrich R, Rapoport TA. A linear steady-state treatment of enzymatic chains. Critique of the crossover theorem and a general procedure to identify interaction sites with an effector. *Eur J Biochem.* 1974;42:97–105.
 135. Heinrich R, Rapoport TA. A linear steady-state treatment of enzymatic chains. General properties, control and effector strength. *Eur J Biochem.* 1974;42:89–95.
 136. Jucker BM, Barucci N, Shulman GI. Metabolic control analysis of insulin-stimulated glucose disposal in rat skeletal muscle. *Am J*

- Physiol Endocrinol Metab. 1999;277:E505–12.
137. Fell DA. MCA: a survey of its theoretical and experimental development. *Biochem J.* 1992;286:313–30.
 138. Klamt S, Stelling J, Ginkel M, Gilles ED. Flux analyzer: exploring structure, pathways and flux distributions in metabolic networks on interactive flux maps. *Bioinformatics.* 2003;19:261–9.
 139. Hoops S, Sahle S, Gauges R, Lee C, Pahle J, Simus N, Singhal M, Xu L, Mendes P, Kummer U. COPASI—a complex pathway simulator. *Bioinformatics.* 2006;22:3067–74.
 140. Golman K, Axelsson O, Johannesson H, Mansson S, Olofsson C, Petersson JS. Parahydrogen-induced polarization in imaging: subsecond (^{13}C) angiography. *Magn Reson Med.* 2001;46(1):1–5.
 141. Goodson BM. Nuclear magnetic resonance of laser-polarized noble gases in molecules, materials, and organisms. *J Magn Reson.* 2002;155(2):157–216.
 142. Golman K, Ardenkjaer-Larsen JH, Petersson JS, Mansson S, Leunbach I. Molecular imaging with endogenous substances. *Proc Natl Acad Sci U S A.* 2003;100(18):10435–9.
 143. Ardenkjaer-Larsen JH, Fridlund B, Gram A, Hansson G, Hansson L, Lerche MH, Servin R, Thaning M, Golman K. Increase in signal-to-noise ratio of $>10,000$ times in liquid-state NMR. *Proc Natl Acad Sci U S A.* 2003;100(18):10158–63.
 144. Bowers CR, Weitekamp DP. Parahydrogen and synthesis allow dramatically enhanced nuclear alignment. *J Am Chem Soc.* 1987;109:5541–2.
 145. Canet D, Aroulanda C, Mutzenhardt P, Aime S, Gobetto R, Reineri F. Para-hydrogen enrichment and hyperpolarization. *Concepts Magn Reson.* 2006;28A(5):321–30.
 146. Pravica MG, Weitekamp DP. Net NMR alignment by adiabatic transport of parahydrogen addition products to high magnetic field. *Chem Phys Lett.* 1998;145(4):255–8.
 147. Goldman M, Johannesson H, Axelsson O, Karlsson M. Hyperpolarization of ^{13}C through order transfer from parahydrogen: a new contrast agent for MRI. *Magn Reson Imaging.* 2005;23(2):153–7.
 148. Abragam A, Goldman M. Principles of dynamic nuclear polarization. *Rep Prog Phys.* 1978;41:396–467.
 149. Kohler SJ, Yen Y, Wolber J, Chen AP, Albers MJ, Bok R, Zhang V, Tropp J, Nelson S, Vigneron DB, Kurhanewicz J, Hurd RE. In vivo ^{13}C carbon metabolic imaging at 3 T with hyperpolarized ^{13}C -1-pyruvate. *Magn Reson Med.* 2007;58(1):65–9.
 150. Chen AP, Cunningham CH, Ozturk-Isik E, Xu D, Hurd RE, Kelley DA, Pauly JM, Kurhanewicz J, Nelson SJ, Vigneron DB. High-speed 3 T MR spectroscopic imaging of prostate with flyback echo-planar encoding. *J Magn Reson Imaging.* 2007;25(6):1288–92.
 151. Merritt ME, Harrison C, Storey C, Jeffrey FM, Sherry AD, Malloy CR. Hyperpolarized ^{13}C allows a direct measure of flux through a single enzyme-catalyzed step by NMR. *Proc Natl Acad Sci U S A.* 2007;104(50):19773–7.
 152. Overhauser AW. Polarization of nuclei in metals. *Phys Rev.* 1953;92(2):411–5.
 153. Abragam A. Overhauser effect in nonmetals. *Phys Rev.* 1955;98(6):1729–35.
 154. Boer WD, Borghini M, Morimoto K, Niinikoski TO, Udo F. Dynamic polarization of protons, deuterons, and carbon- 13 nuclei: thermal contact between nuclear spins and an electron spin-spin interaction reservoir. *J Low Temp Phys.* 1974;15:249–67.
 155. Keshari KR, Kurhanewicz J, Wilson DM, Jeffries RE, Dewar BJ, Van Criekinge M, et al. Hyperpolarized ^{13}C spectroscopy and a novel NMR-compatible bioreactor system for the investigation of real time cellular metabolism. *Magn Reson Med.* 2010;63:322–9.
 156. Chen AP, Albers MJ, Cunningham CH, Kohler SJ, Yen YF, Hurd RE, Tropp J, Bok R, Pauly JM, Nelson SJ, Kurhanewicz J, Vigneron DB. Hyperpolarized C- 13 spectroscopic imaging of the TRAMP mouse at 3 T-initial experience. *Magn Reson Med.* 2007;58(6):1099–106.
 157. Frydman L, Blazina D. Ultrafast two-dimensional nuclear magnetic resonance spectroscopy of hyperpolarized solutions. *Nat Phys.* 2007;3:415–9.
 158. Merritt ME, Harrison C, Mander W, Malloy CR, Sherry AD. Dipolar cross-relaxation modulates signal amplitudes in the (^1H) NMR spectrum of hyperpolarized [^{13}C]formate. *J Magn Reson.* 2007;189(2):280–5.
 159. Reeder SB, Brittain JH, Grist TM, Yen YF. Least-squares chemical shift separation for (^{13}C) metabolic imaging. *J Magn Reson Imaging.* 2007;26(4):1145–52.
 160. Levin YS, Mayer D, Yen YF, Hurd RE, Spielman DM. Optimization of fast spiral chemical shift imaging using least squares reconstruction: application for hyperpolarized (^{13}C) metabolic imaging. *Magn Reson Med.* 2007;58(2):245–52.

161. Macdonald J, Kurhanewicz J, Dahiya R, Espanol MT, Chang LH, Goldberg B, James TL, Narayan P. Effect of glucose and confluency on phosphorus metabolites of perfused human prostatic adenocarcinoma cells as determined by ^{31}P MRS. *Magn Reson Med*. 1993;29(2):244–8.
162. Zierhut ML, Yen YF, Chen AP, Bok R, Albers MJ, Zhang V, et al. Kinetic modeling of hyperpolarized (^{13}C)-pyruvate metabolism in normal rats and TRAMP mice. *J Magn Reson*. 2010;202:85–92.
163. Lapidot A, Gopher A. Cerebral metabolic compartmentation. Estimation of glucose flux via pyruvate carboxylase/pyruvate dehydrogenase by ^{13}C nmr isotopomer analysis of D-[U- ^{13}C] glucose metabolites. *J Biol Chem*. 1994;269:27198–208.
164. Lown KS, Thummel KE, Benedict PE, Shen DD, Turgeon DK, Berent S, Watkins PB. The erythromycin breath test predicts clearance of midazolam. *Clin Pharmacol Ther*. 1995;57:16–24.
165. Kronbach T, Mathys D, Umeno M, Gonzalez FJ, Meyer UA. Oxidation of midazolam and triazolam by human liver cytochrome P450III A4. *Mol Pharmacol*. 1989;36:89–96.
166. Bork RW, Muto T, Beaune PH, Srivastava PK, Lloyd RS, Guengerich FP. Characterization of mRNA species related to human liver cytochrome P-450 nifedipine oxidase and the regulation of catalytic activity. *J Biol Chem*. 1989;264:910–9.
167. Watkins PB, Murray SA, Winkelman LG, Heuman DM, Wrighton SA, Guzelian PS. Erythromycin breath test as an assay of glucocorticoid-inducible liver cytochrome P-450. *J Clin Invest*. 1989;83:688–97.
168. Baker AL, Kotake AN, Schoeller DS. Clinical utility of breath tests for the assessment of hepatic function. *Semin Liver Dis*. 1983;3:318–29.
169. Keshari KR, Kurhanewicz J, Wilson DM, Jeffries RE, Dewar BJ, Van Criekinge M, Vigneron DB, Macdonald JM. Hyperpolarized ^{13}C spectroscopy and a novel NMR-compatible bioreactor system for the investigation of real time cellular metabolism. *Magn Reson Med*. 2010;63:322–9.
170. Kuramitsu S, Inoue K, Kondo K, Aki K, Kagamiyama H. Aspartate aminotransferase isozymes from rabbit liver. Purification and properties. *J Biochem*. 1985;97(5):1337–45.
171. Cunningham CH, Chen AP, Lustig M, Hargreaves BA, Lupo J, Xu D, et al. Pulse sequence for dynamic volumetric imaging of hyperpolarized metabolic products. *J Magn Reson*. 2008;193(1):139–46.
172. Jin ES, Jones JG, Merritt M, Burgess SC, Malloy CR, Sherry AD. Glucose production, gluconeogenesis, and hepatic tricarboxylic acid cycle fluxes measured by nuclear magnetic resonance analysis of a single glucose derivative. *Anal Biochem*. 2004;327(2):149–55.
173. Jue T, Rothman DL, Tavittian BA, Shulman RG. Natural-abundance ^{13}C NMR study of glycogen repletion in human liver and muscle. *Proc Natl Acad Sci U S A*. 1989;86(5):1439–42.
174. Knüttel A, Kimmich R, Spohn KH. Motion-insensitive volume-selective pulse sequences for direct and proton-detected ^{13}C spectroscopy: detection of glycogen in the human liver in vivo. *Magn Reson Med*. 1991;17(2):470–82.
175. Magnusson I, Rothman DL, Jucker B, Cline GW, Shulman RG, Shulman GI. Liver-glycogen turnover in fed and fasted humans. *Am J Physiol*. 1994;266:E796–803.
176. Jehenson P, Canioni P, Hantraye P, Syrota A. Carbon ^{13}C NMR study of glycogen metabolism in the baboon liver in vivo. *Biochem Biophys Res Commun*. 1992;182(2):900–5.
177. Alger JR, Shulman RG. Metabolic applications of high-resolution ^{13}C nuclear magnetic resonance spectroscopy. *Br Med Bull*. 1984;40(2):160–4.
178. Vogt JA, Yarmush DM, Yu YM, Zupke C, Fischman AJ, Tompkins RG, et al. TCA cycle flux estimates from NMR- and GC-MS-determined [^{13}C]glutamate isotopomers in liver. *Am J Physiol*. 1997;272(6 Pt 1):C2049–62.
179. Canioni P, Alger JR, Shulman RG. Natural abundance Carbon- ^{13}C nuclear magnetic resonance spectroscopy of liver and adipose tissue of the living rat. *Biochemistry*. 1983;22(21):4974–80.
180. Cross TA, Pahl C, Oberhänsli R, Aue WP, Keller U, Seelig J. Ketogenesis in the living rat followed by ^{13}C NMR spectroscopy. *Biochemistry*. 1984;23(26):6398–402.
181. Desmoulin F, Canioni P, Cozzzone PJ. Glutamate-glutamine metabolism in the perfused rat liver ^{13}C -NMR study using (2- ^{13}C)-enriched acetate. *FEBS Lett*. 1985;185(1):29–32.
182. Stromski ME, Arias-Mendoza F, Alger JR, Shulman RG. Hepatic gluconeogenesis from alanine: ^{13}C nuclear magnetic resonance methodology for in vivo studies. *Magn Reson Med*. 1986;3(1):24–32.
183. Kalderon B, Gopher A, Lapidot A. Metabolic pathways leading to liver glycogen repletion

- in vivo, studied by GC-MS and NMR. *FEBS Lett.* 1986;204(1):29–32.
184. Shulman GI, Rossetti L, Rothman DL, Blair JB, Smith D. Quantitative analysis of glycogen repletion by nuclear magnetic resonance spectroscopy in the conscious rat. *J Clin Invest.* 1987;80(2):387–93.
 185. Kalderon B, Gopher A, Lapidot A. A quantitative analysis of the metabolic pathways of hepatic glucose synthesis in vivo with ^{13}C -labeled substrates. *FEBS Lett.* 1987;213(1):209–14.
 186. Künnecke B, Cerdan S. Multilabeled ^{13}C substrates as probes in in vivo ^{13}C and ^1H NMR spectroscopy. *NMR Biomed.* 1989;2(5–6):274–7.
 187. Shalwitz RA, Reo NV, Becker NN, Hill AC, Ewy CS, Ackerman JJ. Hepatic glycogen synthesis from duodenal glucose and alanine. An in situ ^{13}C NMR study. *J Biol Chem.* 1989;264(7):3930–4.
 188. Chen W, Ackerman JJ. Localized ^{13}C - ^1H NMR of rat liver in vivo using surface-spoiling gradients. *NMR Biomed.* 1989;2(5–6):267–73.
 189. Zang LH, Laughlin MR, Rothman DL, Shulman RG. ^{13}C NMR relaxation times of hepatic glycogen in vitro and in vivo. *Biochemistry.* 1990;29(29):6815–20.
 190. Cunnane SC. Carbon-by-carbon discrimination of ^{13}C incorporation into liver fatty acids. *FEBS Lett.* 1992;306(2–3):273–5.
 191. Van Cauteren M, Miot F, Segebarth CM, Eisendrath H, Osteaux M, Willem R. Excitation characteristics of adiabatic half-passage RF pulses used in surface coil MR spectroscopy. Application to ^{13}C detection of glycogen in the rat liver. *Phys Med Biol.* 1992;37(5):1055–64.
 192. Wehmeyer N, Gunderson H, Nauman J, Savage S, Hartzell C. Determination of the glycogen synthesis pathway by ^{13}C nuclear magnetic resonance analysis. *Metabolism.* 1994;43(1):38–43.
 193. Jones JG, Cottam GL, Miller BC, Sherry AD, Malloy CR. A method for obtaining ^{13}C isotopomer populations in ^{13}C -enriched glucose. *Anal Biochem.* 1994;217(1):148–52.
 194. Jucker BM, Lee JY, Shulman RG. In vivo ^{13}C NMR measurements of hepatocellular tricarboxylic acid cycle flux. *J Biol Chem.* 1998;273(20):12187–94.
 195. Küstermann E, Seelig J, Künnecke B. Ascorbic acid, a vitamin, is observed by in vivo ^{13}C nuclear magnetic resonance spectroscopy of rat liver. *Am J Physiol.* 1998;274(1 Pt 1):E65–71.
 196. Likhodii SS, Cunnane SC. Uptake of ^{13}C -tracer arachidonate and gamma-linolenate by the brain and liver of the suckling rat observed using ^{13}C -NMR. *J Neurochem.* 1998;72(6):2548–55.
 197. Beckmann N, Seelig J, Wick H. Analysis of glycogen storage disease by in vivo ^{13}C NMR: comparison of normal volunteers with a patient. *Magn Reson Med.* 1990;16(1):150–60.
 198. Petersen KF, West AB, Reuben A, Rothman DL, Shulman GI. Noninvasive assessment of hepatic triglyceride content in humans with ^{13}C nuclear magnetic resonance spectroscopy. *Hepatology.* 1996;24(1):114–7.
 199. Roden M, Perseghin G, Petersen KF, Hwang JH, Cline GW, Gerow K, et al. The roles of insulin and glucagon in the regulation of hepatic glycogen synthesis and turnover in humans. *J Clin Invest.* 1996;97:642–8.
 200. Stevens AN, Iles RA, Morris PG, Griffiths JR. Detection of glycogen in a glycogen storage disease by ^{13}C nuclear magnetic resonance. *FEBS Lett.* 1982;150(2):489–93.
 201. Sillerud LO, Shulman RG. Structure and metabolism of mammalian liver glycogen monitored by carbon-13 nuclear magnetic resonance. *Biochemistry.* 1983;22(5):1087–94.
 202. Reo NV, Siegfried BA, Ackerman JJ. Direct observation of glycogenesis and glucagon-stimulated glycogenolysis in the rat liver in vivo by high-field carbon-13 surface coil NMR. *J Biol Chem.* 1984;259(22):13664–7.
 203. Siegfried BA, Reo NV, Ewy CS, Shalwitz RA, Ackerman JJ, McDonald JM. Effects of hormone and glucose administration on hepatic glucose and glycogen metabolism in vivo. A ^{13}C NMR study. *J Biol Chem.* 1985;260(30):16137–42.
 204. Pahl-Wostl C, Seelig J. Metabolic pathways for ketone body production. ^{13}C NMR spectroscopy of rat liver in vivo using ^{13}C -multilabeled fatty acids. *Biochemistry.* 1986;25(22):6799–807.
 205. Pahl-Wostl C, Seelig J. Ketogenesis in the living rat followed by ^{13}C -NMR spectroscopy. Infusion of [1,3- ^{13}C]octanoate. *Biol Chem Hoppe Seyler.* 1987;368(3):205–14.
 206. Cohen SM. Effects of insulin on perfused liver from streptozotocin-diabetic and untreated rats: ^{13}C NMR assay of pyruvate kinase flux. *Biochemistry.* 1987a;26(2):573–80.
 207. Cohen SM. ^{13}C NMR study of effects of fasting and diabetes on the metabolism of pyruvate in the tricarboxylic acid cycle and the utilization of pyruvate and ethanol in

- lipogenesis in perfused rat liver. *Biochemistry*. 1987b;26(2):581–9.
208. Shulman GI, Rothman DL, Chung Y, Rossetti L, Petit Jr WA, Barrett EJ, et al. ^{13}C NMR studies of glycogen turnover in the perfused rat liver. *J Biol Chem*. 1988;263(11):5027–9.
 209. Cerdan S, Künnecke B, Dölle A, Seelig J. In situ metabolism of 1, omega medium chain dicarboxylic acids in the liver of intact rats as detected by ^{13}C and ^1H NMR. *J Biol Chem*. 1988;263(24):11664–74.
 210. Liu KJ, Henderson TO, Kleps RA, Reyes MC, Nyhus LM. Gluconeogenesis in the liver of tumor rats. *J Surg Res*. 1990;49(2):179–85.
 211. David M, Petit WA, Laughlin MR, Shulman RG, King JE, Barrett EJ. Simultaneous synthesis and degradation of rat liver glycogen. An in vivo nuclear magnetic resonance spectroscopic study. *J Clin Invest*. 1991;86(2):612–7.
 212. Künnecke B, Seelig J. Glycogen metabolism as detected by in vivo and in vitro ^{13}C -NMR spectroscopy using $[1,2-^{13}\text{C}_2]\text{glucose}$ as substrate. *Biochim Biophys Acta*. 1991;1095(2):103–13.
 213. Liu KJ, Kleps R, Henderson T, Nyhus L. ^{13}C NMR study of hepatic pyruvate carboxylase activity in tumor rats. *Biochem Biophys Res Commun*. 1991;179(1):366–71.
 214. Shulman GI, DeFronzo RA, Rossetti L. Differential effect of hyperglycemia and hyperinsulinemia on pathways of hepatic glycogen repletion. *Am J Physiol*. 1991;260(5 Pt 1):E731–5.
 215. Muller HJ, Lanens D, de Cock Buning TJ, van de Vyver FL, Alderweireldt FC, Domisse R, et al. Noninvasive in vivo ^{13}C -NMR spectroscopy in the rat to study the pharmacokinetics of ^{13}C -labeled xenobiotics. *Drug Metab Dispos*. 1992;20(4):507–9.
 216. Lanens D, Muller HJ, Van de Vyver F, de Cock-Bunning T, Spanoghe M, Van der Linden A, et al. Noninvasive in vivo ^{13}C -NMR spectroscopy of a ^{13}C -labeled xenobiotic in the rat. *Magn Reson Imaging*. 1992;10(6):975–81.
 217. Petersen KF, Blair JB, Shulman GI. Triiodothyronine treatment increases substrate cycling between pyruvate carboxylase and malic enzyme in perfused rat liver. *Metabolism*. 1995;44(11):1380–3.
 218. Morikawa S, Inubushi T, Takahashi K, Terada Y, Iwata S, Ozawa K. Glucose and energy metabolism in rat liver after ischemic damage assessed by ^{13}C and ^{31}P NMR spectroscopy. *J Surg Res*. 1996;63(2):393–9.
 219. Morikawa S, Inubushi T, Takahashi K, Ishii H, Ozawa K. Gluconeogenesis and phosphoennergetics in rat liver during endotoxemia. *J Surg Res*. 1998;74(2):179–86.
 220. Changani KK, Bell JD, Iles RA. ^{13}C -Glycogen deposition during pregnancy in the rat following routine meal feeding. *Biochim Biophys Acta*. 1998;1380(2):198–208.
 221. Yarmush DM, MacDonald AD, Foy BD, Berthiaume F, Tompkins RG, Yarmush ML. Cutaneous burn injury alters relative tricarboxylic acid cycle fluxes in rat liver. *J Burn Care Rehabil*. 1999;20(4):292–302.
 222. Zhaofan X, Jianguang T, Guangyi W, Hongtai T, Shengde G, Horton JW. Effect of thermal injury on relative anaplerosis and gluconeogenesis in the rat during infusion of $[\text{U}-^{13}\text{C}]$ propionate. *Burns*. 2002;28(7):625–30.
 223. Baillet-Blanco L, Beauvieux MC, Gin H, Rigalleau V, Gallis JL. Insulin induces a positive relationship between the rates of ATP and glycogen changes in isolated rat liver in presence of glucose; a ^{31}P and ^{13}C NMR study. *Nutr Metab (Lond)*. 2005;2:32.
 224. Geoffrion Y, Butler K, Pass M, Smith IC, Deslauriers R. Plasmodium berghei: gluconeogenesis in the infected mouse liver studied by ^{13}C nuclear magnetic resonance. *Exp Parasitol*. 1988;59(3):364–74.
 225. Hall JE, Mackenzie NE, Mansfield JM, McCloskey DE, Scott AI. ^{13}C -NMR analysis of alanine metabolism by isolated perfused livers from $\text{C}3\text{H}6\text{B}/\text{FeJ}$ mice infected with African trypanosomes. *Comp Biochem Physiol B*. 1988;89(4):679–85.
 226. Nedelec JF, Mégnin F, Patry J, Jullien P, Lhoste JM, Domicoli JL. Modification of the gluconeogenic/glycolytic balance in isolated perfused liver of myeloproliferative leukemia infected mice: a ^{13}C NMR study. *Comp Biochem Physiol B*. 1990;95(3):505–14.
 227. Cohen SM, Werrmann JG, Tota MR. ^{13}C NMR study of the effects of leptin treatment on kinetics of hepatic intermediary metabolism. *Proc Natl Acad Sci U S A*. 1998;95(13):7385–90.
 228. Choi IY, Wu C, Okar DA, Lange AJ, Gruetter R. Elucidation of the role of fructose 2,6-bisphosphate in the regulation of glucose fluxes in mice using in vivo (^{13}C) NMR measurements of hepatic carbohydrate metabolism. *Eur J Biochem*. 2002;269(18):4418–26.
 229. Cohen SM, Duffy JL, Miller C, Kirk BA, Candelore MR, Ding VD, et al. Direct observation (NMR) of the efficacy of glucagon receptor antagonists in murine liver expressing the human glucagon receptor. *Bioorg Med Chem*. 2006;14(5):1506–17.